High-performance numerical modeling of sprite streamers : Development of optical and electromagnetic diagnostics to characterize transient luminous events for the TARANIS mission

Matthieu Garnung

▶ **To cite this version:**

Matthieu Garnung. High-performance numerical modeling of sprite streamers : Development of optical and electromagnetic diagnostics to characterize transient luminous events for the TARANIS mission. Plasma Physics [physics.plasm-ph]. Université d'Orléans, 2021. English. NNT : 2021ORLE3161 . tel-03771856

HAL Id: tel-03771856
https://theses.hal.science/tel-03771856

Submitted on 7 Sep 2022

HAL is a multi-disciplinary open access archive for the deposit and dissemination of scientific research documents, whether they are published or not. The documents may come from teaching and research institutions in France or abroad, or from public or private research centers.

L'archive ouverte pluridisciplinaire **HAL**, est destinée au dépôt et à la diffusion de documents scientifiques de niveau recherche, publiés ou non, émanant des établissements d'enseignement et de recherche français ou étrangers, des laboratoires publics ou privés.

UNIVERSITÉ D'ORLÉANS

ÉCOLE DOCTORALE Energie, Matériaux, Sciences de la Terre et de l'Univers

Laboratoire de physique et chimie de l'environnement et de l'espace (LPC2E)

THÈSE présentée par :

Matthieu GARNUNG

soutenue le : **16 mars 2021**

pour obtenir le grade de : **Docteur de l'Université d'Orléans**

Discipline/ Spécialité : Sciences de l'Univers / Électricité atmosphérique

High-performance numerical modeling of sprite streamers: Development of optical and electromagnetic diagnostics to characterize transient luminous events for the TARANIS mission.

THÈSE dirigée par :

[M. Celestin Sebastien]	Maître de conférence, Université d'Orléans, France
[M. Farges Thomas]	Chercheur, CEA, DAM, DIF, Arpajon, France

RAPPORTEURS :

[M. Hobara Yasuhide]	Professeur, The University of Electro-Communications, Japan
[M. Soula Serge]	Professeur, Université Paul Sabatier - Toulouse III, France

---

JURY :

[Mme. Huret Nathalie]	Professeur, Université Clermont-Auvergne, France, Présidente de jury
[M. Fullekrug Martin]	Professeur, University of BATH, UK
[M. Bonaventura Zdeněk]	Maître de conférence, Masaryk University, Czech Republic
[M. Pinçon Jean-Louis]	Chercheur, LPC2E, France

Acknowledgment

Une thèse, c'est véritablement une aventure scientifique & humaine. Dans celle-ci, il y a deux protagonistes que je voudrais commencer par remercier. Il s'agit de Sébastien Célestin et Thomas Farges qui furent, respectivement directeur de thèse et co-directeur de thèse. Ce fut un immense honneur et un immense plaisir de travailler avec eux, d'apprendre, de voyager et de découvrir ces petits filaments de plasma. Cette thèse ne serait pas ce qu'elle est sans leurs écoutes, conseils, remarques et encouragements. Un grand merci à eux deux !

Je tiens également à remercier les membres du jury qui ont participé à l'évaluation de ces travaux, Nathalie Huret, Serge Soula, Yasuhide Hobara, Martin Fullekrug, Zdeněk Bonaventura et Jean-Louis Pinçon.

Dans ce formidable labo qu'est le LPC2E, je tiens à remercier ceux avec qui nous avons partager beaucoup de choses, de nos peines de doctorants, de nos résultats, nos stress, nos joies. Ainsi, je remercie (sans ordre quelconque), Romaric, Anna, Mélody, Nini, Andrea, Nicolas, Vamsee, Minna, Vanessa, Chen, Ségolène, Louis, Mélina (et si je t'ai oublié, n'hésite à pas te rajouter en lisant à nouveau la phrase). Ajoutons également Pietro, Gaëtane, Jérémie, Shogo, Shu, Luca, Emmanuel, Federico et Alexandra.

Une petite pensée également pour les étudiants avec qui j'ai apprécié travailler, Paul, Antoine, Eddy, Benjamin et Vika.

Néanmoins, il me semble aussi bien de mentionner les différents membres du labo avec qui nous avons parfois échangé autour d'un café, au croisement du couloir ou lors d'un repas. Ainsi, je voudrais chaleureusement remercier Thierry, Pierre, Orélien, Jean-Louis, Matthieu, Clara, Claire, Nathalie, Franck, Xavier, Ted, Michel, Dominique L., Dominique D., Vincent, Benoît... (encore une fois, si toi lecteur tu te sens lésé, tu peux te rajouter à la liste). Un grand merci également à l'équipe méca, Gilles, Stéphane et Thierry pour leur aide lors des manips FRIPON. Pareillement pour Isabelle, Catherine

et Tiphaine pour tous les aspects administratifs (déplacements, achats, paperasses...).

Merci également à l'équipe FRIPON pour nous avoir laissé essayer la détection des TLEs avec leur formidable réseau !

Un grand merci aux membres du Stick Fight Club pour les parties endiablées grâce à la maîtrise du kung-fu (coucou Anna) et du Full Counter (n'est-ce pas Mélody ?) ainsi que le talent, jusqu'à présent inégalé, du duo Andrea-Vamsee.

Enfin sur un plan plus personnel, je remercie mes parents, ma petite soeur et mes grand-parents (avec une pensée supplémentaire pour mon grand-père).

Contents

List of Figures

List of Tables

Acronyms

GPU Graphic Processor Unit

SOR Successive Over Relaxation

SMT Simultaneous MultiThreading

CPU Central Processor Unit

MPI Message Passing Interface

SIMD Single Instruction Multiple Data

GPGPU General Purpose Graphic Processor Unit

TLE Transient Luminous Event

TGF Terrestrial Gamma ray Flash

TARANIS Tool for the Analysis of Radiation from lightning and Sprites

LEP Lighting-induced Electron Precipitation

FCT Flux Correct Transport

PIC Particle-In-Cell

CNES Centre National d'Études Spatiales

AMR Adaptive Mesh Refinement

ISUAL Imager for Sprites and Upper Atmospheric Lightning

LSO Lightning and Sprite Observations

GLIMS Global Lightning and Sprite Measurements

ASIM Atmosphere-Space Interaction Monitor

Notations

ϕ Electric potential

E Electric field

q Electric charge

ρ Charge density

n_e Electron density

n_p Positive ion density

n_n Negative ion density

D_k Diffusion for the species k

ϵ_0 Vacuum permittivity

ν_i Ionization frequency

ν_{a2} Two-body attachment frequency

ν_{a3} Three-body attachment frequency

β_{ep} Electron-positive ion recombination coefficient

β_{np} Negative-positive ion recombination coefficient

S_{ph} Photoionization source term

A_j Fitting coefficient associated with the three-group SP_3model

p_{O_2} Partial pressure of oxygen

$\lambda_j p_{O_2}$ Absorption term used in the three-group SP_3model

τ_u Lifetime of the excited state u

n_u Density of the radiative excited species u

R Source-observer distance

ξ Photoionization efficiency

$\Psi_{SP_3,0,j}$ Three-group SP_3approximation j-term of the isotropic part of the photon distribution function

S_{ph} Photoelectron production rate

p_q Quenching pressure

p Local air pressure

$\mathrm{d}t_{\text{ioni}}$ Time scale associated with the Ionization frequency

$\mathrm{d}t_{\text{atta}}$ Time scale associated with electron attachment process

$\mathrm{d}t_{\text{spectro}}$ Time scale associated with lifetime of excited species

$\mathrm{d}t_{\text{CFL}}$ Time scale associated with the Courant–Friedrichs–Lewy (CFL)

$\mathrm{d}t_{\text{M}}$ Time scale associated with the dielectric relaxation (Maxwell time)

μ_e Electron mobility

k_B Boltzmann constant

c Speed of light in vacuum

$F_{i+\frac{1}{2},j}$ Flux at the interface $i+\frac{1}{2},j$

$S_{i+\frac{1}{2},j}$ Surface of the interface $i+\frac{1}{2},j$

$V_{i,j}$ Volume of the cell (i,j)

T Thermodynamic temperature of the local medium

A_k Einstein coefficient of the excited state k

θ Polar angle between the streamer axis and the receiver

$i(z, t - \frac{R}{c})$ Current along the z-axis at the retarded time $t - \frac{R}{c}$

Resumé en français

Les Evenements Lumineux Transitoires (ELT) sont des manifestations lumineuses et soudaines se produisant au-dessus des nuages d'orages pendant quelques millisecondes jusqu'à la seconde, et pouvant s'étendre entre 20 km et 90 km d'altitude. L'acronyme ELT regroupe en son sein, une variété de manifestations lumineuses pouvant revêtir différentes formes. Celles-ci se produisent à des gammes d'altitudes et d'intensités lumineuses dinstinctes, et ont souvent des mécanismes d'origines physiques différentes. Dans le cadre de cette thèse, nous nous interessons tout particulièrement aux sprites. Il s'agit d'émissions lumineuses résultant de la création de filaments de plasma, nommés streamers, durant quelques millisecondes et s'étendant entre 40 km et 90 km d'altitude. Ces derniers peuvent se propager vers le bas ou vers le haut. L'origine des sprites provient d'une brutale rupture d'équilibre au sein du nuage d'orage. En effet, durant son existence, une production de charges électriques va naître par des effets thermoélectriques. Ces charges vont se séparer au sein du nuage d'orage. Dans une vision simplifiée, le nuage d'orage est assimilable à un dipôle, dont les charges négatives se trouvent au centre tandis que les charges positives vont se trouver à son sommet. Comme ce processus est plus lent que le temps de Maxwell local (c.-à-d. le temps de relaxation du milieu), l'ionosphère (région conductrice de l'atmosphère à partir de 80 km d'altitude) s'y adapte en les écrantant électrostatiquement. Il en vient une situation d'équilibre entre la distribution de charges au sein du nuage d'orage et l'ionosphère. Au cours d'un processus de décharges du nuage d'orage via la formation d'une connection électrique entre le nuage et le sol engrendant la formation d'un éclair nuage-sol, les charges électriques positives se trouvant au sommet du nuage d'orage vont se déplacer très rapidement vers le sol. La durée des processus de décharges étant très inférieure au temps de relaxation de Maxwell, il en résulte un important déséquilibre de charges entre le nuage d'orage et l'ionosphère. Un champ quasi-électrostatique apparaît alors capable de pénétrer jusque

dans les hautes couches de l'atmosphère terrestre. Ce champ électrique va thermaliser les électrons des couches supérieures de l'atmosphère qui vont amener à la création de filaments de plasmas résultant de l'ionisation du milieu local. Dans le même temps, des phénomènes d'excitations et dés-excitations produits par les collisions des électrons avec les molécules neutres de l'atmosphère vont résulter en l'émission de photons dont la longueur d'onde tend vers le rouge, à l'origine des couleurs rougeâtres caractéristiques des sprites.

L'étude des sprites peut se faire avec des mesures des champs électrique et magnétique dans la gamme radio ou des observations optiques depuis l'espace ou le sol. En novembre sera lancée la mission Tool for the Analysis of RAdiation from lightning and Sprites (TARANIS), mission spatiale de l'agence spatiale française (CNES) dediée à l'étude des ELT mais également aux émissions de flashes de rayons gammas TGF. TARANIS embarquera des caméras, des photomètres, des capteurs de particules et de rayonnement X et gamma ainsi que des antennes électriques et magnétiques. Les mesures d'observations se faisant depuis l'espace, il est nécessaire de développer un moyen d'analyser les résultats afin de pouvoir comprendre la physique des TLEs.

Le but de cette thèse est de développer une méthode de diagnostic optique pour déduire l'altitude et le champ électrique des filaments de plasma de sprites. En complément de ces travaux, cette thèse mentionne la prédiction de signature radio dans la gamme HF-VHF résultant de la collision frontale entre deux streamers à polarités opposées. De plus, elle comporte un aspect exploratoire concerant la physique des longs streamers ($>5\,\mathrm{km}$) obtenu graĉe au code haute-performance développé au cours de cette thèse.

Cette thèse est découpée en quatre parties. Nous commençons par décrire le modèle de streamer haute performance que nous avons développé afin de reproduire, via des simulations numériques, le caractère électrodynamique des streamers de sprites associés à leur propagation. Puis, nous expliquerons comment nous avons utilisé ce modèle pour prédire des signatures radios associées lors de collisions de streamers de polarité

opposées en vue de leur détection par le satellite TARANIS, mais également par des radiotélescopes tel que NenuFAR (situé à Nançay). Nous continuons en expliquant comment déduire l'altitude et le champ électrique des sprites à partir des observations optiques qu'effectuera TARANIS. Nous testerons notre approche sur un cas réel, publiée et discuter dans la littérature. Enfin, nous utilisons les possibilités offertes par notre code haute-performance pour étudier les caractéristiques de streamers pouvant atteindre 15 km de long en atmosphère réaliste, c'est à dire à densité d'air variable avec l'altitude. Nous concluons ce manuscrit en proposant de possibles pistes pour des études futures.

Chapitre 2 : Notre modèle de streamer repose sur la modélisation de quatre comportements fondamentaux. Premièrement, l'aspect electrostatique du streamer lié à la présence de charge est pris en compte en résolvant l'équation de Poisson discrétisée suivant un schéma à cinq points. Leur déplacement sous l'action de champs électriques est décrit par une approche fluide via l'équation dite de dérive-diffusion discrétisée par un schéma faible-ordre et un schéma haut-ordre combiné à un limitateur de flux dénommé Flux Corrected Transport (FCT), afin de réduire la présence d'oscillations numériques produites par l'existence de forts gradients de densité. La présence de forts champs électriques, en particulier dans la tête du streamer, entraine l'apparition de phénomène de photo-ionisation induite par la dés-excitation du diazote en émettant des photons UV. Ces photons sont émis dans l'environnement proche du streamer créant une région ionisée en amont de la tête via l'ionisation du O_2. Afin de prendre en considération ce phénomène, nous utilisons le modèle trois groupes SP3. Ce modèle consiste à résoudre la partie isotropique de la fonction de distribution des photons obtenue par l'équation du transfert radiatif. Enfin le streamer se propagant dans l'atmosphère terrestre, il est nécessaire de prendre en considération les réactions chimiques entre le streamer et son milieu. Dans notre modèle, nous considérons l'ionisation du dioxygène produit par impact électronique ainsi que celui du N_2, ces deux réactions chimiques étant des termes sources d'électrons. Nous prenons également, en tant que terme puits, les réactions

d'attachements à deux et trois corps pour le dioxygène. L'aspect haute-performance du modèle est atteint en exploitant les capacités modernes des processeurs à travers l'utilisation du paragdime Single Instruction Multiple Data (SIMD) pour vectoriser notamment les boucles, offrant la possibilité d'effectuer une même opération sur plusieurs données pour un coût en nombre de cycles d'horloges inférieur à celui de la même opération sur chaque donnée individuellement. En outre, nous exploitons massivement le calcul parallèle à travers une approche à mémoire partagée grâce à l'API OpenMP. Enfin, le solveur de Poisson et du modèle trois groupes SP3 étant les plus consommateurs en temps de calcul, une version pouvant tourner sur des architectures hétérogènes a également été developpée, et testée avec succès sur des cartes graphiques. Une série d'optimisations a été également appliquée en couplant les capacités offertes par les compilateurs modernes et le respect de la norme du langage Fortran.

Chapitre 3 : Ce modèle a été par la suite utilisé afin de prédire la signature radio associée lors d'une collision frontale entre deux streamers à polarités opposées. Des travaux antécedents ont montré que de telles collisions sont possibles au sein des sprites en raison de la propagation extrêmement complexe des streamers les constituant. A travers les simulations numériques effectuées, il a été observé une augmentation du champ électrique lorsque les deux têtes de streamers (de polarités opposées) se rencontrent. Cette augmentation très rapide du champ électrique (quelques picosecondes pour une collision se produisant au niveau du sol, c'est-à-dire à pression atmosphérique standard, s'explique par une augmentation de la densité électrique lors de la collision liée à l'addition des champs électriques provenant des deux têtes de streamers. Cette augmentation du champ électrique entraine une plus forte ionisation électronique dans la zone d'interaction (correspondante à l'interprénétration des deux têtes) qui en retour augmente la conductivité du milieu, laquelle entraine très rapidement un collapse du champ électrique. Cette importante variation du champ électrique sur une très petite échelle de temps trahit la possibilité d'avoir une émission électromagnétique associée

à celle-ci. Un rapide calcul d'ordre de grandeur montre que les émissions électromagnétiques attendues sont dans la gamme HF pour une collision se produisant à 60 km d'altitude ce qui est potentiellement mesurable par les instruments radio à bord du satellite TARANIS. Afin d'élucider la question, nous avons simulé la collision frontale entre deux streamers de polarités opposées initiés à 70 km d'altitude. En utilisant le modèle d'antenne d'Uman assimilant le streamer à une antenne rectiligne, nous avons estimé le champ magnétique produit par la collision avant, pendant et après la collision. De celui-ci, nous avons calculé la densité spectrale du signal afin de la comparer avec la sensibilité de l'instrument de mesure de champs magnétiques (IMM) et l'instrument de mesure de champs électriques (IME-HF) à bord du satellite TARANIS. L'obtention du champ électrique à partir du champ magnétique s'effectue sous l'hypothèse que pour de grandes distances, le vecteur d'onde est plan.

A la différence des mesures faites dans l'espace, les mesures radios au sol telles que celles réalisées par le radiotélescope NenuFAR ne sont pas affectées par le filtrage ionosphérique. Nos résultats démontrent que la sensibilité de NenuFAR est d'un million de fois supérieure à l'intensité du signal qui doit être mesuré ouvrant ainsi la possibilité de sonder la microphysique des streamers via de tels instruments grâce à leur résolution spatio-temporelle. Enfin, de très récents travaux mettent en lumière la possiblité d'utiliser les émissions radios incohérentes pour déterminer le nombre de streamers au sein d'un sprite.

Chapitre 4 : Nous avons également utilisé le modèle de streamers pour développer une méthode de diagnostic optique capable de déterminer l'altitude et le champ électrique dans la tête du streamer en se basant sur les ratios spectroscopiques, c'est-à-dire le rapport entre la quantité de photons produit par unité de temps par un système spectroscopique en fonction d'un autre. Cette méthode de diagnostic s'appuie très fortement sur la méthode des ratios récemment développée. De précédents travaux numériques et des campagnes de mesures ont montré que les quatre systèmes de bandes utiles pour

l'étude des sprites sont le système Lyman-Birge-Hopfield (abrégé LBH), le premier et le second système du N_2 (abrégé $1\,PN_2$ et $2\,PN_2$, respectivement), et le premier système négatif du N_2^+ (abrégé $1\,NN_2^+$). Dans ce chapitre, nous simulons grâce à notre code, un streamer de 5 km de long à 80 km d'altitude et se propageant vers une altitude de 75 km. De ce dernier, nous calculons la brillance (le nombre de photons par unité de temps) pour les quatres systèmes de bandes cités ci-dessus. A partir de ces systèmes, nous utilisons la méthode des ratios afin de calculer celui-ci pour différentes combinaisons de champs électriques et d'altitudes. Pour déterminer l'altitude et le champ électrique, nous reportons la valeur du ratio obtenue soit par simulations numériques (dans le cas de vérification de notre approche) soit obtenue à partir de mesures photométriques (via l'instrument ISUAL du satellite FORMOSAT-2), nous permettant ainsi de produire un ensemble de combinaisons d'altitudes et de champs électriques. En faisant ceci pour deux systèmes de bandes, nous montrons que nous pouvons déduire l'altitude du sprite en calculant l'intersection des deux ensembles. Ensuite, à la manière de la résolution d'un système d'équations linéaires, il suffit de rechercher le champ électrique correspondant. L'application de cette méthode, sur un cas issu de simulations numériques, nous a permis de mettre en évidence que l'utilisation du couple de ratios $\frac{\mathrm{LBH}}{1\mathrm{PN_2}}$ et $\frac{\mathrm{LBH}}{1\mathrm{NN_2^+}}$ est très adaptée pour ce type de méthode. En cas d'absence du système $1\,NN_2^+$, l'utilisation du ratio $\frac{2\mathrm{PN_2}}{1\mathrm{PN_2}}$ est recommandé. Nous appliquons ces méthodes sur deux événements complexes de sprites reportés par la mission ISUAL. Cette analyse a permis de déterminer une altitude et un champ électrique dans la tête du streamer compatible avec ceux déduits par des observations et des simulations numériques. En revanche, les résultats obtenus pour un second événements sont sujet à discussion en raison de la superposition de deux sprites quasi-simultanément. Nous avons également mis en lumière la possibilité d'utiliser le taux d'expansion des streamers obtenu à partir d'une régression linéaire dans un espace logarithmique de leur brillance durant leur phase de propagation afin de remonter au champ électrique ambiant dans lequel les streamers se propagent, et donc

à la variation du moment de charge de l'éclair parent. Au cours du développement de la méthode de diagnostic, nous avons entrevu la possibilité d'utiliser les données issues des photomètres pour estimer la taille de l'inhomogénéité ayant donné naissance aux streamers. Cette méthode requiert néanmoins, d'utiliser une pré-tabulation au travers de simulations.

Chapitre 5 : L'utilisation de notre code haute-performance, nous a permis de simuler des streamers pouvant atteindre une longueur de 15 km en densité d'air variable, soit deux échelles de hauteur atmosphérique. Ces simulations à caractère exploratoire permettent d'observer une augmentation de la densité electronique dans la tête du streamer ainsi que celle du champ électrique au cours de la propagation du streamer. Nous avons également exploré l'impact de la densité d'air variable sur l'évaluation de l'altitude et du champ électrique dans la tête du streamer. Nous avons trouvé que celle-ci change le comportement du ratio $\frac{\mathrm{LBH}}{1\mathrm{PN}_2}$ en fonction du champ électrique réduit ambiant, en particulier avec une plus grande amplitude de variation du ratio spectroscopique lorsque le champ électrique réduit ambiant est grand. Les possibilités de simulations offertes par ce code, nous ont également permis d'étudier l'influence de la taille de l'inhomogénéité donnant naissance aux streamers sur leur taux d'expansion lorsqu'ils sont immergés dans un champ électrique constant. Nous avons pu constater un accroissement du facteur d'expansion à mesure que la taille de l'inhomogénéité utilisée pour déclencher le streamer s'accroît. Ceci est complémentaire à l'impact joué par le champ électrique ambiant sur ce facteur d'expansion. De plus, nous avons observé que le champ électrique dans la tête du streamer n'est pas affecté par la taille de l'inhomogénéité, mais uniquement par le champ électrique ambiant.

A titre d'ouverture pour la poursuite de ces travaux, au cours de cette thèse nous avons noté que la méthode actuelle, pour résoudre l'équation de Poisson ainsi que le système d'équations non-linéaires découlant de la méthode du trois groupes SP_3, semble avoir dépassé son domaine d'efficacité pour des streamers longs impliquant le recours à

de grandes grilles de calculs. L'utilisation de solveurs directs en lieu et place de solveurs itératifs optimisés pour fonctionner sur les cartes graphiques pourrait s'avérer salvateur et offrir ainsi de nouvelles possibilités dans l'étude des streamers longs. Il est également à noter que l'implémentation à mémoire partagée utilisée pour le solveur de Poisson et la méthode du trois groupes SP_3, peut être également étendue à une implémentation à mémoire distribuée offrant ainsi, en complément ou non d'une implémentation sur des architectures hétérogènes ou d'hybridations, la possibilité de simuler également de longs streamers. Néanmoins, des études d'optimisations du code et de topologie réseaux (ethernet comme intership), sont nécessaires afin d'avoir une implémentation efficace.

L'étude conduite sur la partie radio devrait être poursuivie par l'analyse des données de TARANIS et en particulier de son instrument de mesures de champs électriques. Cette observation est également applicable pour le radiotélescope NenuFAR.

La méthode de diagnostic optique pourrait être developpée encore plus loin en étudiant l'influence des facteurs de corrections pour différentes configurations de champs électriques, de rayon du domaine de simulation mais également pour différentes tailles caractéristiques associées à l'inhomogénéité donnant naissance au streamer. Ajoutons également que la prise en compte de la densité d'air variable serait une véritable avancée sur l'utilisation de cette méthode.

Les travaux exploratoires menés sur les streamers longs méritent d'être prolongés au travers des questions concernant la propagation des streamers dits "upward" afin d'étudier l'effet d'une diminutation de la densité d'air avec l'altitude. En outre, les questions concernant le "branching", c'est-à-dire la séparation d'un streamer de plusieurs centaines de mètres de rayon en plusieurs streamers d'un diamètre inférieur, sont étudiées au vu des effets de la densité d'air sur le champ électrique, mais également des longeurs caractéristiques associées à la photoionisation. Une autre étude paramétrique en densité d'air variable du rôle examinant le champ électrique ambiant et la taille de l'inhomogénéité sur l'expansion du streamer pourrait être menée.

I Introduction

Transient Luminous Events (TLEs) are sudden and bright luminous plasma discharges occurring above thunderclouds, spreading over several dozens of kilometers of altitude. TLEs designate a lot of various events having their own characteristic duration and altitude range. The figure 1 gives an overview of various reported TLEs. Sprites, halos,

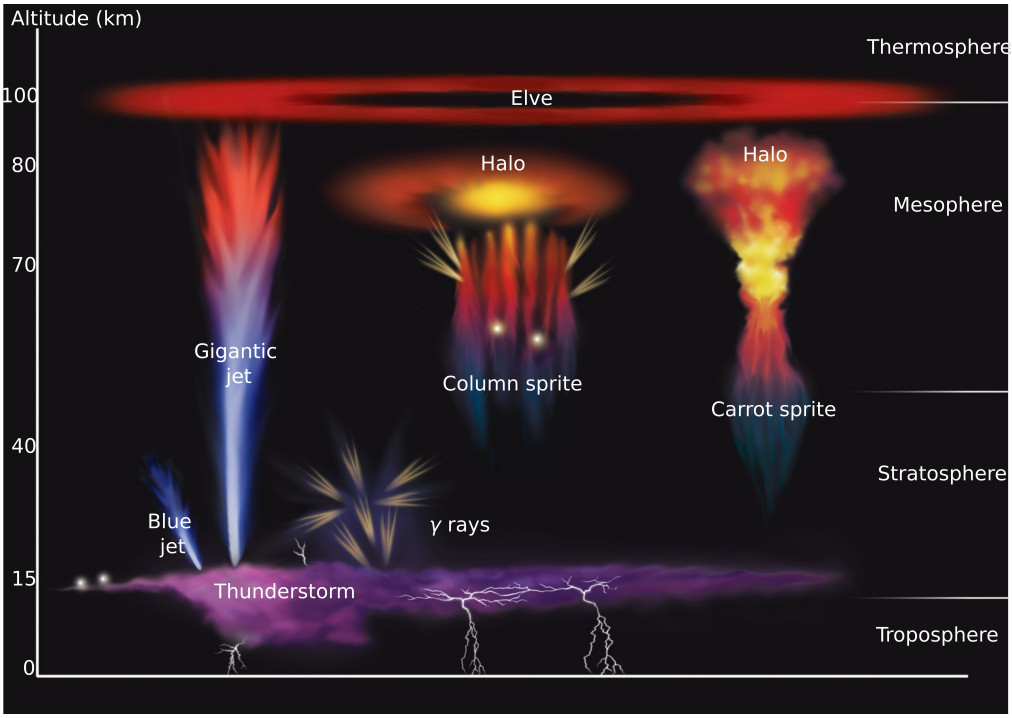

Figure 1: Transient Luminous Events (TLEs) that could appear during a thunderstorm showing the connection between the lowest layer of the Earth's atmosphere (troposphere) and the upper atmosphere and the ionosphere. Adapted from [*Blanc and Farges*, 2012].

elves, jets, and gigantic jets are produced by electrical processes associated with lightning discharges. They are the optical manifestation of electrodynamic coupling between the troposphere and the upper atmosphere up to the ionosphere. Some features such altitude, duration, spatial extent, and origins are summarized in Table 1.

Sprites were first reported by *Franz et al.* [1990] during an experimentation with a

TLE	Altitude	Duration	Spatial extension	Intensity	Origins
Sprite	40 km to 90 km	1 ms to 10 ms	Up to 40 km vertically	∼1.6 M R	Quasi-electrostatic field
Halo	90 km	1 ms to 10 ms	<100 km horizontally	∼100 k R	
ELVES	∼ 90 km	1 ms	Up to 300 km horizontally	∼500 k R	EMP
Blue jets	∼ 20 km	200 ms to 300 ms	2.5 km vertically	∼490 k R	Streamer corona discharge
Gigantic jet	20 km	∼500 ms	60 km vertically	∼1 M R	

Table 1: Summary of the main TLEs characteristics illustrated in Figure 1. EMP stands for ElectroMagnetic Pulse produced by one associated parent lightning. ELVES stands for Emission of Light and very Low Frequency perturbations due to Electromagnetic Pulses Sources. References for sprites and halos [e.g., *Pasko et al.*, 1997, 1998; *Gerken et al.*, 2000; *Pasko*, 2006a; *Kuo et al.*, 2008; *Qin et al.*, 2013a]. References for ELVES [e.g., *Pasko*, 2006a; *Kuo et al.*, 2008]. References for Blue jets [e.g., *Wescott et al.*, 1995; *Xu et al.*, 2020]. References for gigantic jet [e.g., *van der Velde et al.*, 2007; *Kuo et al.*, 2008; *Chern et al.*, 2014].

low light CCTV camera. General physical processes generating sprites are explained in *Pasko et al.* [1997], and illustrated in the figure 2. The first stage is the slow building-up of charges in the thundercloud. Positive charges move to the top of the thundercloud while negative charges migrate to the base. As this accumulation is a slow process, the ionosphere shields the positive charges in accumulating negative charges above the storm. When a lightning discharge occurs, either with a +CG or -CG, it results in a sudden disruption in the charge equilibrium. This difference of charges over a large scale (typically, thunderstorm tops are between 10 and 15 km altitude and the lower layers of the ionosphere (where ELVES and halos occur) is at 90 km altitude) produces an electric field penetrating the troposphere, stratosphere, mesosphere, and ionosphere. This electric field heats up electrons, which interact with the air medium producing a bright plasma discharge. The produced electric field has a lifetime approximately equal to the local relaxation time also referred to as Maxwell time ($\tau_\sigma = \frac{\epsilon_0}{\sigma}$, where ϵ_0 is the permittivity of free space and σ is the local conductivity) at the considered altitude.

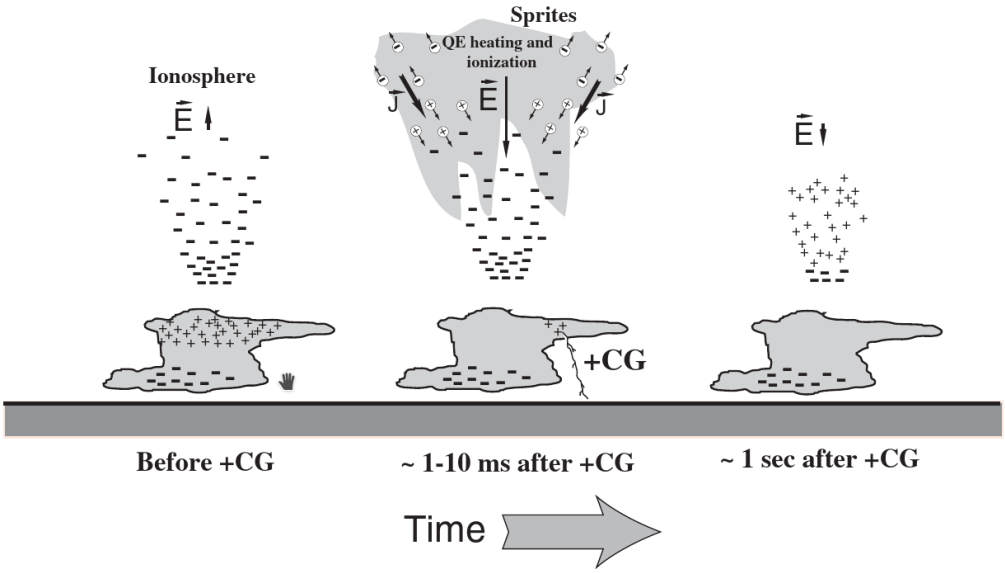

Figure 2: Illustration of the general mechanisms producing sprites. The + and - symbols correspond to signs of electric charges, $\vec{E}$ indicates the electric field, +CG stands for positive (+) cloud-to-ground, which is one of the ways thundercloud discharge, and QE stands for quasi electrostatic. Reproduced from [*Pasko*, 2007].

Sprites are made up of plasma filaments named streamers. They are ionizing waves propagating in a neutral medium, turning it into plasma filaments. Streamers have a high electric field contained in a small region at the tip named the streamer head, as sketched in Figure 3. Due to the high electric field over a small region, the streamer head is the place where most of the ionization and excitation of the local medium through electron impact occur. Photoionization processes are critical to the propagating of streamers. The photoionization processes result from the radiative deexcitation of excited N_2 molecules releasing UV photons capable of ionizing O_2 molecules. This region of the streamer is also the brightest one. The streamer channel is the region left behind the streamer head, which is the place of a weak electric field relatively to the head. This region is dominated by chemical processes like attachment, in which electrons and oxygen molecules form negative oxygen ions. The channel also emits light in a weaker manner than the head, and hence have a lesser contribution to the whole streamer emission [.e.g., *Bonaventura*

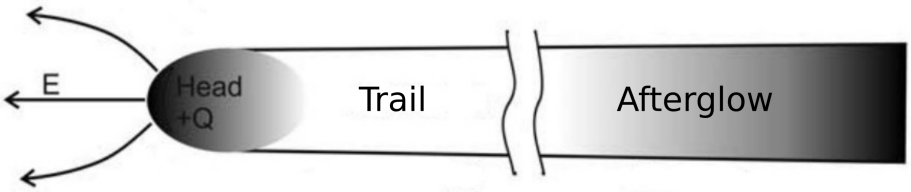

Figure 3: Illustration of the three regions of a streamer composed by the head, the trail, and the afterglow. The head contains an electric field stronger than in the rest of the streamer. The trail is the region after the head and has a weaker electric field than the head. The afterglow is farther away from the head, and corresponds to an increase of the optical emissions. Adapted from [*Sentman et al.*, 2008].

et al., 2011]. The increase of the luminosity of the streamer channel is sometimes referred to as the afterglow (Figure 3). An example of the filamentary nature of sprites is shown in Figure 4. The diameter of a streamer as shown in Figure 4a depends on its altitude. It is between 60 m to 120 m at 60 km altitude and grows up to 196 m at 80 km [*Gerken et al.*, 2000]. As predicted by *Pasko et al.* [1998] , an interesting feature of streamers is the possibility to scale them from one altitude to another using similarity laws, offering the possibility to characterize streamers from the ground to upper part of the Earth's atmosphere in an unified way (e.g., electron density, electric field, time, etc.) as a function of the local air density. A comprehensive review of the use of similarity laws are given by *Pasko et al.* [1998]; *Pasko* [2006a]. Below we report some useful relations, which will be used in this thesis:

- Time: $t_N = t_{N_0} \frac{N_0}{N}$
- Length: $L_N = L_{N_0} \frac{N_0}{N}$
- Electric field: $E_N = E_{N_0} \frac{N}{N_0}$
- Electron density: $n_{e_N} = n_{e_{N_0}} \frac{N^2}{N_0^2}$

where N is the air density at a given altitude and N_0 is the air density at ground level. A more exhaustive list can be found in *Ihaddadene* [2016]. Note that the relation for

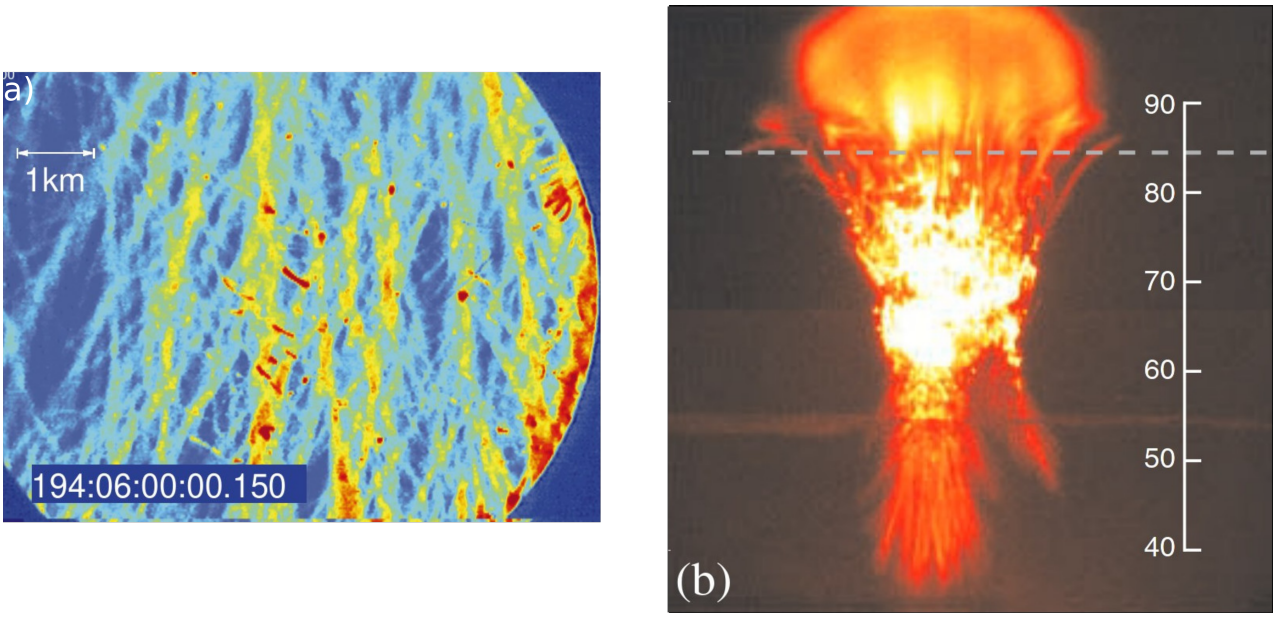

Figure 4: Illustration of streamers within a carrot sprite. a) Telescopic Image of a bright sprite event offering the possibility to measure the streamer's diameter. Reproduced from [*Gerken et al.*, 2000]. b) Photograph of a carrot sprite with the altitude on the right. Adapted from [*Pasko and Stenbaek-Nielsen*, 2002].

electron density can also be used for positive and negative ion densities. However, it must be mentioned that *Liu and Pasko* [2004] have shown that although similarity laws are perfectly valid above 25 km, below this altitude, they would break because of the collisional quenching excited states responsible for the photoionization.

There are various research questions about the physical mechanisms leading to the perturbations, production of sprites and their effects. Specifically, the initiation mechanisms, the role played by ionospheric irregularities (e.g., plasma tail produced by a meteor), the filamentation processes, the interaction and branching of plasma filaments, their propagation dynamics, the observed various morphologies, and their global effects such as their impact on the atmospheric chemistry, their role in the Global Electric Circuit (GEC), the induced ionospheric perturbations, and their impact on radio propagation [e.g., *Pasko et al.*, 2013].

Observations of sprites have been performed based on various techniques including radio observations [e.g., *Cummer et al.*, 1998; *Füllekrug et al.*, 2001; *Cummer et al.*, 2006b; *Füllekrug et al.*, 2010; *Farges and Blanc*, 2011], optical observations from ground-based observations [e.g., *Gerken et al.*, 2000; *Cummer et al.*, 2006a; *Kanmae et al.*, 2010] optical observation using space instruments [e.g., *Chern et al.*, 2003; *Blanc et al.*, 2004; *Sato et al.*, 2015; *Neubert et al.*, 2019], and observation of infrasounds [e.g., *Farges and Blanc*, 2010].

They are usually modeled with numerical codes that split into two categories depending on the manner to describe the motion of electrons and ions:

Fluid approach consists in describing the motion of species through solving coupled drift-diffusion equations. This group can be subdivided into two sub-categories based on the numerical grid used:

Regular mesh where the mesh size does not change throughout the simulation [e.g., *Pasko et al.*, 1997; *Liu and Pasko*, 2004; *Bourdon et al.*, 2007; *Qin et al.*, 2013b; *Ihaddadene and Celestin*, 2015; *Shi et al.*, 2017; *Janalizadeh and Pasko*, 2019].

Adaptive Mesh Refinement (AMR) where the mesh size is dynamically updated throughout the simulation to concentrate the computation resources to relevant regions [e.g., *Montijn et al.*, 2006; *Ebert et al.*, 2006; *Luque*, 2017]. An illustration of the use of AMR for streamer simulations is shown in Figure 5.

Particle-In-Cell (PIC) uses a particle description for each species and requires the use of Monte-Carlo collision engine [e.g., *Chanrion and Neubert*, 2008] to modeling interaction between particles.

For both approaches (i.e, fluid or PIC), the simulation of optical emissions associated with TLEs, and especially for sprite streamers requires to use a spectroscopic model

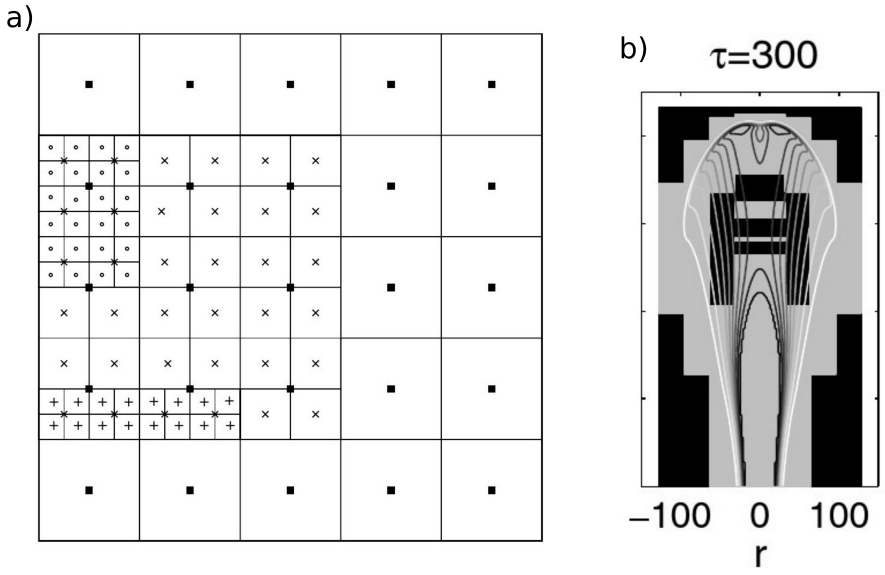

Figure 5: Illustration of Adaptive Mesh Refinement (AMR) in streamer simulation. a) Nested grid used for the computation. Regions of interest have finer grids while others regions have coarse grids. b) Grid used for the computation of continuity equations as done in [*Montijn et al.*, 2006]. The black cells are coarse grids while grey shades correspond to finer grids. Adapted from [*Montijn et al.*, 2006].

[e.g., *Liu and Pasko*, 2004; *Gordillo-Vázquez et al.*, 2011, 2012; *Qin and Pasko*, 2015; *Ihaddadene and Celestin*, 2017; *Janalizadeh and Pasko*, 2019]. Typically, these models calculate the excitation frequency associated with a specific excited state and its associated deexcitation processes from a higher energy level to a lower one. In case of sprite streamers, spectroscopic observations during campaigns [e.g., *Mende et al.*, 1995; *Sentman et al.*, 1995; *Hampton et al.*, 1996; *Milikh et al.*, 1998; *Morrill et al.*, 1998; *Suszcynsky et al.*, 1998; *Armstrong et al.*, 1998; *Gerken et al.*, 2000; *Bucsela et al.*, 2003; *Blanc et al.*, 2004; *Kanmae et al.*, 2010; *Siefring et al.*, 2010; *Heavner et al.*, 2010; *Jehl et al.*, 2013] allow to identify the useful spectroscopic bands to study sprites and others TLEs from ground-based and space observations. The most interesting transitions are: The Lyman-Birge-Hopfiled (LBH) ($N_2(a^1\Pi_g \rightarrow X^1\Sigma_u^+)$), the first positive band system ($N_2(B^3\Pi_g \rightarrow A^3\Sigma_u^+)$), the second positive band system ($N_2(C^3\Pi_u \rightarrow B^3\Pi_g)$), and the

first negative band system of the nitrogen positive ion ($N_2{}^+\left(B^2\Sigma_u^+ \rightarrow X^2\Sigma_g^+\right)$). In the literature, these observations are studied in detail using spectroscopic quantum transition models [e.g., *Gordillo-Vazquez*, 2010; *Gordillo-Vázquez et al.*, 2011, 2012; *Parra–Rojas et al.*, 2013].

TARANIS, standing for Tool for the Analysis of RAdiation from lightNIng and Sprites [*Lefeuvre et al.*, 2008] was a mission of the French space agency (CNES) dedicated to the study of TLEs and Terrestrial Gamma ray Flashes (TGFs). TGFs are intense and brief bursts of gamma rays produced within thunderstorms [e.g., *Fishman et al.*, 1994; *Dwyer et al.*, 2012]. An illustration of the TARANIS payload with its instruments is shown in Figure 6. The mission design follows on from previous space missions such

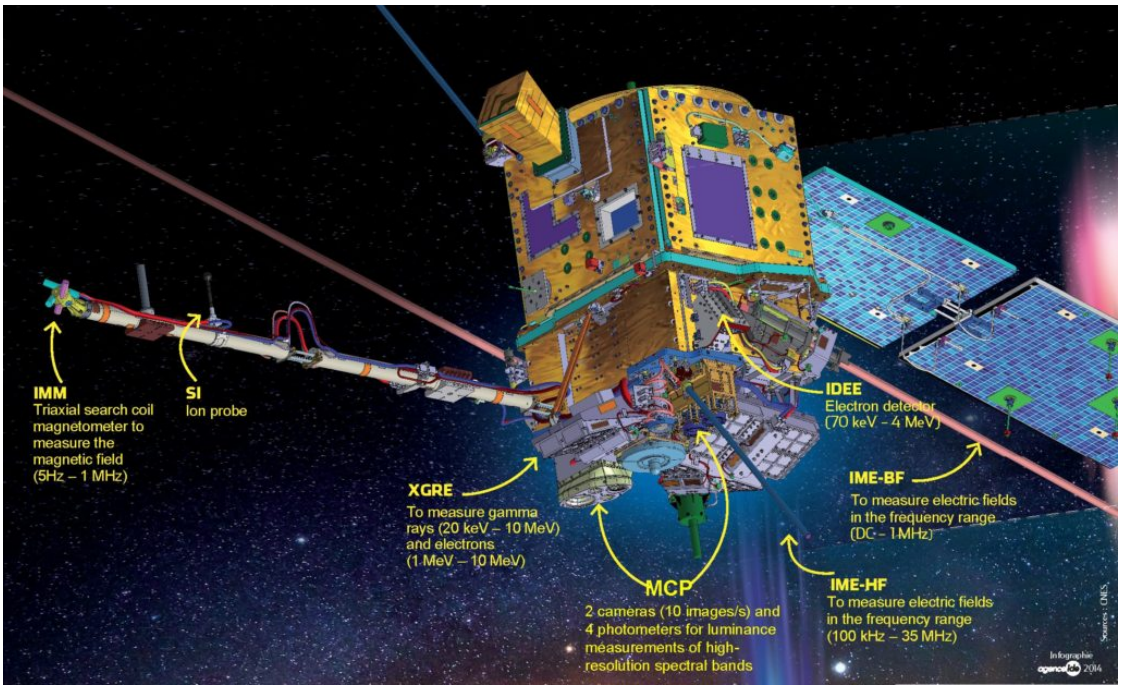

Figure 6: Illustration of TARANIS payload. Yellow arrows indicate the name and the role of the scientific instruments onboard the spacecraft. Credits: CNES.

as the Lightning and Sprite Observations (LSO) [*Blanc et al.*, 2004; *Farges and Blanc*, 2016] and the Imager for Sprites and Upper Atmospheric Lightning (ISUAL) [*Chern*

et al., 2003; *Frey et al.*, 2016], which operated on board the Formosat-2 satellite from 2004 to 2016. It is worth mentioning that recent missions such as GLIMS *Sato et al.* [2015] and ASIM *Neubert et al.* [2019] on board the International Space Station had goals partly overlapping those of TARANIS.

The PhD research described in this thesis has been carried out with a view to use the reported results in application to TARANIS observations. Unfortunately, TARANIS launch (November 17$^{\text{th}}$, 2020) was a failure resulting in the complete loss of the satellite. The results presented in this thesis are still beneficial to the scientific community at large and can be applied to other past and future space-based observations as demonstrated in Chapter IV.

TARANIS would have operated for at least 2 years, at 676 km altitude on a sun-synchronous orbit. The mission of the spacecraft consisted in obtaining various kinds of data on TLEs and TGFs, in nadir-viewing geometry. In this configuration, TARANIS would have been able to simultaneously measure optical, particle, and radio emissions relative to these phenomena. In order to achieve its misssion, TARANIS was equipped with the following instruments:

MCP A set of two microcameras operating at around 10 fps with a field of view of 500 km at ground level. The camera MCS observed at 762 ± 5 nm to record both light emission from lightning and TLEs. The camera MCE observed at 777 ± 5 nm to record only light emission from lightning. MCP also had four photometers sampling at 20 kHz for the on-board identification and the study of TLEs in four spectral bands summarized in the table 2.

IME-BF was a low frequency (DC to 1 MHz) electric antenna.

IME-HF was high frequency (100 kHz to 35 MHz) electric antenna.

IMM was a triaxis magnetometer (search-coil) measuring the magnetic field from 5 Hz to 1 MHz.

Instrument	Wavelength	Phenomena
PH1	160 nm to 260 nm	TLE
PH2	337 ± 5 nm	TLE + lightning
PH3	762 ± 5 nm	TLE + lightning
PH4	600 nm to 900 nm	Lightning

Table 2: Distinctive features of the four MCP photometers. Adaptated from *Farges et al.* [2018].

XGRE was an X-and gamma ray scintillator made of three detectors to measure X and gamma photons between 20 keV-10 MeV, and relativistic electrons between 1 MeV-10 MeV.

IDEE was a set of two high-energy electron detectors to measure the spectrum and their pitch angle.

Their respective position on TARANIS is illustrated in Figure 6.

Because TARANIS would have operated in a nadir-viewing geometry, the flux of photons produced by TLEs is integrated over a vertical line of sight implying a loss of information about the altitude TLEs.

The purpose of the present PhD thesis is to improve the understanding of streamer discharge emissions through the development of a series of models and predictions that will strongly support the interpretation TLE observations from the ground and from space with a particular emphasis on sprites. The next chapter presents various modeling techniques used in the design of the very efficient sprite streamer model developed in the course of the PhD research program. In the chapter III, we use the newly developed model to make an original prediction of HF-VHF emissions produced by streamer collisions in sprites that should have been observable by TARANIS. Chapter IV presents a spectroscopic method to infer specific properties of sprite streamers such as their heights and maximum fields from space nadir-viewing geometry observation. Finally, in the chapter V, we present simulation results of unprecedentedly long streamers propagating

through several scale heights of air density and analyze their physical properties, as well as demonstrating the dependence of the exponential expansion rate of streamers on the size of the initial inhomogeneity. We finally conclude this manuscript summarizing the main results obtained and their impact on our understanding of TLEs.

II Streamer Modeling

Our modeling of streamers consists in taking four aspects into account:

- Electric field produced by the charged species including electrons and, positive and negative ions. In practice, it is calculated from the electric potential obtained through Poisson's equation.
- Motion of charged species: due to the presence of an electric field, charged species are in motion. The modeling of this displacement is simulated in solving the drift-diffusion equation for each species.
- Photoionization processes are induced by the electron impacts exciting N_2 molecules in the air, which in turn release UV photons with sufficient energy to ionize ambient O_2 molecules in the vicinity of the streamer head. Photoionization affects are computed through the three-group SP_3 model [*Bourdon et al.*, 2007].
- Chemical processes are produced by the electric field, which is sufficiently strong to energize electrons that in turn produce ionization of air molecules (source term). On the other hand, when the electric field becomes weak, attachment processes onto oxygen molecules dominate leading to a diminution of electrons and ions.

Written in a mathematical way, we have to solve the set of non-linearly coupled equations below:

$$\nabla^2\phi = -\frac{q}{\epsilon_0}\left(n_p - n_e - n_n\right) \tag{1}$$

$$\partial_t n_e + \vec{\nabla}\cdot\left(n_e\vec{v_e} - D_e\vec{\nabla}n_e\right) = \left(\nu_i - \nu_{a_2} - \nu_{a_3}\right)n_e - \beta_{ep}n_e n_p + S_{ph} \tag{2}$$

$$\partial_t n_p + \vec{\nabla}\cdot\left(n_p\vec{v_p} - D_p\vec{\nabla}n_p\right) = \nu_i n_e - n_p\left(\beta_{ep}n_e - \beta_{np}n_n\right) + S_{ph} \tag{3}$$

$$\partial_t n_n + \vec{\nabla}\cdot\left(n_n\vec{v_n} - D_n\vec{\nabla}n_n\right) = \left(\nu_{a_2} + \nu_{a_3}\right)n_e - \beta_{np}n_n n_p \tag{4}$$

$$S_{\text{ph}} = \sum_j A_j p_{O_2} c\xi\Psi_{SP_3,0,j} \tag{5}$$

where ϕ is the electric potential from which the electric field $\vec{E}$ is derived from $\vec{E} = -\nabla\phi$. The terms n_k, D_k and $\vec{v_k}$ are the density, the diffusion coefficient, and velocity of the species k computed as $\vec{v_k} = \text{sign}\,(e)\mu_k\vec{E}$, which can be electrons (subscript e), positive ions (subscript p) or negative ions (subscript n). The chemical reaction model is based on the ionization frequency ν_i, the two-body attachment ν_{a_2} the three-body attachment ν_{a_3}, the electron-positive ion recombination frequency β_{ep} and negative-positive ion recombination frequency β_{np}. S_{ph} corresponds to the photoionization source term, A_j is a fit coefficient associated with the three-group SP_3 method, p_{O_2} is partial pressure of oxygen, c is the speed of light in vacuum, ξ is the photoionization efficiency (see Section II.4) and $\Psi_{SP_3,0,j}$ is the SP_3 approximation term of the isotropic part of the photon distribution function.

The code produced by the implementation of the equations (1)-(5) is named Electrodynamic Modeling for Sprite Streamer (EMSS), and its flowchart is illustrated in the Figure 7. The equation (1) is Poisson's equation (see Section II.2), equations (2)-(4) are the drift-diffusion equations for charged species (see Section II.3), and (5) is the final photoionization equation derived within the SP_3 model *Bourdon et al.* [2007] (see Section II.4). To simulate light emissions produced by the streamer, we have built a spectroscopic model (see Section II.6). We also use a radio model to calculate the electromagnetic radiation produced by a streamer (see Section II.7). To validate our implementation, a validation of our model with respect to results from literature was conducted (see Section II.9). The next subsections describe the implementation of these equations in our model dedicated to the propagation of streamers in air.

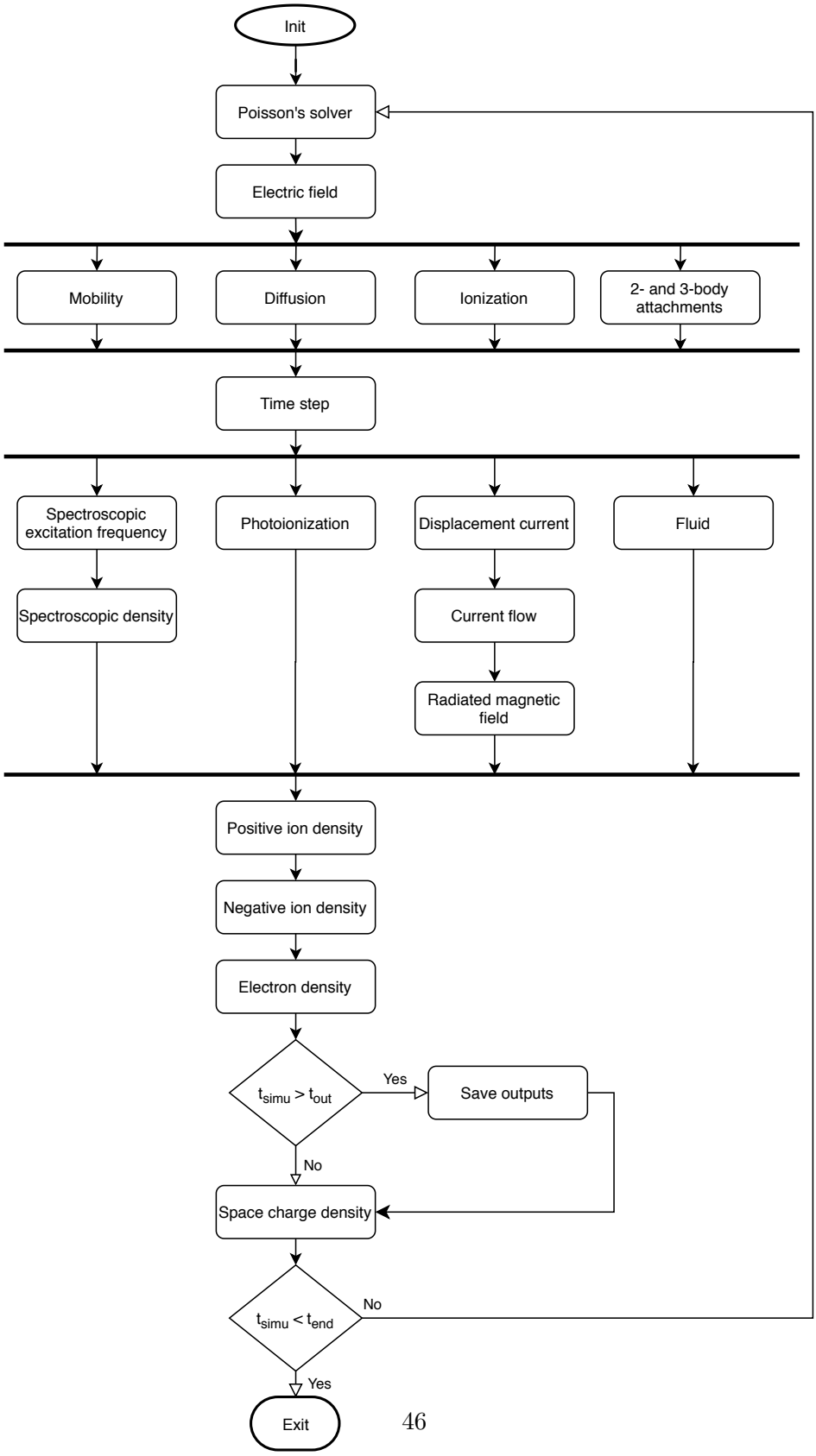

Figure 7: General flowchart illustrating the streamer model developed in the course of the PhD research program. t_{simu} corresponds to the physical time of the simulation, t_{out} is the physical time at which simulation results must be saved, and t_{end} is the physical time at which the simulation must end. The bold horizontal black lines are barriers. Blocks horizontally aligned can be concurrently executed with respect to the master thread. However, within blocks parallel programming is also used.

II.1 Numerical grid

The streamer model is based on a 3-D axisymmetric regular grid as shown in Figure 8.

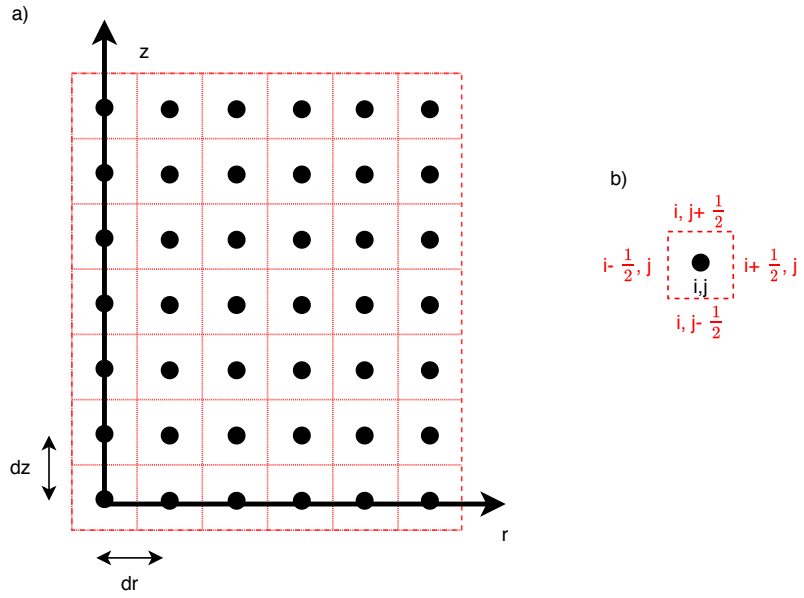

Figure 8: a) The 3-D axisymmetric grid used in our streamer model. Black points correspond to scalar values (e.g., electric potential, density) while red dashed lines correspond to interfaces, which are used for vectorial quantities (e.g., fluxes, electric field). b) Description of the notation used for one cell (i, j). Index i locates the position along the r-axis while index j locates position along the z-axis. Interfaces are denotated with a term $\pm\frac{1}{2}$.

The filamentary shape of streamers leads to the use of cylindrical coordinates. We also assume azimuthal symmetry ($\partial_\theta = 0$). We can write the area of elemental surfaces parallel and perpendicular to the z-axis for a constant radial coordinate r respectively, (equations (6) and (7)):

$$\mathrm{d}S_r = r\,\mathrm{d}\theta\,\mathrm{d}z \tag{6}$$

$$\mathrm{d}S_z = r\,\mathrm{d}r\,\mathrm{d}\theta \tag{7}$$

and the volume of one grid cell (equation (8)).

$$\mathrm{d}V = r\,\mathrm{d}r\,\mathrm{d}\theta\,\mathrm{d}z \tag{8}$$

Considering the symmetry assumption, integration over elemental surfaces leads to:

$$S_r = 2\pi\Delta z\left(r_i + \frac{\Delta r}{2}\right) \tag{9}$$

$$S_z = \pi\left[\left(r_i + \frac{\Delta r}{2}\right)^2 - \left(r_{i-1} + \frac{\Delta r}{2}\right)^2\right] \tag{10}$$

$$V = \pi\Delta z\left[\left(r_i + \frac{\Delta r}{2}\right)^2 - \left(r_{i-1} + \frac{\Delta r}{2}\right)^2\right] \tag{11}$$

where i is the grid index for the radial coordinate. In the vicinity of the axis (i.e., $r \to 0$, we get:

$$S_r = \pi\Delta r\Delta z \tag{12}$$

$$S_z = \pi\left(\frac{\Delta r}{2}\right)^2 \tag{13}$$

$$V = \pi\Delta z\left(\frac{\Delta r}{2}\right)^2 \tag{14}$$

Beside the spatial aspect in the code, we also have to take the time component into account. The choice of the space scale is mainly determined by the length of the streamer and the smallest space scale that needs to be captured. Usually, a mesh size of 8 $\frac{N_0}{N}$ µm is used, where N and N_0 are the local and ground-level air densities. However, for large streamers ($\geq 5\,\mathrm{km}$) we increase the mesh size to 141 $\frac{N_0}{N}$ µm. These two parameters infer the number of points for both r and z directions, which in turns affect the memory and CPU time consumption. The same approach for the time is applied since we want to capture the smallest relevant time scale of the streamer physics. In our model, the time scale of the streamer is driven by five physical processes: the

ionization $\mathrm{d}t_{\mathrm{ioni}}$ and attachment $\mathrm{d}t_{\mathrm{atta}}$ processes, the spectroscopic lifetime $\mathrm{d}t_{\mathrm{spectro}}$, the Courant–Friedrichs–Lewy (CFL) condition $\mathrm{d}t_{\mathrm{CFL}}$ (specifying the temporal propagation of the solution at a given speed with respect to the mesh size) and the dielectric relaxation time (Maxwell time) $\mathrm{d}t_{\mathrm{M}}$ given by:

$$\mathrm{d}t_{\mathrm{ioni}} = \frac{1}{\nu_i} \tag{15}$$

$$\mathrm{d}t_{\mathrm{atta}} = \min\left(\frac{1}{\nu_{a2}}, \frac{1}{\nu_{a3}}\right) \tag{16}$$

$$\mathrm{d}t_{\mathrm{CFL}} = \min\left(\frac{\mathrm{d}r}{v_r}, \frac{\mathrm{d}z}{v_z}\right) \tag{17}$$

$$\mathrm{d}t_{\mathrm{M}} = \frac{\epsilon_0}{e\mu_e n_e} \tag{18}$$

$$\mathrm{d}t_{\mathrm{spectro}} = \min\left(\frac{1}{\tau_{\mathrm{LBH}}}, \frac{1}{\tau_{1\mathrm{PN}_2}}, \frac{1}{\tau_{2\mathrm{PN}_2}}, \frac{1}{\tau_{1\mathrm{NN}_2}}\right) \tag{19}$$

where τ_{LBH}, $\tau_{1\mathrm{PN}_2}$, $\tau_{2\mathrm{PN}_2}$, $\tau_{1\mathrm{NN}_2}$ are the lifetimes associated with the spectroscopic band systems in subscript as explained in the section II.6. Since we are looking for the smallest time scale, the time step $\mathrm{d}t$ is defined based on the minimum value over the whole grid among these five physical processes. Following *Vitello et al.* [1994], we add the coefficients C_{ioni}, C_{atta}, C_{spectro}, C_{CFL}, and C_{M} to obtain a finer time step compared to the smallest scale:

$$\mathrm{d}t = \min\left(C_{\mathrm{ioni}}\mathrm{d}t^{i,j}_{\mathrm{ioni}}, C_{\mathrm{atta}}\mathrm{d}t^{i,j}_{\mathrm{atta}}, C_{\mathrm{spectro}}\mathrm{d}t^{i,j}_{\mathrm{spectro}}, C_{\mathrm{CFL}}\mathrm{d}t^{i,j}_{\mathrm{CFL}}, C_{\mathrm{M}}, \mathrm{d}t^{i,j}_{\mathrm{M}}\right) \tag{20}$$

In our model, we set $C_{\mathrm{ioni}} = C_{\mathrm{atta}} = C_{\mathrm{spectro}} = 0.05$ and $C_{\mathrm{CFL}} = C_{\mathrm{M}} = 0.5$ following *Bourdon et al.* [2007].

In principle, we would only need to use the time scales given by the equations (15)-(18) which correspond to the electrodynamic time scales of streamers. However, simulations at an altitude of 80 km are dominated by the time scale of spectroscopy. At these altitudes, it is typically 1000 times shorter than the dielectric relaxation time leading to

very long simulations. Therefore, we separate the spectroscopic computation from the rest of the simulation. The spectroscopic part is calculated at each time step until it catches up with the time of the simulation. We go into more details about that point in Section II.6.

II.2 Poisson's equation

Poisson's equation (1) links the electric potential with the density of charged species. In our model, Poisson's equation is solved assuming the axisymmetry of the system for an electric potential ϕ ($\partial_\theta \phi = 0$). In cylindrical coordinates, the Laplacian can hence be written as:

$$\nabla^2 \phi = \frac{1}{r}\partial_r \phi + \partial_r^2 \phi + \partial_z^2 \phi \tag{21}$$

It is convenient to use L'Hôpital's rule near the axis (i.e., $r \to 0$) of the simulation domain to obtain:

$$\lim_{r\to 0} \nabla^2 \phi = 2\partial_r^2 \phi + \partial_z^2 \phi \tag{22}$$

The discretization of the equations (21) and (22) is realized through a five point stencil as shown in the Figure 9 where the value in the red circle is updated according to its black neighbors. The first order derivative is approximated with a first order forward scheme while the second derivates are approximated with a second-order centered scheme :

$$\partial_r \phi \simeq \frac{1}{\Delta r}\left(\phi_{i+1,j} - \phi_{i,j}\right) + \mathcal{O}\left(\Delta r\right) \tag{23}$$

$$\partial_r^2 \phi \simeq \frac{1}{\Delta r^2}\left(\phi_{i+1,j} - 2\phi_{i,j} + \phi_{i-1,j}\right) + \mathcal{O}\left(\Delta r^2\right) \tag{24}$$

$$\partial_z^2 \phi \simeq \frac{1}{\Delta z^2}\left(\phi_{i,j+1} - 2\phi_{i,j} + \phi_{i,j-1}\right) + \mathcal{O}\left(\Delta r^2\right) \tag{25}$$

Substituting these formulas in equations (21)-(22), we get:

$$\phi_{1,j} = \frac{1}{w_{\mathrm{C}}}\left[w_{\mathrm{WE}}\phi_{2,j} + w_{\mathrm{NS}}\left(\phi_{1,j-1} + \phi_{1,j+1}\right) + \frac{\rho_{1,j}}{\epsilon_0}\right] \tag{26}$$

$$\phi_{i,j} = \frac{1}{w_{\mathrm{C}}}\left[w_{\mathrm{W}}\phi_{i-1,j} + w_{\mathrm{E}}\phi_{i+1,j} + w_{\mathrm{NS}}\left(\phi_{i,j-1} + \phi_{i,j+1}\right) + \frac{\rho_{i,j}}{\epsilon_0}\right] \tag{27}$$

where $\rho_{i,j} = \rho\left(r_i, z_j\right)$ is the charge density at the point indexed (i, j). The values for the coefficients w_{C}, w_{WE}, and w_{NS} for the equation (26) are:

$$w_{\mathrm{C}} = \frac{4}{\Delta r^2} + \frac{4}{\Delta z^2} \tag{28}$$

$$w_{\mathrm{WE}} = \frac{4}{\Delta r^2} \tag{29}$$

$$w_{\mathrm{NS}} = \frac{1}{\Delta z^2} \tag{30}$$

and for the coefficients w_W, w_E in the equation (27):

$$w_{\mathrm{C}} = \frac{1}{r_i \Delta r} + \frac{2}{\Delta r^2} + \frac{2}{\Delta r^2} \tag{31}$$

$$w_{\mathrm{E}} = \frac{1}{r_i \Delta r} + \frac{1}{\Delta r^2} \tag{32}$$

$$w_{\mathrm{W}} = \frac{1}{\Delta r^2} \tag{33}$$

$$w_{\mathrm{NS}} = \frac{1}{\Delta z^2} \tag{34}$$

Based on the literature about streamer modeling [e.g., *Guo and Wu*, 1993; *Kulikovsky*, 1995; *Liu and Pasko*, 2004; *Bourdon et al.*, 2007; *Qin et al.*, 2011; *Ihaddadene and Celestin*, 2015; *Janalizadeh and Pasko*, 2019], we choose to use the method of Successive Over-Relaxation (SOR) [e.g., *Golub and Van Loan*, 1996; *Press et al.*, 2007], which is an optimization of the Gauss-Seidel method because it converges faster to the guessed

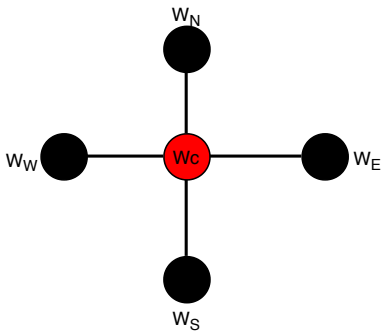

Figure 9: Five point stencil used to solve Poisson's equation. The red disk corresponds to the location of the solution that will be updated using its neighbor values in black.

solution. The value of the electric potential at the iteration $k+1$ is given by:

$$\phi_{i,j}^{k+1} = \omega\tilde{\phi}_{i,j} + (1-\omega)\phi_{i,j}^{k} \tag{35}$$

where $\tilde{\phi}_{i,j}$ is the electric potential obtained from equations (26) and (27), ω is the relaxation factor, and $\phi_{i,j}^{k}$ is the value of the electric potential at the iteration k. The value of ω can be either static or dynamic. In our implementation, we use a dynamic relaxation factor updated according to the Chebyshev acceleration algorithm [e.g., *Golub and Van Loan*, 1996; *Press et al.*, 2007]. The value of ω is updated according to the recursive formula:

$$\begin{cases} \omega^{(0)} = 1 \\ \omega^{(\frac{1}{2})} = \dfrac{1}{1-\frac{1}{2}\rho^2} \\ \omega^{(k+\frac{1}{2})} = \dfrac{1}{1-\frac{1}{4}\rho^2\omega^{(k)}} \end{cases} \tag{36}$$

where ρ is the spectral radius of the matrix coefficient illustrated in Figure 10. In our case, this matrix can be analytical expressed by:

$$\rho = \frac{1}{2}\left[\cos\left(\frac{\pi}{N_r}\right) + \cos\left(\frac{\pi}{N_z}\right)\right] \tag{37}$$

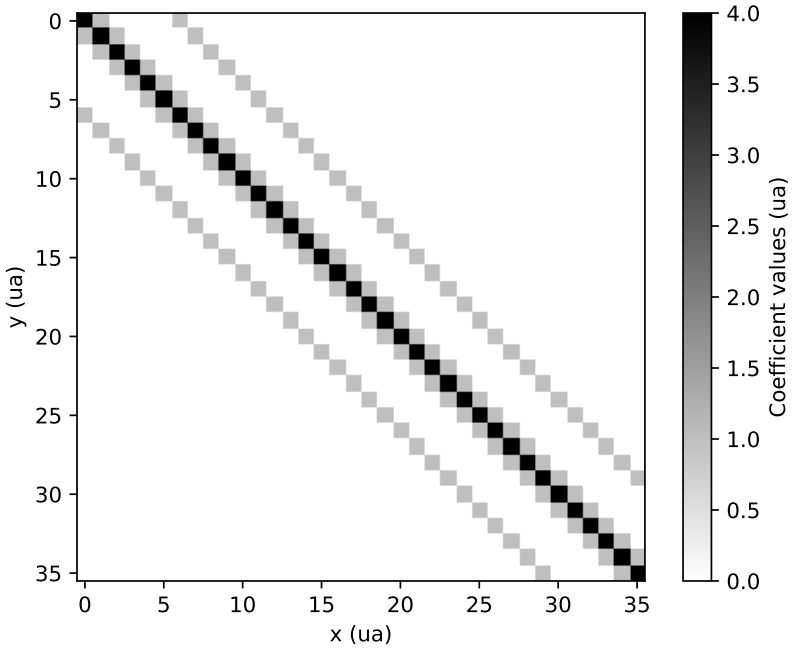

Figure 10: Absolute value of the coefficient matrix obtained from the discretization of Poisson's equation assuming a square domain of 32 points. More than 97 % of the matrix is composed of null values.

The optimal relaxation factor is reached at the limit $\lim_{n\to+\infty} \omega^{(n)}$. In practice, the convergence of ω is reached after a dozen of iterations.

The convergence of the solver is halted when the norm defined by:

$$\epsilon = \frac{\sum_{i,j} \left(\phi_{i,j}^{k+1} - \phi_{i,j}^{k}\right)^2}{\sum_{i,j} \left(\phi_{i,j}^{k}\right)^2} \tag{38}$$

is strictly less than 10^{-9}. This value is obtained through experimentations. It satisfies both an accurate solution and a correct speed of convergence.

In terms of computation time, Poisson's solver described above is one of the two bottlenecks of the streamer code as it is used to solve both Poisson's equation and the SP_3model for the photoionization (see Section II.4). To reduce its impact, we use the

Red and Black implementation (R&B) [e.g., *Evans*, 1984]. The idea is to split the domain in two "colors" as illustrated in the Figure 9. All the values at red points are updated from the values at their black neighbors, then in a second step, black neighbors are updated with the newest red-point-based values. In the case of the stencil we use, each red values of the grid are, from the point of view concurrent access, independent, meaning we can simultaneously update all red values. The same process is also applied with the black values for the same reason. As red and black values are independent at each update, this approach offers opportunities to use shared memory (e.g., OpenMP), distributed memory (e.g., MPI) or hybridization OpenMP-MPI. We also point out that R&B implementation can be also implemented on GPUs providing, from our experience, a real gain in speed.

Figure 10 illustrates the sparseness of the coefficient matrix where a more than 97 % of the matrix is null meaning only a few coefficients are used for the computation of solutions (greys and black cells). This feature is convenient to reduce the memory footprint of the both Poisson's and SP_3 solver.

Figure 11 shows the workflow of the Poisson's solver in a global view. In the case of shared memory implementation (current implementation of the code), the parallelization occurs on loops for the update of red and black values.

To solve Poisson's equation, we need to set boundary conditions namely Dirichlet boundary conditions. For instance, one could fix the electric potential at the domain boundaries. However, when the streamer will be in the vicinity of the edges of the domain, we can expect some interaction between the streamer and the edge. In the aim to produce a more realistic simulation and also reduce the size of the domain, the electric potential at the boundaries is dynamically updated as a function of the charge inside the domain [*Liu and Pasko*, 2006]. A homogenous electric field acting as a background ambient electric field is also defined. Because of the linearity of the Laplacian operator

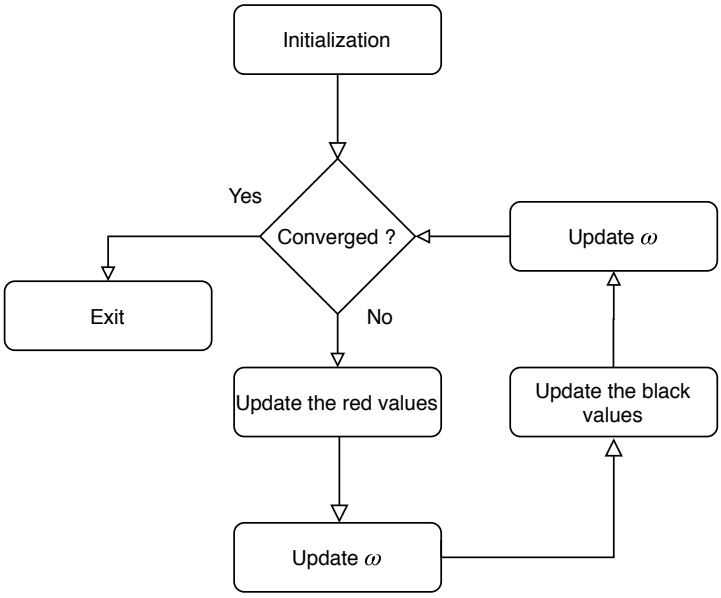

Figure 11: Generic workflow of the Poisson's solver implemented with the Red and Black (R&B) approach. The value of ω is updated according to the Chebyshev acceleration (36).

in the equation (1), the electric potential can be written as:

$$\phi = \phi_L + \phi_{\texttt{streamer}} \tag{39}$$

where ϕ_L is the part of the potential giving rise to the externally sourced ambient homogeneous electric field often referred as Laplacian electric field (since it is Laplacian-free). $\phi_{\texttt{streamer}}$ is the space charge electric potential given by *Liu and Pasko* [2006]:

$$\phi_{\texttt{streamer}} = \frac{1}{4\pi\epsilon_0} \iint \frac{2\pi r \rho_Q\left(r,z\right) 4\mathcal{K}\left(k\right)}{\sqrt{\left(r_b+r\right)^2+\left(z_b-z\right)^2}\, 2\pi} \mathrm{d}r\mathrm{d}z \tag{40}$$

where subscripts b denotes borders, respectively. ρ_Q is the space charge density at the coordinates (r,z). $\mathcal{K}$ corresponds to the complete elliptic integral of the first kind and k is defined as $k = \frac{4r_b r}{(r_b+r)^2+(z_b-z)^2}$. The computation of the integral from the equation (40) is an expensive numerical task. To decrease the corresponding time-consumption

we use four techniques:

1. The computation of the term $\phi_{\texttt{streamer}}$ is not performed at all the points over the boundaries, and a linear interpolation is applied to recover missing values. This approach is possible because the variation of the electric potential on the borders of the simulation domain is smooth away from high charge density regions.

2. The computation of the term $\phi_{\texttt{streamer}}$ implies to evaluate the term ρ_Q within the domain. However, the charge is mainly concentrated in a compact region named streamer head as shown in the Figure 12 by the colored shell for both streamers. This observation allows us to reduce the computation time in only considering the highest charge density so that the computation is done if $\rho_Q\left(r_d, z_d\right) > \frac{\max\left(|\rho_Q|\right)}{1000}$ following *Bourdon et al.* [2007].

3. The computation of $\mathcal{K}$ can be realized using either a look-up table or a direct computation. In our implementation, we use the direct computation using the efficient Carlson's algorithm [DLMF].

4. The computation of ϕ_{streamer} in the equation (40) can be done in an independant manner meaning that it is well suited for multiprocessing computation.

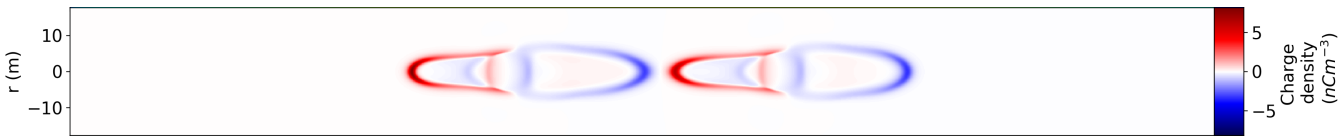

Figure 12: 2-D cross sectional view of the charge density of two double-headed streamers at an altitude of 70 km. The blue color corresponds to a negative net charge while the red color corresponds to an excess positive charge.

II.3 Drift-diffusion equations

The implementation of a fluid method to solve the non-linearly coupled drift-diffusion equations (2)-(4) is a critical part of the model because of the existence of strong density

gradients localized in the vicinity of the streamer head. Such gradients tend to create numerical oscillations of the solution leading, in the worst case, to aberrant results. Several kinds of numerical schemes have been reported in the literature to capture these gradients in the framework of streamer simulations. We can cite here the Scharfetter-Gummel scheme [e.g., *Kulikovsky*, 1995; *Liu and Pasko*, 2004; *Bourdon et al.*, 2007], the Flux Corrected-Transport method (FCT) [e.g., *Boris and Book*, 1973; *Zalesak*, 1979; *Bourdon et al.*, 2007; *Zalesak*, 2012; *Qin et al.*, 2013b; *Ihaddadene and Celestin*, 2015], or second-order piecewise linear flux-limiting technique [e.g., *Mignone*, 2014; *Janalizadeh and Pasko*, 2019]. In our model we use the FCT method. The idea underlying the FCT method is to mix two schemes, one with a low-order and inherently diffusive scheme and a high-order inherently dispersive scheme. In the aim to attenuate oscillations, the FCT will track gradients and mix low-order and high-order schemes to produce an oscillation-free solution.

To solve the equations (2)-(4), we use a Finite Volume Method (FVM), which consists of solving the equations in their volumic integral form. This approach has the great advantage to be conservative and then well adapted to modeling of fluid mechanics. Using the equation (2) and integrating it over the volume of a cell leads to:

$$\int_V \partial_t n_e \mathrm{d}V + \int_V \vec{\nabla} \cdot \left(n_e \vec{v_e} - D_e \vec{\nabla} n_e \right) \mathrm{d}V = \int_V \left[\left(\nu_i - \nu_{a_2} - \nu_{a_3} \right) n_e - \beta_{ep} n_e n_p + S_{ph} \right] \mathrm{d}V \tag{41}$$

Using Gauss' theorem, we obtain:

$$\partial_t \int_V n_e \mathrm{d}V + \int_{\partial V} n_e \vec{v_e} \cdot \mathrm{d}\vec{S} - \int_{\partial V} D_e \vec{\nabla} n_e \cdot \mathrm{d}\vec{S} = \int_V \left[\left(\nu_i - \nu_{a_2} - \nu_{a_3} \right) n_e - \beta_{ep} n_e n_p + S_{ph} \right] \mathrm{d}V \tag{42}$$

This formulation expresses the variation of the density as a difference of a flux in and out of each grid cell for the second and third terms of the equation (42). The first term is the time variation of the electron density within the cell. As we consider a 3-D axisymetric

model, fluxes lie both along the r and z directions, we can write for the second term in (42):

$$\int_{\partial V} n_e \vec{v_e} \cdot \mathrm{d}\vec{S} = \sum F = F_{i+\frac{1}{2},j} - F_{i-\frac{1}{2},j} + F_{i,j+\frac{1}{2}} - F_{i,j-\frac{1}{2}} \tag{43}$$

where the subscript $i+\frac{1}{2}$ describes the flux along the r-axis and $j+\frac{1}{2}$ for the z- axis. The same computation can be done for the third term of the equation (42). The projected fluxes F are written as:

$$F_k = n_{e_k} v_{e_{k'}} S_{k'} \tag{44}$$

where the subscript k denotes the cell (i,j), and k' denotes either $(i+\frac{1}{2},j)$ or $(i,j+\frac{1}{2})$, and $S_{k'}$ is the surface. The term $v_{e_{k'}}$ depends on the mobility of the considered species, which is evaluated using coefficients provided by *Moss et al.* [2006].

The diffusion term in the equation (42) is evaluated at the first order as:

$$F^D_{i+\frac{1}{2},j} = \frac{1}{\mathrm{d}r} D_{e_{i,j}} \left(n_{e_{i+1,j}} - n_{e_{i,j}} \right) S_{i+\frac{1}{2},j} \tag{45}$$

where the superscript D indicates the diffusion term of the equation (42). For electrons, this term is evaluated according to *Morrow and Lowke* [1997]. The ion diffusion is neglected.

However, FCT is not sufficient to fully remove oscillations on its own. In addition to the FCT, we combine it to a Lax-Wendroff scheme [e.g., *Press et al.*, 2007] to significantly reduce simulations over time.

The evaluation of the new value of electron, and positive and negative ion densities is illustrated by the workflow in Figure 13.

The first-order scheme upwind deduced from the equation (44):

$$F^l_{i+\frac{1}{2},j} = n_{e_{i,j}} v_{i+\frac{1}{2},j} S_{i+\frac{1}{2},j} \tag{46}$$

for the right face of the cell ($v_{i+\frac{1}{2},j>0}$). The upperscript l designates the low-order nature

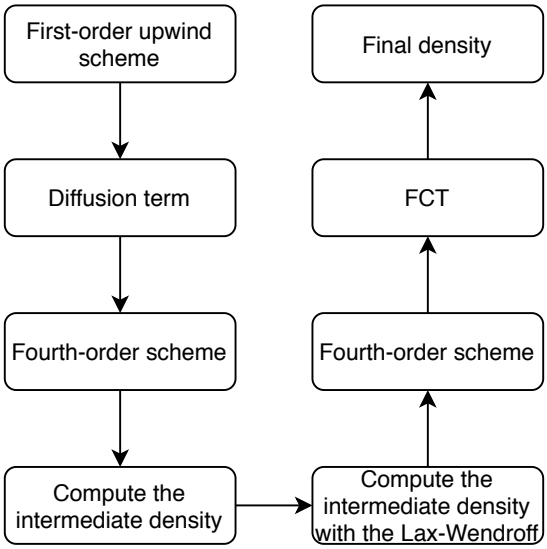

Figure 13: Workflow of the numerical drift-diffusion equation solver.

of the scheme. For the same face of the cell, the fourth-order scheme writes:

$$F^{h}_{i+\frac{1}{2},j} = \left[\frac{7}{12}\left(\tilde{n}_{e_i} + \tilde{n}_{e_{i+1}}\right) - \frac{1}{12}\left(\tilde{n}_{e_{i+2}} + \tilde{n}_{e_{i-1}}\right)\right] v_{i+\frac{1}{2},j} S_{i+\frac{1}{2},j} \tag{47}$$

where the superscript h denotes the high-order and the tilde designates the decimal logarithm of the electron density (i.e., $\tilde{n}_{e_i} = \log_{10}(n_{e_i})$). The use of the logarithm is reported in *Ihaddadene* [2016] to damp ripples because it smooths out the electronic density and attenuates the amplitude of the gradient density. The formulation for the other faces can be deduced by replacing subscript indices. The deduction of the coefficients $\frac{7}{12}$ and $\frac{1}{12}$ is explained in *Ihaddadene* [2016]. However, the computation of the fourth-order scheme along the z-axis needs to be combined with an artificial numerical diffusion term [*Boris and Book*, 1973; *Zalesak*, 1979, 2012] to reduce ripples and dramatically improve the efficiency of the FCT:

$$F^{D_{\text{num}}}_{i,j} = \left[\frac{3}{16}\left(n_{e_{i,j+1}} - n_{e_{i,j}}\right) - \frac{1}{16}\left(n_{e_{i,j+2}} - n_{e_{i,j-1}}\right)\right] \left|v_{i,j+\frac{1}{2}}\right| S_{i,j+\frac{1}{2}} \tag{48}$$

The two temporary densities are defined as:

$$n_{e_{i,j}}^{t+\delta t} = n_{e_{i,j}}^{t} - \frac{\Delta t}{V_{i,j}} \left(F^{l}_{i+\frac{1}{2},j} - F^{l}_{i-\frac{1}{2},j} + F^{l}_{i,j+\frac{1}{2}} - F^{l}_{i,j-\frac{1}{2}} \right) \tag{49}$$

$$n_{e_{i,j}}^{t+\frac{\delta t}{2}} = n_{e_{i,j}}^{t} - \frac{\Delta t}{2V_{i,j}} \left(F^{h}_{i+\frac{1}{2},j} - F^{h}_{i-\frac{1}{2},j} + F^{h}_{i,j+\frac{1}{2}} - F^{h}_{i,j-\frac{1}{2}} \right) \tag{50}$$

where Δt is the time step of the simulation given by the equation (20), and $V_{i,j}$ is the volume of the cell (i, j).

The temporary density used for the second stage of the fourth-order scheme is obtained through:

$$n_{e_{i,j}}^{t+\frac{\delta t}{2}} = \frac{1}{12} \left| 5n_{e_{i,j}}^{t+\delta t} + 8n_{e_{i,j}}^{t} - n_{e_{i,j}}^{t-\delta t} \right| \tag{51}$$

where the term $n_{e_{i,j}}^{t-\delta t}$ corresponds to the density at the previous temporal iteration. The absolute value is not present in the original formula. We add it to avoid the apparition of non finite values, either Not a Number (NaN) or infinity (Inf), when the density is close to 0.

A complete description of the FCT can be found in *Boris and Book* [1973] and *Zalesak* [1979]. Here, we summarize it as used in our implementation. First, we have to compute for each axis the antidiffusive fluxes:

$$A_{i+\frac{1}{2},j} = F^{h}_{i+\frac{1}{2},j} - F^{l}_{i+\frac{1}{2},j} \tag{52}$$

$$A_{i,j+\frac{1}{2}} = F^{h}_{i,j+\frac{1}{2}} - F^{l}_{i,j+\frac{1}{2}} \tag{53}$$

where $A_{i+\frac{1}{2},j}$ and $A_{i,j+\frac{1}{2}}$ are the antidiffusive fluxes for the radial and the azimutal axes, respectively. Using the equation (52) and (53), we calculate three logical values for each

axis:

$$C^1_{i+\frac{1}{2},j} = \left\{ A_{i+\frac{1}{2},j} \left(n^{t+\delta t}_{e_{i+1,j}} - n^{t+\delta t}_{e_{i,j}} \right) < 0 \right\} \tag{54}$$

$$C^2_{i+\frac{1}{2},j} = \left\{ A_{i+\frac{1}{2},j} \left(n^{t+\delta t}_{e_{i+2,j}} - n^{t+\delta t}_{e_{i+1,j}} \right) < 0 \right\} \tag{55}$$

$$C^3_{i+\frac{1}{2},j} = \left\{ A_{i+\frac{1}{2},j} \left(n^{t+\delta t}_{e_{i,j}} - n^{t+\delta t}_{e_{i-1,j}} \right) < 0 \right\} \tag{56}$$

From equations (54)-(56), the value of the antidiffusive fluxes from the equation (52) is updated according to:

$$A_{i+\frac{1}{2},j} = \begin{cases} A_{i+\frac{1}{2},j} & \text{if} \quad C^1_{i+\frac{1}{2},j} \wedge \left(C^2_{i+\frac{1}{2},j} \vee C^3_{i+\frac{1}{2},j} \right) \text{is true} \\ 0 & \text{otherwise} \end{cases} \tag{57}$$

Where the notations $\wedge$ and $\vee$ correspond to the operators AND and OR of the Boolean algebra, respectively. The approach stays the same for the radial direction, one just needs to change indexes. According to *Zalesak* [1979], the set of equations (54)-(57) plays a minimal and cosmetic role because of the probability of cases of antidiffusive fluxes directed down gradient in $n_e^{t+\delta t}$ is rare. However, we maintain this set of equations for safety.

In parallel, we search the minimum and the maximum in the density at time t and $t + \delta t$ given by the equations (58) and (59).

$$w^a_{i,j} = \max \left(n_e, n_e^{t+\delta t} \right) \tag{58}$$

$$w^b_{i,j} = \min \left(n_e, n_e^{t+\delta t} \right) \tag{59}$$

From the equations (58) and (59) we deduce the maximum , and minimum, using:

$$w_{i,j}^{\max} = \max\left(w_{i-1,j}^{a}, w_{i,j}^{a}, w_{i+1,j}^{a}, w_{i,j-1}^{a}, w_{i,j+1}^{a}\right) \tag{60}$$

$$w_{i,j}^{\min} = \min\left(w_{i-1,j}^{b}, w_{i,j}^{b}, w_{i+1,j}^{b}, w_{i,j-1}^{b}, w_{i,j+1}^{b}\right) \tag{61}$$

We use the equations (60) and (61) to compute the sum of all antidiffusive fluxes into a cell:

$$P_{i,j}^{+} = \max\left(0, A_{i-\frac{1}{2},j}\right) - \min\left(0, A_{i+\frac{1}{2},j}\right) + \max\left(0, A_{i,j-\frac{1}{2}}\right) - \min\left(0, A_{i,j+\frac{1}{2}}\right) \tag{62}$$

$$P_{i,j}^{-} = \max\left(0, A_{i+\frac{1}{2},j}\right) - \min\left(0, A_{i-\frac{1}{2}}\right) + \max\left(0, A_{i,j+\frac{1}{2}}\right) - \min\left(0, A_{i,j-\frac{1}{2}}\right) \tag{63}$$

and four others quantities that will be used to constrain the flux:

$$Q_{i,j}^{+} = V_{i,j}\left(w_{i,j}^{\max} - n_e^{t+\delta t}\right) \tag{64}$$

$$Q_{i,j}^{-} = V_{i,j}\left(n_e^{t+\delta t} - w_{i,j}^{\min}\right) \tag{65}$$

$$R_{i,j}^{+} = \begin{cases} \min\left(1, \dfrac{Q_{i,j}^{+}}{P_{i,j}^{+}}\right) & \text{if} \quad P_{i,j}^{+} > 0 \\ 0 \quad \text{otherwise} \end{cases} \tag{66}$$

$$R_{i,j}^{-} = \begin{cases} \min\left(1, \dfrac{Q_{i,j}^{-}}{P_{i,j}^{-}}\right) & \text{if} \quad P_{i,j}^{-} > 0 \\ 0 \quad \text{otherwise} \end{cases} \tag{67}$$

Then, we define limiters as:

$$C_{i+\frac{1}{2},j} = \begin{cases} \min\left(R_{i+1,j}^{+}, R_{i,j}^{-}\right) & \text{if} \quad A_{i+\frac{1}{2},j} \geq 0 \\ \min\left(R_{i,j}^{+}, R_{i+1,j}^{-}\right) & \text{otherwise} \end{cases} \tag{68}$$

$$C_{i,j+\frac{1}{2}} = \begin{cases} \min\left(R_{i,j+1}^{+}, R_{i,j}^{-}\right) & \text{if} \quad A_{i,j+\frac{1}{2}} \geq 0 \\ \min\left(R_{i,j}^{+}, R_{i,j+1}^{-}\right) & \text{otherwise} \end{cases} \tag{69}$$

An interesting feature of $C_{i+\frac{1}{2},j}$ and $C_{i,j+\frac{1}{2}}$ is that they range between 0 and 1. Finally, limited fluxes are defined by:

$$AC_{i+\frac{1}{2},j} = C_{i+\frac{1}{2},j} A_{i+\frac{1}{2},j} \tag{70}$$

$$AC_{i,j+\frac{1}{2}} = C_{i,j\frac{1}{2}} A_{i,j+\frac{1}{2}} \tag{71}$$

The new value of the density is given by:

$$\begin{aligned} n_{e_{i,j}}^{t+\delta t} = n_{e_{i,j}}^{t} - \frac{1}{V_{i,j}} \Big(& AC_{i+\frac{1}{2},j} - AC_{i-\frac{1}{2},j} + AC_{i,j+\frac{1}{2}} - AC_{i,j-\frac{1}{2}} \\ & + F^D_{i+\frac{1}{2},j} - F^D_{i-\frac{1}{2},j} + F^D_{i,j+\frac{1}{2}} - F^D_{i,j-\frac{1}{2}} \Big) \end{aligned} \tag{72}$$

Despite the fact that the fluid model is not a bottleneck in the final code, we point out that for long streamers it becomes useful to use multiprocessing implementation. Furthermore, the fluid model given here is well-adapted for such approach and straightforward.

We report that the use of an eight-order scheme is also useful to significantly damp oscillations. It is explicitly written:

$$\begin{aligned} F^h_{i+\frac{1}{2},j} = \Big[& \frac{533}{840} \left(\tilde{n}_{e_{i+1}} + \tilde{n}_{e_i} \right) - \frac{139}{840} \left(\tilde{n}_{e_{i+2}} + \tilde{n}_{e_{i-1}} \right) + \frac{29}{840} \left(\tilde{n}_{e_{i+3}} + \tilde{n}_{e_{i-2}} \right) \\ & - \frac{1}{280} \left(\tilde{n}_{e_{i+4}} + \tilde{n}_{e_{i-3}} \right) \Big] v_{i+\frac{1}{2},j} S_{i+\frac{1}{2},j} \end{aligned} \tag{73}$$

II.4 Photoionization

The photoionization process plays a significant role in the dynamic of sprite streamers. Indeed, the streamer head is a place of strong electric field, which contributes to two processes: ionization and excitation. Under the high electric field in the head of the streamer, N_2 is excited into higher states by electron impact and relaxes in producing UV photons in front of the streamer head. Some of the produced UV photons are

energetic enough to ionize O_2 and increase the electron density in the vicinity of the streamer head. This increase in the electron density allowing the positive streamer to move in the opposite direction of the electron motion.

The simulation of photoionization processes is based on experimental results reported by *Zheleznyak et al.* [1982]. *Liu and Pasko* [2004] give a clear description of the concepts at hand in *Zheleznyak et al.* [1982]'s photoionization model. In our model, we choose to use the method describes by *Bourdon et al.* [2007] named the three-group SP_3. Note that *Janalizadeh and Pasko* [2019] extended this method in taking more high energy states of N_2 molecules capable to ionize O_2 into account. They also provide a general framework for the photoionization calculations in nonthermal gas discharges in air.

The three-group SP_3 developed by *Bourdon et al.* [2007] is based on the resolution of the isotropic part of the photon distribution function given by the effective radiation transfer equation [*Ségur et al.*, 2006; *Bourdon et al.*, 2007]. The main goal of this approach is to speed up computation in replacing the volume integral by a set of elliptic differential equations. The effective monochromatic radiative transfer equation can be written [*Ségur et al.*, 2006; *Bourdon et al.*, 2007]:

$$\vec{\Omega} \cdot \vec{\nabla} \Psi_j \left(\vec{r}, \vec{\Omega} \right) + \lambda_j p_{O_2} \Psi_j \left(\vec{r}, \vec{\Omega} \right) = \frac{n_u(\vec{r})}{4\pi c \tau_u} \tag{74}$$

where $\vec{\Omega}$ is the direction, Ψ_j the photon distribution function, $\lambda_j p_{O_2}$ is the absorption term, $n_u(\vec{r})$ is the density of the radiative excited species u, c the speed of light in vacuum, τ_u is the lifetime of the excited state u, and $\vec{r}$ is the distance between the source and observer. Integrating equation (74) one obtains, the isotropic part of the photon distribution function $\Psi_{0,j}$:

$$\Psi_{0,j} = \iiint_{V'} \frac{n_u(\vec{r})}{c\tau_u} \frac{\exp\left(-\lambda_j p_{O_2} R\right)}{4\pi R^2} \mathrm{d}V' \tag{75}$$

where R is the distance between the source and the observer. Under the assumption

that the isotropic part of the total distribution function $\Psi_0(\vec{r})$ can be written as a linear combination of monochromatic terms $\Psi_{0,j}$:

$$\Psi_0(\vec{r}) = \sum_j \alpha_j \Psi_{0,j}(\vec{r}) \tag{76}$$

where α_j is a constant. The combination of the equations (75) and (76) leads to the photoionization term S_{ph} in equations (2)-(3):

$$S_{\text{ph}} = \sum_j A_j \xi p_{\text{O}_2} \iiint_{V'} \frac{n_u(\vec{r})}{c\tau_u} \frac{\exp(-\lambda_j p_{\text{O2}} R)}{4\pi R^2} \mathrm{d}V' \tag{77}$$

where ξ is a parameter named the photoionization efficiency. S_{ph} is the rate of photoelectron production per unit volume. As part of a preliminary work, we compared results obtained with our implementation of the SP_3 model with the integral formulation of *Zheleznyak et al.* [1982].

$$S_{\text{ph}} = \iiint_{V'} \frac{I(\vec{r}) g(R)}{4\pi R^2} \mathrm{d}V' \tag{78}$$

Equations (77) and (78) are identical under the condition:

$$\frac{g(R)}{p_{\text{O}_2}} = \sum_j A_j \exp(-\lambda_j p_{\text{O}_2} R) \tag{79}$$

where A_j and λ_j are unknown constants. They are defined by a three-exponential fit over experimental results of the term $\frac{g(R)}{p_{\text{O}_2}}$ in the equation (79). The coefficients used are extracted from *Bourdon et al.* [2007] and reported in Table 3. Note that the method can be extended to use more coefficients *Janalizadeh and Pasko* [2019, 2020]. *Ségur et al.* [2006] solve the equation (74) using the Eddington approximation. However, *Bourdon et al.* [2007] have shown that for streamers, the three-group SP_3 is more accurate. Finally,

j	A_j ($\mathrm{cm^{-1}\,Torr^{-1}}$)	λ_j ($\mathrm{cm^{-1}\,Torr^{-1}}$)
1	0.0067	0.0447
2	0.0346	0.1121
3	0.3059	0.5994

Table 3: The three-exponential fitting coefficients used to compute the photoionization for the SP_3 model. The values are reproduced from *Bourdon et al.* [2007].

the photoionization term S_{ph} writes:

$$S_{\mathrm{ph}} = \sum_{j=1}^{3} A_j p_{\mathrm{O_2}} c\xi \Psi_{\mathrm{SP_3,0,j}} \tag{80}$$

where $\Psi_{\mathrm{SP_3,0,j}}$ is given by:

$$\Psi_{\mathrm{SP_3,0,j}} = \frac{\gamma_2\phi_{1,j} - \gamma_1\phi_{2,j}}{\gamma_2 - \gamma_1} \tag{81}$$

with γ_1 and γ_2 expressed as $\gamma_n = \frac{5}{7}\left[1 + (-1)^n 3\sqrt{\frac{6}{5}}\right]$, where $\phi_{1,j}$ and $\phi_{2,j}$ are the solutions of the following equations:

$$\nabla^2\phi_{1,j}\left(\vec{r}\right) - \frac{\left(\lambda_j p_{\mathrm{O_2}}\right)^2}{\kappa_1^2}\phi_{1,j}\left(\vec{r}\right) = -\frac{\lambda_j p_{\mathrm{O_2}}}{\kappa_1^2}\frac{n_u\left(\vec{r}\right)}{c\tau_u} \tag{82}$$

$$\nabla^2\phi_{2,j}\left(\vec{r}\right) - \frac{\left(\lambda_j p_{\mathrm{O_2}}\right)^2}{\kappa_2^2}\phi_{2,j}\left(\vec{r}\right) = -\frac{\lambda_j p_{\mathrm{O_2}}}{\kappa_2^2}\frac{n_u\left(\vec{r}\right)}{c\tau_u} \tag{83}$$

with κ_1^2 and κ_2^2 are expressed as $\kappa_n^2 = \frac{3}{7} + (-1)^n \frac{2}{7}\sqrt{\frac{6}{5}}$. According to *Bourdon et al.* [2007], the terms $\frac{n_u(\vec{r})}{c\tau_u}$ on the right-hand side of the equations (82)-(83) is written as:

$$\frac{n_u(\vec{r})}{c\tau_u} = \frac{p_q}{p + p_q}\left(\frac{\nu_u}{\nu_i}\right)\nu_i n_e \tag{84}$$

where p_q is the quenching pressure assumed to be equal to 30 Torr [*Bourdon et al.*, 2007], and p is the local air pressure. ν_i corresponds to the excitation frequency, and ν_u denotes the electron impact excitation frequency for level u. In this work, the term $\xi\frac{\nu_u}{\nu_i}$

is assumed to be equal to 0.06 [*Bourdon et al.*, 2007]. Note that this value could also be varying as function of the reduced electric field as pointed out in *Liu and Pasko* [2004].

The resolution of the equations (82)-(83) is similar to the resolution of Poisson's equation (1). Indeed, the only difference in the three-group SP_3 equations with respect to the discretized Poisson's equation (see the equations (26) and (27)) is the presence of an absorption term on the left-hand side. We can solve this equation using the Poisson's solver with a slight modification to add this extra term. In order to mitigate the numerical noise introduced by the Poisson's solver when using large simulation domains implying very small values of the photoionization term ($\sim 10^{-12}\,\mathrm{cm}^{-3}\,\mathrm{s}^{-1}$) away from the streamer head, we add a residual photoelectron background of $1\,\mathrm{cm}^{-3}$, which otherwise has a negligible impact on the simulation results.

The boundary condition used in this manuscript consists in nullifying the three terms of S_{ph} at the borders of the domain. More details about relevant boundary conditions in *Bourdon et al.* [2007]; *Liu et al.* [2007].

II.5 Chemical model

The chemical model accounts for the production or loss of electrons and ions due to various electric-field-dependant reactions. Our chemical model includes common chemical reactions implemented in streamer models:

$$\mathrm{e} + \mathrm{O_2} \longrightarrow 2\,\mathrm{e} + {\mathrm{O_2}}^{+} \tag{85}$$

$$\mathrm{e} + \mathrm{N_2} \longrightarrow 2\,\mathrm{e} + {\mathrm{N_2}}^{+} \tag{86}$$

$$\mathrm{e} + \mathrm{O_2} \longrightarrow \mathrm{O} + \mathrm{O}^{-} \tag{87}$$

$$\mathrm{e} + \mathrm{O_2} + \mathrm{A} \longrightarrow {\mathrm{O_2}}^{-} + \mathrm{A} \tag{88}$$

The equations (85) and (86) describe the ionization for O_2 and N_2. The equations (87)-(88) account for the two-body dissociative and three-body attachment processes. These

chemical reactions are taken into account through the terms referred to as ν in the right-hand side of equations (2)-(4). We use the source term frequencies provided by *Moss et al.* [2006].

In addition, we take the term of electron positive ion recombination β_{ep} expressed in $\mathrm{cm}^{-3}\,\mathrm{s}^{-1}$ (equations (2)-(4)) into account and defined as:

$$\beta_{ep} = 1.138\mathrm{x}10^{-11}\frac{q_e D_e}{\mu_e k_b}^{-0.7} \tag{89}$$

The negative-positive ion recombination β_{np} (in $/\mathrm{c}^3\mathrm{m/s}$) is written as:

$$\beta_{np} = 2\mathrm{x}10^{-13}\sqrt{\frac{T}{300}} \tag{90}$$

where T is the neutral temperature of the medium assumed to be 300 K at ground pressure.

II.6 Spectroscopy

The spectroscopy model consists in computing the density of specific electronic states of excited species of N_2 and $N_2{}^+$ through solving the equation (91):

$$\frac{\partial n_k}{\partial t} = -\frac{n_k}{\tau_k} + \nu_k n_e + \sum_m A_m n_m \tag{91}$$

where n_k is the density of excited species, ν_k is the excitation frequency of the species k. The last term describes the quantum cascade. The lifetime is defined as:

$$\tau_k = \frac{1}{A_k + \alpha_{1,k} N_{\mathrm{N}_2} + \alpha_{2,k} N_{\mathrm{O}_2}} \tag{92}$$

where A_k is the Einstein coefficient, $\alpha_{1,k}$, $\alpha_{2,k}$ the collisional quenching rates, and N_{N_2} and N_{O_2} the partial densities of N_2 and O_2, respectively. Equation (91) is solved using

a forward Euler method.

Simulations conduct at high altitude ($\geq 80\,\mathrm{km}$ altitude) are time-consuming because the time step of the simulations are dictated by the spectroscopic time scale rather than the electrodynamics. To achieve simulations at such altitudes within a reasonnable time, we split the spectroscopy computation from the time grid used for the rest of the physics. In practice, we compute the time scale as described in the section II.1 ignoring the spectroscopic contribution. Then, we compute the quantities we need to solve equation (91). Solving of the equation (91) is done using a time step obtained from the time scale from the equation (19) up to the time scale obtained from electrodynamics of the streamer given by equation (20) considering the equations (15)-(18). We iterate until the spectroscopic time equals the electrodynamics one.

In our model, we consider four band systems that are usally bright enough to detect TLEs:

Lyman–Birge–Hopfield (LBH) bands from $\sim$100 nm to $\sim$260 nm produced by the transition $N_2(a^1\Pi_g \rightarrow X^1\Sigma_u^+)$ [e.g., *Liu and Pasko*, 2005; *Liu et al.*, 2006b, 2009a; *Gordillo-Vázquez et al.*, 2011]

The first positive band system ($1PN_2$) from $\sim$650 nm to $\sim$1070 nm produced by the transition $N_2(B^3\Pi_g \rightarrow A^3\Sigma_u^+)$ [e.g., *Mende et al.*, 1995; *Hampton et al.*, 1996; *Green et al.*, 1996; *Morrill et al.*, 1998; *Milikh et al.*, 1998; *Bucsela et al.*, 2003; *Kanmae et al.*, 2007, 2010; *Siefring et al.*, 2010; *Gordillo-Vazquez*, 2010; *Gordillo-Vázquez et al.*, 2011, 2012]

The second positive band system ($2PN_2$) from $\sim$330 nm to $\sim$450 nm produced by the transition $N_2(C^3\Pi_u \rightarrow B^3\Pi_g)$ [e.g., *Armstrong et al.*, 1998; *Morrill et al.*, 1998; *Milikh et al.*, 1998; *Suszcynsky et al.*, 1998; *Heavner et al.*, 2010; *Gordillo-Vazquez*, 2010; *Gordillo-Vázquez et al.*, 2011, 2012]

The first negative band system of the positive ion N_2^+ ($1NN_2^+$) from $\sim$390 nm

to ∼430 nm produced by $N_2^+\left(B^2\Sigma_u^+ \rightarrow X^2\Sigma_g^+\right)$ [e.g., *Armstrong et al.*, 1998; *Suszcynsky et al.*, 1998; *Kanmae et al.*, 2010]

Note that the quantum cascade from $N_2(C^3\Pi_u)$ to $N_2(B^3\Pi_g)$ populates $N_2(B^3\Pi_g)$ and hence has an effect on the $1PN_2$ emission. The figure 14 shows the energy levels of the most intense vibronic transitions of these band systems.

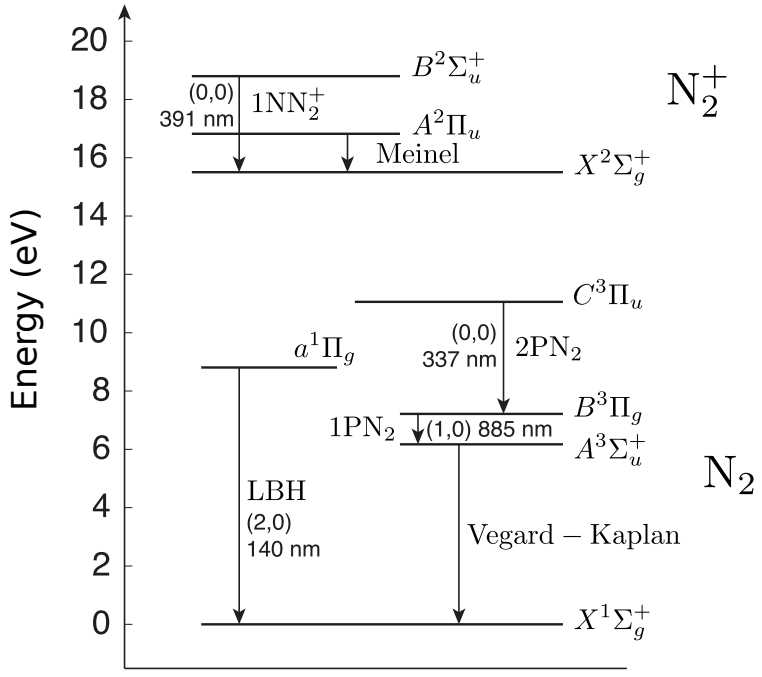

Figure 14: Molecular electronic states and band systems that can be found in sprites. Vibronic transitions are indicated by parenthesis and correspond to the brighest emission of each band system [*Gordillo-Vázquez et al.*, 2011]. Adapted from [*Ihaddadene*, 2016].

Einstein coefficients and quenching factors for these band systems are summarized in the Table 4.

Optical emissions are calculated using [e.g., *Liu and Pasko*, 2004]:

$$I = 10^{-6} \int_{\mathscr{L}} A_k n_k \mathrm{d}l \tag{93}$$

where I is the flux of photons in rayleighs noted R (expressed in the SI as $\mathrm{m^{-2}\,s^{-1}\,sr^{-1}}$),

Variables	LBH	$1PN_2$	$2PN_2$	$1NN_2$
A_k (s^{-1})	1.8×10^4	1.7×10^5	2×10^7	1.4×10^7
α_1 (cm^3/s)	1×10^{-11}	1×10^{-11}	1×10^{-11}	4.53×10^{-10}
α_2 (cm^3/s)	1×10^{-10}	3×10^{-10}	3×10^{-10}	7.36×10^{-10}
h_Q (km)	77	67	31	48

Table 4: Einstein coefficients A_k, quenching factors $\alpha_{1,2}$, and quenching altitude h_Q for the four band systems used in our model. Reproduced from [*Ihaddadene and Celestin*, 2017].

and $\mathscr{L}$ is the line of sight over which the integral is performed. Considering a line of sight perpendicular to the axis of the streamer discharge as illustrated in the figure 15, the term l can be expressed in the Cartesian coordinate system as $l = \sqrt{r^2 - y^2}$ using Pythagoras' theorem. Substituting the previous expression and plugging it into the equation (93), we obtain:

$$I = 10^{-6} \int_{r=y}^{r=r_{\mathtt{max}}} A_k n_k \frac{r}{\sqrt{r^2 - y^2}} \mathrm{d}r \tag{94}$$

where $r_{\mathtt{max}}$ is the simulation domain radius. One can see that (94) corresponds to an Abel transform [*Bonaventura et al.*, 2011].

II.7 Radio emission

In our model, we add the possibility to evaluate the electromagnetic radiation produced by sprite streamers. We assume that a sprite streamer can be assimilated to a straight antenna in which the current is flowing. This assumption allows the computation of the magnetic field radiated by the sprite streamer without the use of more complex models requiring to solve Maxwell's equations. The azimuthal component of the magnetic field radiated by a straight antenna B_ϕ is given by the Uman's model *Uman et al.* [1975]:

$$B_\phi(t) = \frac{\mu_0}{4\pi} \int_{H_1}^{H_2} \frac{\sin(\theta)}{R^2} i(z, t - \frac{R}{c}) \, \mathrm{d}z + \frac{\mu_0}{4\pi} \int_{H_1}^{H_2} \frac{\sin(\theta)}{cR} \frac{\partial i(z, t - \frac{R}{c})}{\partial t} \, \mathrm{d}z \tag{95}$$

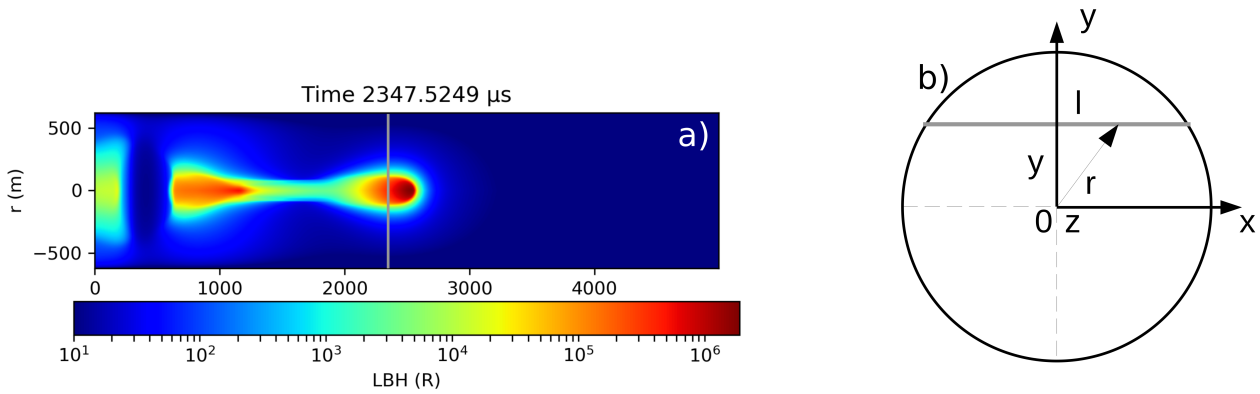

Figure 15: Illustration of the calculation of optical emissions through the equation (93). The cross-sectional view of the photon flux (a) for the LBH system for a single streamer propagating from 80 km to 75 km under a varying air density with an ambient electric field of 0.8 E_k (see [e.g *Qin and Pasko*, 2015]). The grey line corresponds to the line of sight for the computation of the photon flux. Panel (b) is a view in the direction of the vertical axis of the cylindrical simulation domain and the line of sight. Adapted from *Ihaddadene* [2016].

where μ_0 is the vacuum permeability, θ is the polar angle between the streamer axis and the receiver, $i\left(z, t - \frac{R}{c}\right)$ is the current along the z-axis at the retarded time $t - \frac{R}{c}$ where R is the streamer-receiver distance and c is the speed of light in vacuum. The integral is performed over the domain in which the streamer propagates so that H_1 and H_2 are the altitudes of the domain borders.

II.8 Improving of the computation

In our streamer model there are two major bottlenecks coming from the three-group SP_3 and the Poisson's solver. Reducing the time required to compute these two elements allows to simulate larger streamers (a dozen of centimeters at ground pressure, and dozen of kilometers at typical sprite altitude). There are different way to proceed, each of them having advantages and disadvantages. In this section, I will describe some techniques we use to speed up the code.

Data structures are very important to reduce the computational time because they

usually allow faster access for specific problems. In the case of our model, the main data structure used is the multidimensional array, which is efficient for us as we use a regular mesh.

Access to the memory of an array must be done in a contiguous and predictable way as much as possible. Indeed, reading or writing in a contiguous memory area allows processors to optimize memory access using CPU caches, which are small but very fast memory directly integrated to processors themselves. In languages using column-major ordering like Fortran or Matlab, the fastest access is done when accessing the first index of the array because of the contiguous aspect of the memory. In languages using row-major ordering like C or Python, the fastest access is realized on the last index of the array.

Single Instruction Multiple Data (SIMD) is a paradigm, which consists in repeating a single instruction (e.g., addition) over multiple data. This is very efficient for loop computing because they are usually well-suited for that. In addition, CPUs have specific hardware to perform such operations leading to improvement of the computation time and use of CPUs resources. Such approach is very efficient and allows compilers to produce better codes.

Parallelization is used in our code to split a huge loop in a bunch of smaller ones that are computed on several CPUs. This approach is very efficient to significantly reduce the computation time. This can be done either with a shared memory model (e.g., OpenMP) or a distributed memory model (e.g., MPI). Our code has been written for a shared memory model through OpenMP. It is interesting to use a shared memory model when processors are on the same motherboard, while distributed memory model is well-suited for clusters (i.e., processors are not all on the same motherboard). Of course, it is possible to mix the both approach to exploit their respective advantages. Such approach is named hydrid programming.

Parallelization can also be used to split tasks (i.e., different sets of operations) over several CPUs. For instance, the computation of fluxes and the FCT limiter to solve drift-diffusion equations (see Section II.3) is split in two tasks. The first task consists in computing the fluxes meanwhile the second task (running on a different CPU) computes the FCT limiter.

GPGPU consists in using GPUs to perform general computations. GPGPU is very efficient for computations that do not need to wait for intermediate results. The computation over GPUs is a bit more complex than for CPUs and requires a good understanding of some hardware features (e.g., PCI-Express communication, low-level memory access, GPU's architecture) to access high-performance. However, note that all algorithms are not suited for GPUs. In our implementation both, the Poisson's and SP_3 solver use the GPU.

Speculative execution covers a set of optimization techniques to speed-up code and avoid idle CPU time. It includes prefetching memory, value prediction, branch prediction, and others. Usually, this task is performed by processors. Branch prediction has a cost on modern processor and in the aim to reduce penalities, processors will try to predict the branch before its execution. If the value found by the branch predictor is correct, it results a positive impact (i.e., speed-up), otherwise the impact is negative because the processor has to turn back its execution implying flushing and reloading the instruction pipeline. To reduce the negative impact, the conditional branch must turn into a branchless form. Note that branchless forms can be prone to SIMD optimizations. In the case where the conversion is not feasible, branch conditions should be written in the order of decreasing likelihood. Rewriting the code to help the predict unit in the CPU is possible. However this technique is very specific to a given CPU microarchitecuture and requires a good description of such unit by the manufacturer, which is

not always available.

Denormal numbers corresponds to a non-zero number with a magnitude smaller than the small normal number i.e., its exponent is null and its mantissa different from zero. This hack allows to extend the representation of small values around zero. However, the downside of this approach is to significantly reduce the time of computation for a decimal operation (e.g., addition, multiplication) by a factor 10 to 100, especially when there is a mixing between normal and denormal values. This slackening happens because the CPU has to use specific microcode to handle such case. As these denormal values are very small with respect to normal values, we force them to be null in setting denormals-are-zero (DAZ) and flush-to-zero (FTZ) flags from the MXCSR register [*Intel Corporation*, 2016a,b].

In our model the compilater used is a build version of GCC 9.3 from scratch in order to have the graphite feature at our disposal. It consists in a framework for high-level memory optimizations (more details are available at `https://gcc.gnu.org/wiki/Graphite`).

The options used are *-O2 -march=znver1 -mtune=znver1 -frename-registers -ftree-vectorize -fno-prefetch-loop-arrays -ftree-lrs -fgraphite*. Note that *march* and *mtune* are specific to the processor used for our simulations. The option *O2* is a standard trade-off between time of compilation and optimizations done by the compiler. The two options *march* and *mtune* inform the compiler of the processor on which the code will be run, and thus it allows the compiler to use specific instructions, especially the instructions related to SIMD. The option *frename-registers* increases the pressure register (i.e., it allows the compiler to use as much as possible the whole of registers available in the processor). The option *ftree-vectorize* turns on the auto-vectorization of the code by the compiler to use SIMD. The option *fno-prefetch-loop-array* tells to the compiler to use prefetch instructions. Finally, the options *ftree-lrs* and *fgraphite* allow deeper optimization especially on

loops.

We use OpenMP for parallel computing mainly for the Poisson's solver and the three-group SP_3 model, both having a GPU agnostic-vendor implementation made with OpenCL providing an efficient solution for computation.

II.9 Validation of the model

II.9.1 Validation of the electrodynamic modeling part

The validation of the electrodynamic part is realized in running our streamer model in the same condition as *Bourdon et al.* [2007]. The domain size is of 151 x 1681 points with a mesh size of 8 µm. A neutral Gaussian shaped of plasma is placed in the middle of domain with a density of $10^{18}\,\mathrm{m}^{-3}$ under an electric field of $40\,\mathrm{kV\,cm}^{-1}$ at ground level. The figure 16 shows the electron density of the double-headed streamer at four different times. We compare the solution with the one found by *Bourdon et al.* [2007] as reported in the Figure 17. We see that the electric field of the double-headed streamer is synchronized both in space and time with the solution given in *Bourdon et al.* [2007]. In Figure 17, we identify two kinds of streamers. The first one is the negative streamer propagating from the middle of the domain to the right (0.7 cm to 1.2 cm). The second one is a positive streamer propagating from the middle of the domain to the left (0.7 cm to 0 cm). Both simulation results are in excellent agreement, especially given the non-linearity of the problem and the different approaches used.

We note that the negative streamer has a slightly higher electric field than the solution reported in *Bourdon et al.* [2007], especially at 1.5 ns, 2 ns, and 2.5 ns. This behavior is not visible for the positive streamer. Relative errors between the *Bourdon et al.* [2007] solution with our solution are reported in Figure 18. In this figure, we see that the upper limit of the error for the positive streamer is around 3.5 % and for the negative streamer is around 1.8 %, therefore such small relative errors illustrate an excellent agreement.

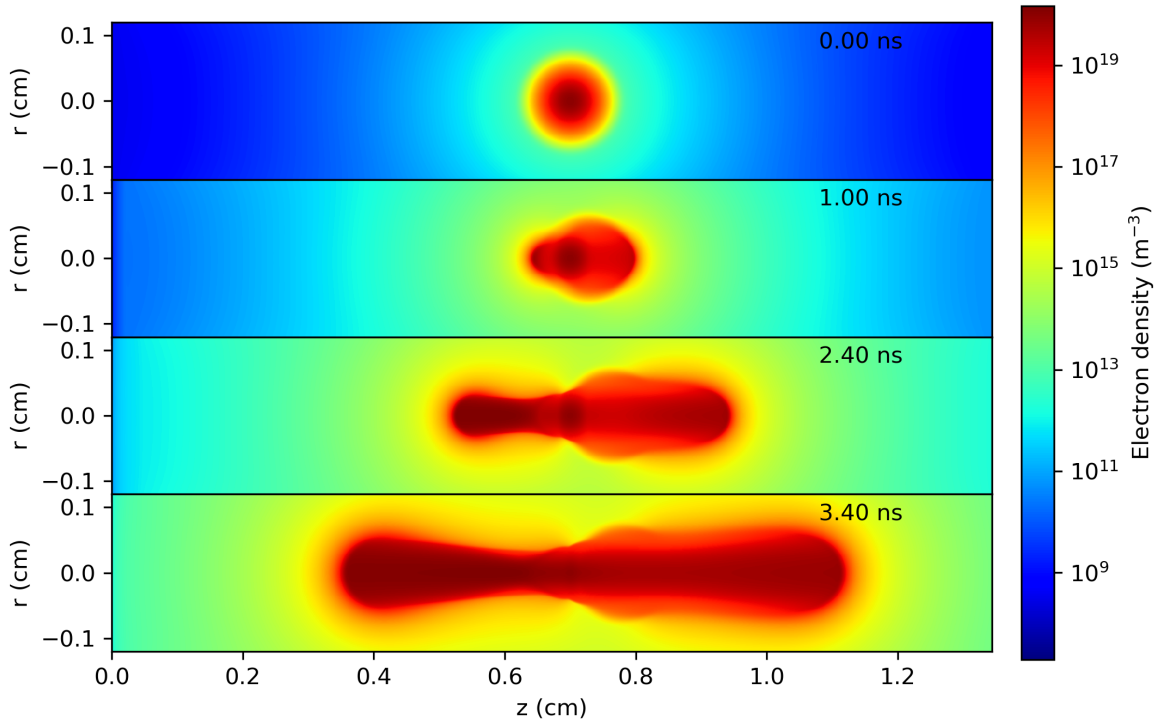

Figure 16: Snapshot of the 2-D cross sectional view of the electron density at four different time for a double-headed streamer propagating under an electric field of 40 kV cm^{-1} at ground level. The electron density is reported in the colorbar, and the time of each snapshot is written around the top-right corner of each subplot.

II.9.2 Validation of the spectroscopic modeling part

In the aim to verify the spectroscopic part of our model, a replication of the *Qin and Pasko* [2015]'s simulation is done. A domain size of 300 x 2400 points is used for a mesh size of 2.08 m with varying air density as function of the altitude. A positive streamer is initialized in placing a neutral Gaussian plasma at $z = 245$ m away from the left border with a peak density of 9×10^{18} m^{-3} at 80 km altitude, and propagates to 75 km altitude. An electron density background is used to reproduce the ambient ionospheric electron density [e.g., *Wait and Spies*, 1964]:

$$n_{e_{\text{amb}}}(h) = 1.43 \times 10^{13} \mathrm{e}^{-0.15h'} \mathrm{e}^{(\beta-0.15)(h-h')} \tag{96}$$

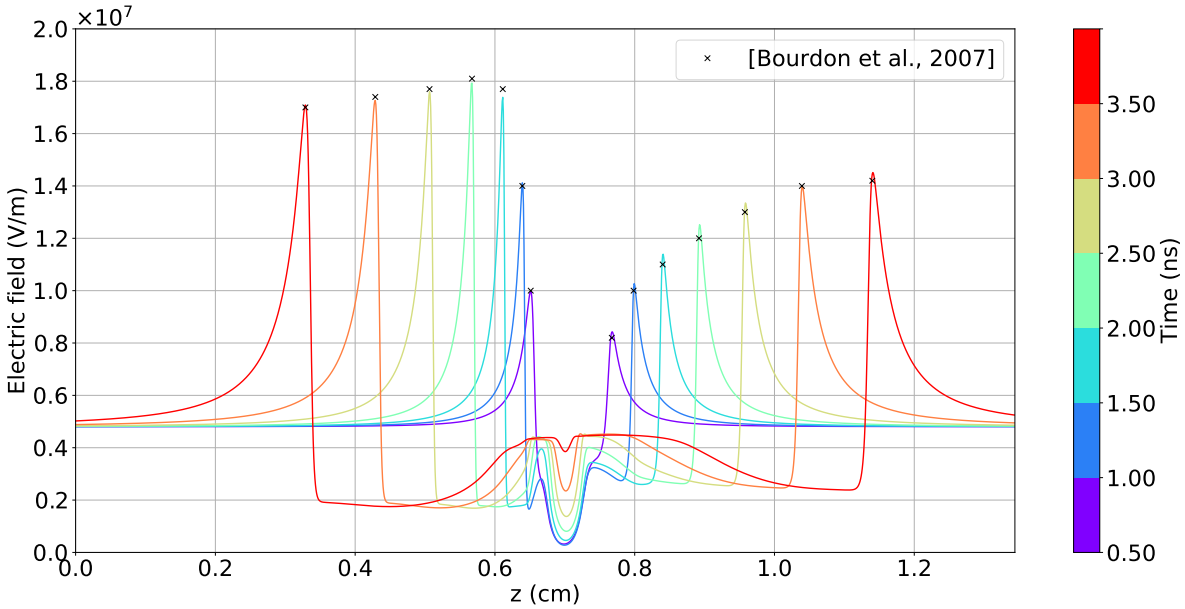

Figure 17: Comparison between the electric field produces by our streamer model and *Bourdon et al.* [2007]'s peak electric field indicated by black crosses. The time is reported by the colorbar.

where h is the altitude, h' is the reference altitude and β the sharpness. According to *Qin and Pasko* [2015], we set h' and β for a typical nighttime corresponding to $h' = 85\,\mathrm{km}$ and $\beta = 0.5\,\mathrm{km}^{-1}$ [e.g., *Han and Cummer*, 2010]. We observe that for a weak electric field, the presence of an electronic density background is necessary to initiate the streamer. The domain of simulation is immersed in a constant ambient homogeneous electric field of $0.8\ \frac{N}{N_0} E_k$ ($E_k = 30\,\mathrm{kV\,cm}^{-1}$). A snapshot of the propagation of this positive streamer is shown in Figure 19 at four different times.

The verification of the spectroscopic model used is done in comparing the output for each band system with the stationary solution (i.e., $\frac{\mathrm{d}n_k}{\mathrm{d}t} = 0$) of the equation (91) writing as:

$$n_k = \tau_k \left(\nu_k n_e + \sum_m A_m n_m \right) \tag{97}$$

The stationarity also referred as steady state occurs when the source terms (i.e, excitation

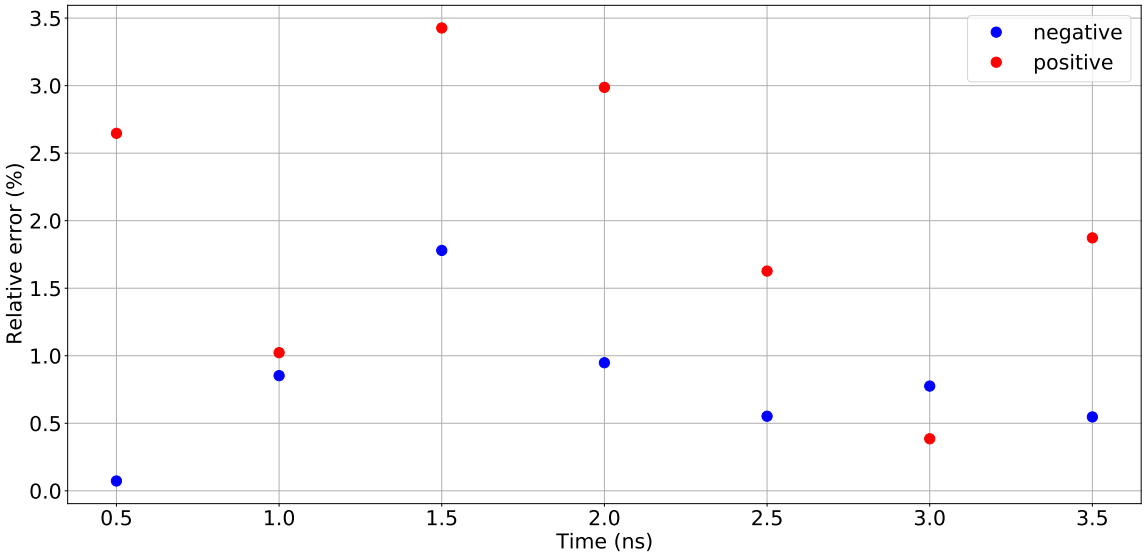

Figure 18: Comparison between the peak electric field along the z-axis obtained from our model and *Bourdon et al.* [2007] at different time of the simulation for a double-headed streamer. The red dots correspond to the negative streamer (the electric field from the middle of the domain to the right in the figure 17) and the blue dots correspond to the positive streamer (from the middle of the domain to the left in the figure 17).

due to electron impact) compensates for the loss terms (i.e., radiative deexcitation and collisonal quenching). The results is illustrated in Figure 20. We observe two behaviors: The first one is a perfect match for $N_2(C^3\Pi_u)$ and $N_2^+(B^2\Sigma_u^+)$ between their stationary solution (dashed orange line) and the solutions obtained with the simulation (blue line). The second behavior is a nearly perfect match for $N_2(a^1\Pi_g)$ and $N_2(B^3\Pi_g)$ except in the rear of the streamer head. We show significant difference for $N_2(a^1\Pi_g)$ of a factor 100 is between 77.5 km to 77.2 km altitude. Likewise, the $N_2(B^3\Pi_g)$ has a weaker difference (around a factor 10 is the worst case) at 77.3 km altitude. The difference observed in the behavior of $N_2(a^1\Pi_g)$, $N_2(B^3\Pi_g)$ and $N_2(C^3\Pi_u)$, $N_2^+(B^2\Sigma_u^+)$ is explained by the rate of gain or loss for each species through the terms $\nu_k n_e + \sum_m A_m n_m$ and $-\frac{n_k}{\tau_k}$ in the equation (91), respectively. In the figure 21, the density of excited species $N_2(a^1\Pi_g)$, $N_2(B^3\Pi_g)$, $N_2(C^3\Pi_u)$, and $N_2^+(B^2\Sigma_u^+)$ are shown in the vicinity of the streamer head, which is

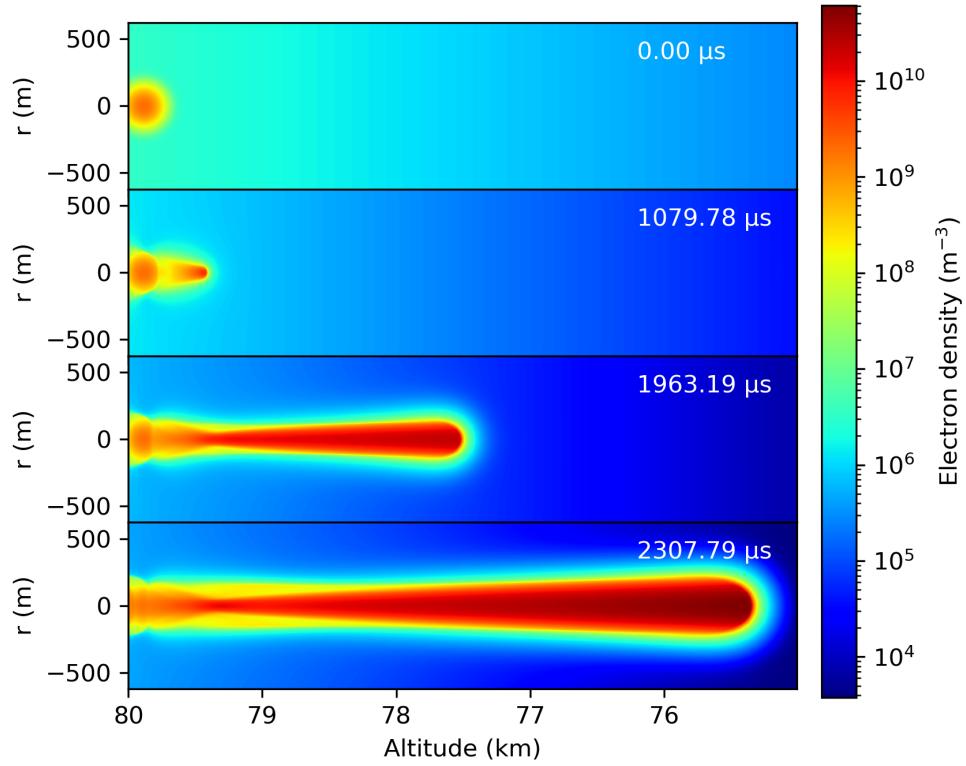

Figure 19: 2-D cross sectional views of the electron density at four different times for a positive streamer propagating under an electric field of 0.8 $\frac{N}{N_0}E_k$ from 80 km altitude to 75 km altitude. The electron density is reported in the colorbar, and the time of each snapshot is written around the top-right corner of each subplot.

localized by the maximum of the electric field. For the $N_2(a^1\Pi_g)$ and $N_2(B^3\Pi_g)$, near the streamer head, the presence of a high electric field (289 V m^{-1} or 118.6 $\frac{N}{N_0}$ kV cm^{-1}) leads to a high excitation frequency (1.77×10^6 s^{-1}) as shown in the figure 22. As the density of $N_2(a^1\Pi_g)$ is close to electron density and the lifetime frequency (dashed blue line in Figure 22) is lower than (7×10^4 s^{-1}), this results in an increase of the density of $N_2(a^1\Pi_g)$. Away from the streamer head the electric field is much weaker than near the streamer head (at 77.15 km altitude, it reaches 30 V m^{-1} or 12 6 $\frac{N}{N_0}$ kV cm^{-1}). Therefore the excitation frequency is also weaker (549 s^{-1}). Furthermore, the $N_2(a^1\Pi_g)$ lifetime is not driven by the electric field; the loss term (i.e., radiative deexcitation) thus dominates

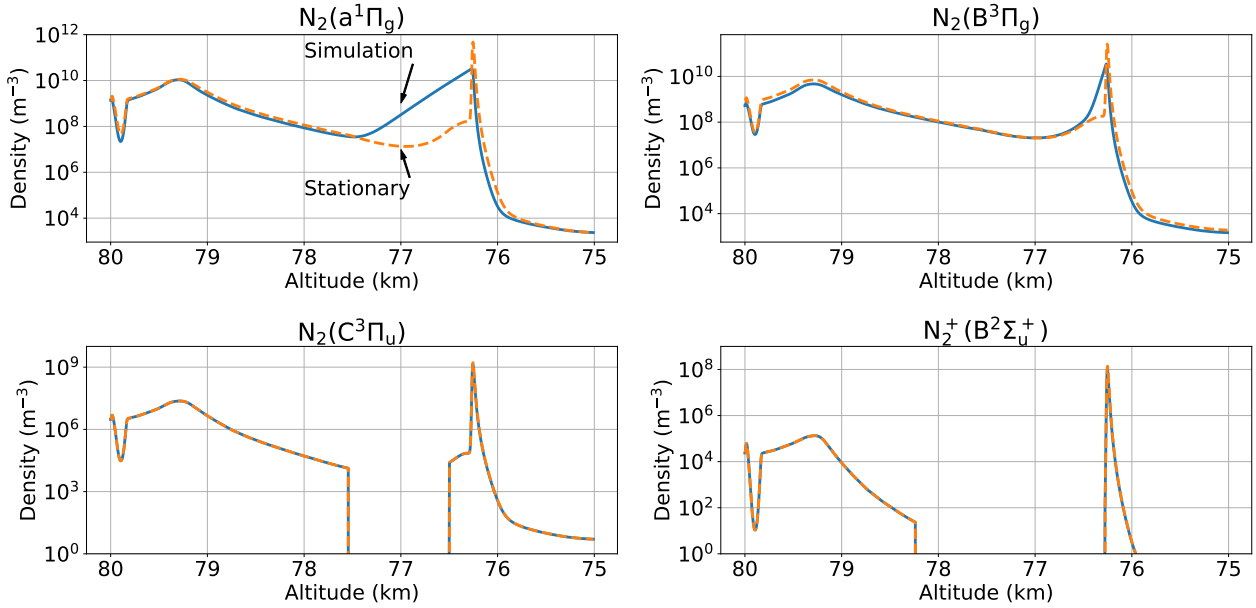

Figure 20: Validation of the spectroscopic modeling through the comparison of the density of excited species (blue line) and stationary solution (equation (97)) (dashed orange line) for the four electronic states used in our modeling and reported in the title of each plot. The electron density and electric field of the positive streamer used for the computation are shown in Figures 19 and 23, respectively.

the source term induced by the electron impact. This phenomenon is strong near the streamer head because the density of excited species is close to the electron density while in the same time the low electric field (a few meters behind the streamer head) makes the source term significantly weaker than the loss term. Nevertheless, the density of the excited species decreases as it gets farther away from the streamer head. At a one point, the density of the excited species equalizes the source term such that there is neither production nor loss of the density of the excited species along the time leading to the stationarity. The same thinking stays valid for the $N_2(B^3\Pi_g)$ except that the presence of the quantum cascade playing a role of production.

About the $N_2(C^3\Pi_u)$ and $N_2^+(B^2\Sigma_u^+)$, the same approach is also applied. However, two main differences need to take into consideration. Firstly, for both these species, their

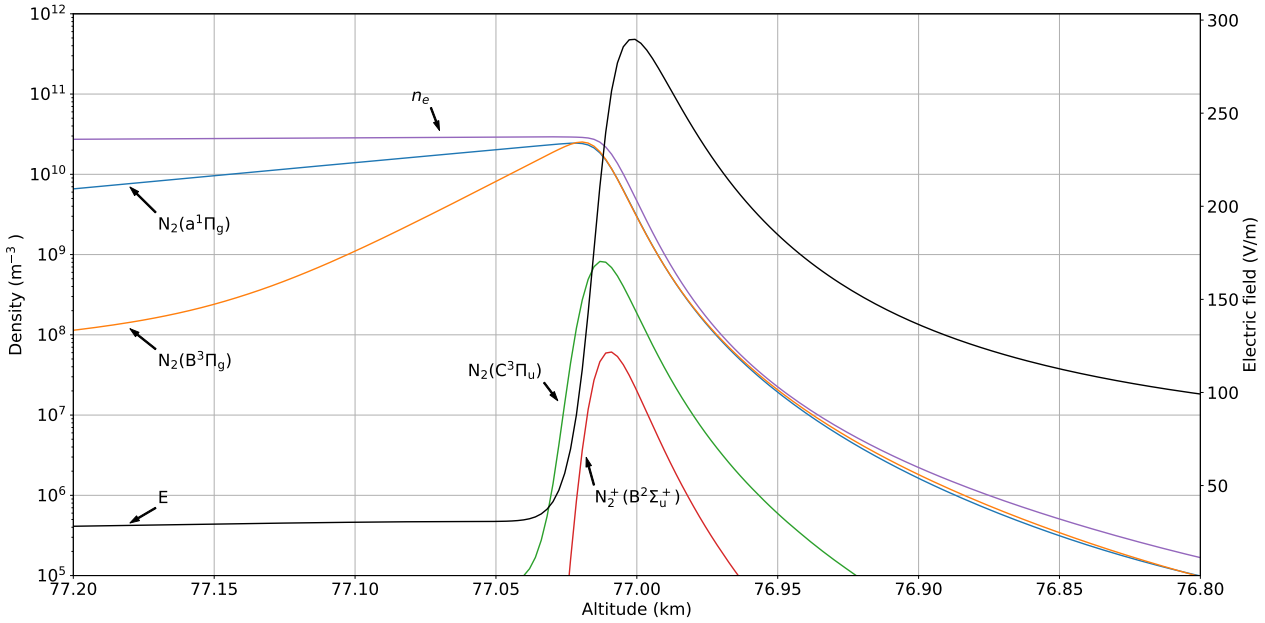

Figure 21: Distribution of densities of excited species $N_2(a^1\Pi_g)$ (blue), $N_2(B^3\Pi_g)$ (orange), $N_2(C^3\Pi_u)$ (green), and $N_2^+(B^2\Sigma_u^+)$ (red) as the function of the altitude in the vicinity of the streamer head defined by its electron density n_e (purple), and electric field E (black).

excited frequencies are always below the lifetime frequency as illustrated in Figure 22. Secondly, their densities are several orders of magnitude lower than the electron density by a factor of 30 and 292 for $N_2(C^3\Pi_u)$, and $N_2^+(B^2\Sigma_u^+)$, respectively. These species are thus in steady state, because their low densities and high lifetime frequencies are counterbalanced by the high electron density and their low excited frequencies.

In Figure 20, a sharp decrease is observable for $N_2(C^3\Pi_u)$ between 77.5 km and 76.5 km altitudes, and between 78.2 km and 76.3 km altitudes for $N_2^+(B^2\Sigma_u^+)$. These gaps result of a lack of excitation at these altitudes due to a weak electric field. In Figure 23, the electric field obtained along the z-axis for the positive streamer shown in Figure 19 is reported at three times. They illustrate the evolution of the electric field associated with the streamer at the beginning (958 µs), middle (1813 µs, and the end

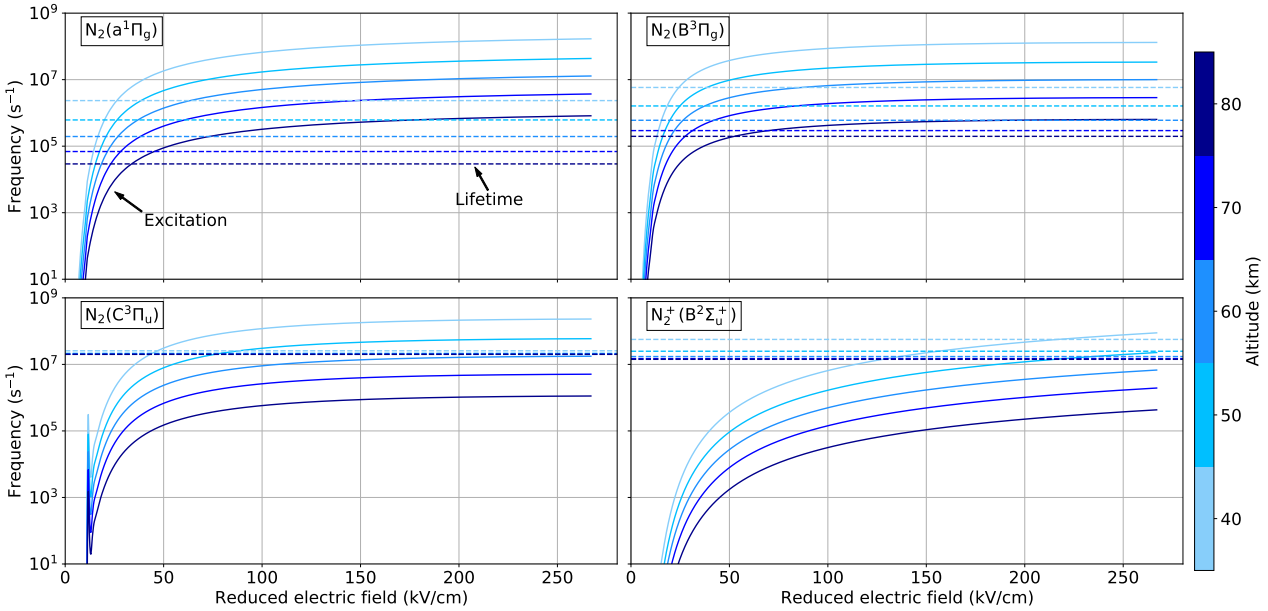

Figure 22: Excitation (solid lines) and lifetime frequencies (i.e. $\frac{1}{\tau}$) (dashed lines) as a function of the reduced electric field for $N_2(a^1\Pi_g)$, $N_2(B^3\Pi_g)$, $N_2(C^3\Pi_u)$ and, $N_2^+(B^2\Sigma_u^+)$ (indicated by the box at the top-left of each plot) at five altitudes reported in the colorbar.

(2267 µs). The cutoff for $N_2(C^3\Pi_u)$ and $N_2^+(B^2\Sigma_u^+)$ reported in this figure indicates the minimum electric field required to have a non-zero excitation frequency. We observe for three times reported that the electric field of the streamer channel (i.e., away from the streamer head) becomes lower than the two cutoffs for $N_2^+(B^2\Sigma_u^+)$ and $N_2^+(B^2\Sigma_u^+)$. For example, at 2267 µs the electric field of the streamer reaches 29.4 $V\,m^{-1}$ at 77.9 km altitude, which is a threshold for the $N_2(C^3\Pi_u)$. A little further on, its electric field reaches 26.4 $V\,m^{-1}$ at 77.1 $V\,m^{-1}$ corresponding to the threshold for $N_2^+(B^2\Sigma_u^+)$. As under these thresholds the electric field is not enough to excite N_2 molecules and $N_2{}^+$ ions, the source term in the equation (91) becomes null leading to the domination of the loss term (the quantum cascade exists only for the $N_2(B^3\Pi_g)$ populated through $N_2(C^3\Pi_u)$) and therefore the decrease of the density of excited species.

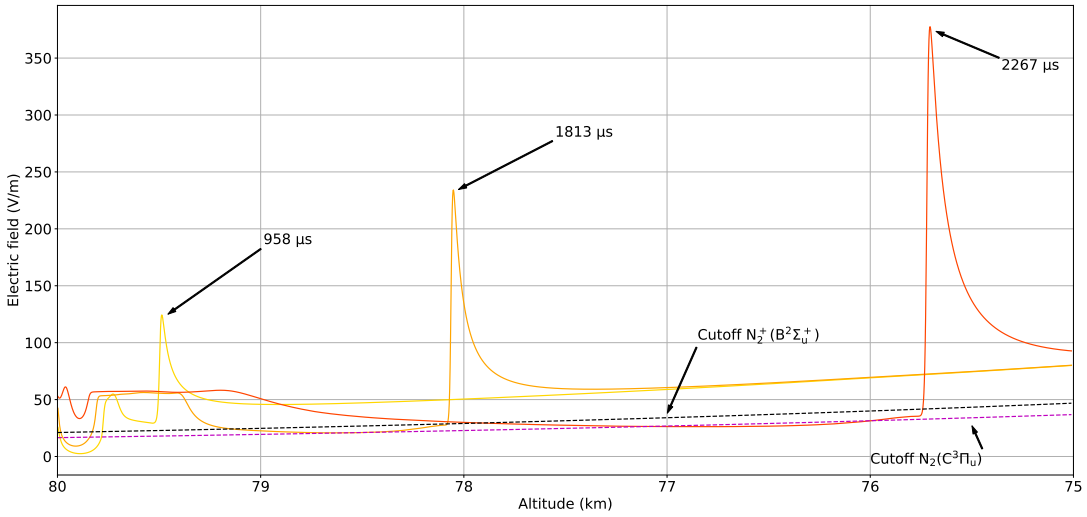

Figure 23: Electric field along the z-axis for the positive streamer shown in Figure 16 at 958 µs (yellow curve), 1813 µs (orange curve), and 2267 µs (red curve). The excitation cutoff for $N_2(C^3\Pi_u)$ (dashed magenta curve) and $N_2^+(B^2\Sigma_u^+)$ (dashed black curve) are expressed as a function of the electric field. They have been calculated using *Moss et al.* [2006].

II.9.3 Validation of the complete model

The validation of the complete model using both electrodynamic and spectroscopic part is realized in comparing the amount of light produced by the positive streamer reproduced in Figure 19 (see Section II.9.2) with the emission in the 1 PN_2 (i.e., $N_2(B^3\Pi_g \rightarrow A^3\Sigma_u^+)$) band system made by *Qin and Pasko* [2015]. The computation of the flux of photons is done through the equation (93) (see Section II.6). Figure 24 compares both results. We notice one little difference between both 1 PN_2 streamer emissions concerning the altitude of both streamers at the same time. Indeed, both streamers are not at the same altitude. While our streamer reached $\sim$ 76.3 km altitude, the Qin and Pasko's streamer reached an altitude of 77 km at 2201 µs. Firstly, this discrepancy can be explained through by two differences with respect to modeling: the streamer modeling reported by *Qin and Pasko* [2015] used an electrostatic field dynamically produced in ionosphere

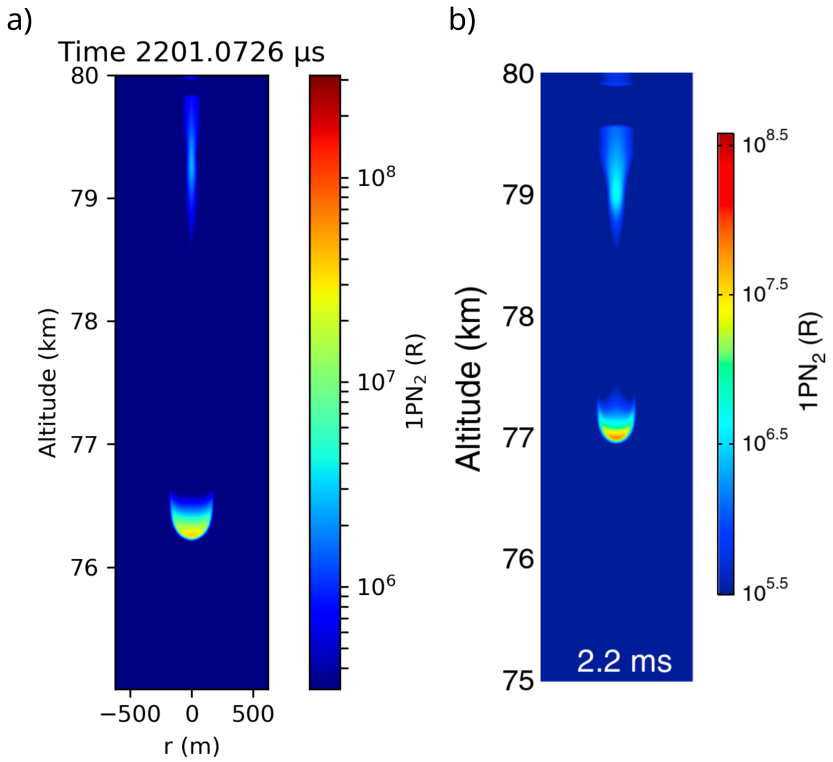

Figure 24: 2-D cross sectional view for the $1\,\mathrm{PN}_2$ optical emission from a positive streamer at 2.2 ms. a) Emission obtained from our model. b) Results adapted from [*Qin and Pasko*, 2015].

during a cloud-to-ground lightning discharge. Such dynamic structure of the ionosphere response is usually referred to as a halo. As the development of a halo model is beyond the focus of this thesis, we only compare our results with the order of magnitude of light emitted, which is used by photometers for spectroscopic diagnostics (.e.g, MCP on TARANIS). The second difference is explained by the setup of the initial conditions. Indeed, the exact location of the plasma cloud used to propagate the positive streamer was not clearly reported in *Qin and Pasko* [2015] leading to estimate its position from the 2-D cross sectional view of the electron density [*Qin and Pasko*, 2015, Figure 1]. However, we note that during our simulations the location of the initial plasma cloud has a strong impact on the propagation of the streamer including its altitude, speed,

and also electric field, thus introducing some variability in the simulation around $\sim 5\,\%$ to $20\,\%$ on the electric field and the altitude of the streamer for a variation of a dozen of meters of the initial position of the inital plasma cloud. About the flux of photons reported in Figure 24, there is only little difference between results both amount of photons flux in the streamer head. For both streamer, the photon flux is around $10^{7.5}\,\mathrm{R}$. The same approach was used at different times of Qin and Pasko's results, and we did not observe any significant discrepancies.

II.10 Conclusion

Through this chapter we describe how our streamer model has been built from scratch. As a streamer is a filament of plasma propagating under the action of an electric field, we have to take the space charge produced by local inhomogeneity into account through the Poisson's equation. As this equation establishes a link between the electric potential and the space charge, we can compute the electric field in deriving it.

The second part of the model consists to propagate the streamer due to electric field which will put in motions electrons and ions. Here, we use a mix between a first-order numerical scheme also referred as upwind, with a high-order scheme. However, such mixing produce numerical instabilities especially in presence of strong gradients. To ripple these effects and ensure a stable simulation over long time scale ($> 2\,\mathrm{ms}$ at $80\,\mathrm{km}$ altitude), and large scale ($> 10\,\mathrm{km}$ at $80\,\mathrm{km}$) we use the Flux-Correct Transport technique which introduces a mathematical flux limiter in combining low-order and high-order scheme to damp oscillations.

The third part models the photoionization process created by electron impact on N_2 molecules. These impacts excite N_2 molecules which deexcite in releasing UV photons, which in turn ionize the O_2 molecules. As this process requires a significant kinetic energy for electrons, it only happens in the streamer head, a piece of streamer where the electric field is significantly higher. Photoionization plays a role in the streamer

propagation in allowing the creation of a cloud of plasma in the vicinity of the streamer head. The model of photoionization retained for this work is the three-group SP_3 model because it consists to solve a set of Poisson's-like equations instead of compute a volume integral allowing a faster computation.

The last part of the model describes the interaction between electrons and, N_2 and O_2 molecules of the medium in which the streamer is propagating. The production of electrons and ions through ionization occurs in presence of sufficiently high electric field. The opposite process is named attachment which happens when the electric field is weaker, which conducts to a loss of electrons and ions. In complement, we add a spectroscopic model consisting in estimating the density of N_2 for the excited states $N_2(a^1\Pi_g)$, $N_2(B^3\Pi_g)$, $N_2(C^3\Pi_u)$, and $N_2^+(B^2\Sigma_u^+)$. We also describe how these densities are used in order to calculate the flux of photons produced by streamer during its propagation. In addition, we also add the *Uman et al.* [1975] antenna model to evaluate the electromagnetic field radiated by streamers, in assimilating them as straight antennas.

One of a goal of this thesis concerned in the development of a fast streamer model. We describes in this chapter several ways we used to speed-up, especially for the two bottlenecks that are the Poisson's equation and the three-group SP_3 model. These techniques consist to use OpenMP, a shared memory model API, to split huge loops into smaller ones that are running on cores of the processor. We also give details about the way to properly manage array structure (i.e., vectors and matrix) to take care of vectorization capabilities of modern CPU architecture. We also mention some advice concerning the speculative execution occurring within the chip itself and, sometimes can be useful to avoid penalties. Finally, we point out the bad effects of subnormal values during floating-point computation and how to ripple them.

Finally, the validation of the model has been done in three steps: Firstly, we have verified the electrodynamic behavior of the streamer in reproducing a streamer simulation described in *Bourdon et al.* [2007]. Then, we validated the spectroscopic model in com-

paring simulation results with steady state solution for $N_2(a^1\Pi_g)$, $N_2(B^3\Pi_g)$, $N_2(C^3\Pi_u)$, and $N_2^+(B^2\Sigma_u^+)$. Finally, the final test combined the electrodynamic and spectroscopic model to compare light emission of the $1\,PN_2$ released by a streamer with results found in the literature [*Qin and Pasko*, 2015].

As the final word, our model has been tested against results published in the literature and, we never observe any significant discrepancies between both results.

III Radio emission from head-on collision

III.1 Introduction

Cummer et al. [1998] observed electromagnetic emission in the extremely low frequency (ELF) to ultra low frequency (ULF) range due to electric currents flowing in the body of sprites. They evaluated that the electromagnetic energy in the ELF range is comparable to that of the parent cloud-to-ground (CG) lightning discharge. *Füllekrug et al.* [2001] confirmed these observations with radio and optical records of sprites with long-time delays relative to their parent lightning discharges. *Füllekrug et al.* [2010] recorded emissions in the low frequency (LF) range, which are temporally coincident with the sprite light emission. They showed that the electromagnetic pulse is produced by the sprite itself. *Farges and Blanc* [2011] reported electromagnetic radiation in the medium frequency (MF) range during sprite events. *Qin et al.* [2012] demonstrated the importance of the local air density on the frequency emission for a single-headed streamer and proposed that LF emissions are associated with streamer expansion processes.

In a different context, *Ihaddadene and Celestin* [2015] showed that collisions between streamers discharges at ground-level with opposite polarities would lead to strong electric field variations over a duration on the order of a dozen of picoseconds under high electric fields. This was latter confirmed through the use of different models [*Köhn et al.*, 2017; *Babich and Bochkov*, 2017; *Luque*, 2017; *Shi et al.*, 2019]. *Luque* [2017] and *Shi et al.* [2019] reported that such streamer collisions at ground-level should produce electromagnetic emission in the ultra high frequency (UHF-300 MHz-3 GHz) range. Using similarity laws [e.g., *Pasko et al.*, 1998; *Pasko*, 2006b; *Qin and Pasko*, 2015] to scale this typical duration of ∼10 ps at an altitude of 60 km, one finds a typical time scale on the order of a few tens of nanoseconds suggesting that electromagnetic emission in the high frequency (HF) and very high frequency (VHF) bands (respectively 30 MHz to 300 MHz) might be produced. If sufficiently bright, these emissions would be observable

from space above a few megahertz because of ionosphere filtering. It is worth mentioning that collisions between streamers are common in sprites [e.g., *Gerken et al.*, 2000; *Cummer et al.*, 2006b].

The purpose of this chapter is to characterize the electromagnetic radiation expected to be produced by collisions of streamers with opposite polarities, and to study its detectability by TARANIS and ground-based instruments such as the radiotelescopes NenuFAR [*Zarka et al.*, 2012, 2015] and the future Square Kilometer Array (SKA) [*Combes*, 2015]. We also provide the temporal pattern associated with such events to help with the identification of physical processes in the data.

III.2 Methods

The streamer model used is described in the chapter II. The numerical grid has a size of 151 × 1681 for a resolution of 8 $\frac{N}{N_0}$ µm, where N is the local neutral density of air and N_0 is the air density at ground level. The simulation is conducted at an altitude of 70 km under a homogeneous electric field of 40 $\frac{N}{N_0}$ kV cm^{-1}. As the length of the grid along the z direction is small (< 200 m), we neglect the variation of the air density as function of the altitude. Two Gaussian shaped neutral plasma seeds with a characteristic radius $\sigma = 3$ m are placed at 75.6 m and 122.8 m away from the right border so that as to produce two double-headed streamers, such that at 99 m (i.e., in the middle of the simulation domain) a head-on collision occurs between a negative and a positive streamer as shown in Figure 25. The inital density distribution is written as:

$$n_{i,j} = A\left[\exp\left(\frac{r_i^2 + (z_j - z_0)^2}{\sigma^2}\right) + \exp\left(\frac{r_i^2 + (z_j - z_1)^2}{\sigma^2}\right)\right] \tag{98}$$

where A is a constant, z_0 and z_1 are the positions of the maximum density of the seeds. In this work, at 70 km altitude, $A = 4.6 \times 10^{11}$ m^{-3}, $z_0 = 75.6$ m, and $z_1 = 122.8$ m.

The radiated magnetic field produced by the streamers is evaluated through the

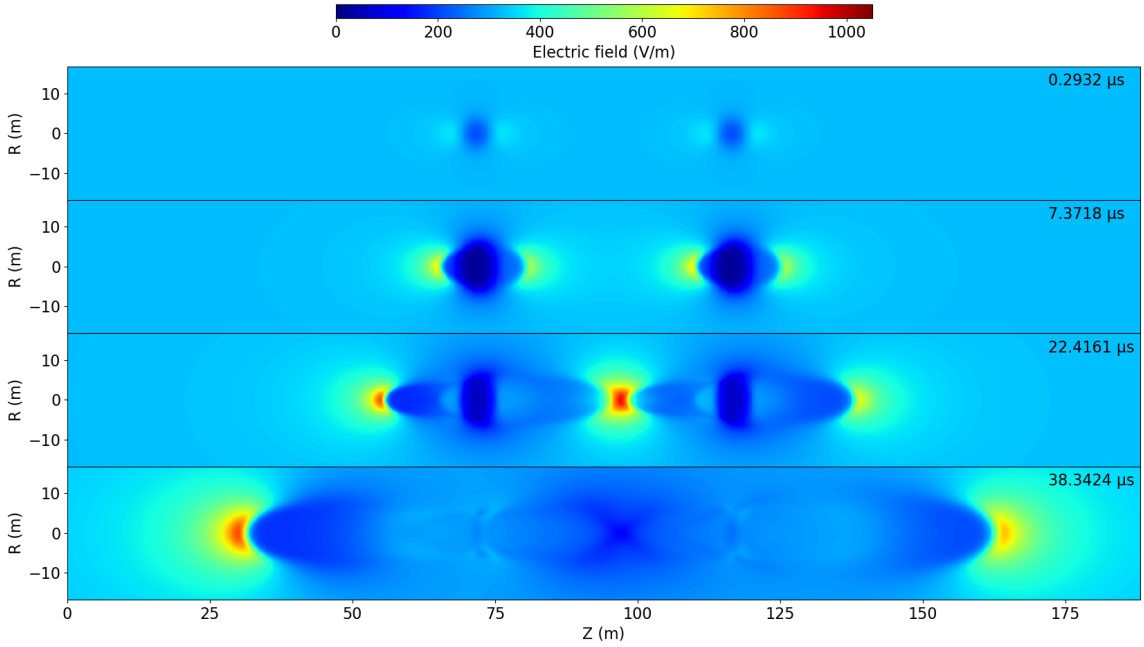

Figure 25: Four 2-D cross-sectional views of the absolute value of the axial component of the electric field for two double-headed streamers at an altitude of 70 km under a Laplacian electric field of 40 $\frac{N}{N_0}$ kV/cm. The time for each snapshot is given at the top right corner of the figure while the electric field is encoded with the top colorbar. The head-on collision between the two double-headed streamers occurs at 22.12 µs.

model of [*Uman et al.*, 1975] considering the cylindrical simulation domain as a straight antenna. The observational geometry is sketched in Figure 26.

The electric field radiated by the antenna is evaluated using the approximation $E = cB$ as the receiver is far away from the source. Indeed, a sprite streamer can be found between 40 km and 90 km altitude while the altitude of TARANIS will be ∼700 km. Furthermore, we neglect the first term in equation (95) considering that the receiver is away from the source. This assumption is verified if both terms in the equation (95) compare such that:

$$\frac{1}{R} i(z, t - \frac{R}{c}) \ll \frac{1}{c} \frac{\partial i(z, t - \frac{R}{c})}{\partial t} \tag{99}$$

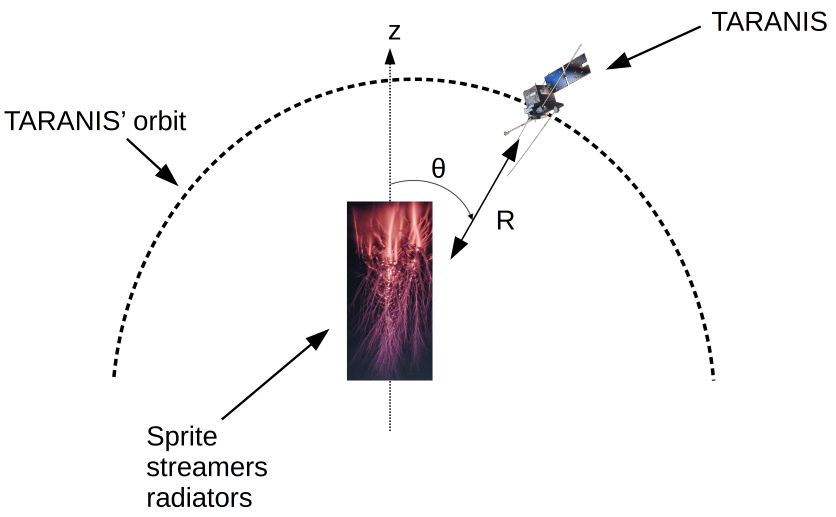

Figure 26: Observational geometry used in our model. Streamers are considered as straight antennas. The spacecraft is at a distance R from the streamers system, which is localized at a given altitude, and making an angle θ with respect to the spacecraft. Credits for the sprite picture: Stéphane *Vetter* [2019].

with straightforward manipulations, we obtain:

$$R \gg c \frac{i(z, t - \frac{R}{c})}{\frac{\partial i(z, t - \frac{R}{c})}{\partial t}} \tag{100}$$

and through a dimensional analysis, one has:

$$R \gg c\Delta t \tag{101}$$

The typical time for a double-headed streamer head-on collision at 70 km is around 20 µs, we hence get $c\Delta t \sim 6$ km, which is about 100 times lower than the streamer-receiver distance (∼600 km) considered in the study. The assumption neglecting first term of the equation (95) is deemed valid. Furthermore, the timestep varies dynamically to capture fast processes in the simulation. We resample the obtained radiated magnetic field at the lowest timestep used during the numerical simulation in a regular fashion through a

cubic interpolation. For a simulation at 70 km altitude, this lowest timestep is 2.5 ns.

Gerken et al. [2000] show that streamers can have transverse extents of about 150 m above 60 km altitude. Such streamers are therefore much wider than those usually obtained in simulations and presumably would carry much stronger electric currents. Indeed, the radius of the streamers shown in Figure 25 is ∼5 m. We hence consider a factor of ∼30 between such simulated sprite streamers and those in reality above 60 km. This difference in the streamer radius needs to be accompanied by an increase in the electric current proportional to the increase in the transverse area ($30^2 = 900$). As part of a preliminary work, through numerical simulations we have verified that such scaling is physical and that the corresponding streamers do follow the dynamics of smaller ones. However, those simulations are extremely resource- and time-consuming if to be pursued with a high grid resolution. In this work, we therefore choose to use this first order approximation factor of 30^2 to obtain the current carried by high-altitude sprite streamers. Note that the difference in size between real sprite streamers and simulated ones is also confirmed by *Liu et al.* [2009b] who found 4 orders of magnitudes between simulated and observed streamer brightnesses (brightness should be proportional to the streamer volume ($\sim 30^3$)) and *McHarg et al.* [2010] showed that a typical sprite streamer tip is 193 m, but found much greater radii for splitting streamers.

III.3 Results and discussion

Figure 25 shows a 2-D cross-sectional view of the electric field at the moment of the head-on collision between two double-headed streamers at 70 km. The collision occurs at $z \simeq 100$ m. The simulation domain is scaled at others altitudes using similarity laws [e.g., *Pasko et al.*, 1998; *Pasko*, 2006b; *Qin and Pasko*, 2015]. As part of preliminary work for the present study, we have verified the validity of this scaling-based method by realizing simulations at various altitudes.

Figure 27 shows the temporal evolution of the total current $i(z, t)$ (Equation (95))

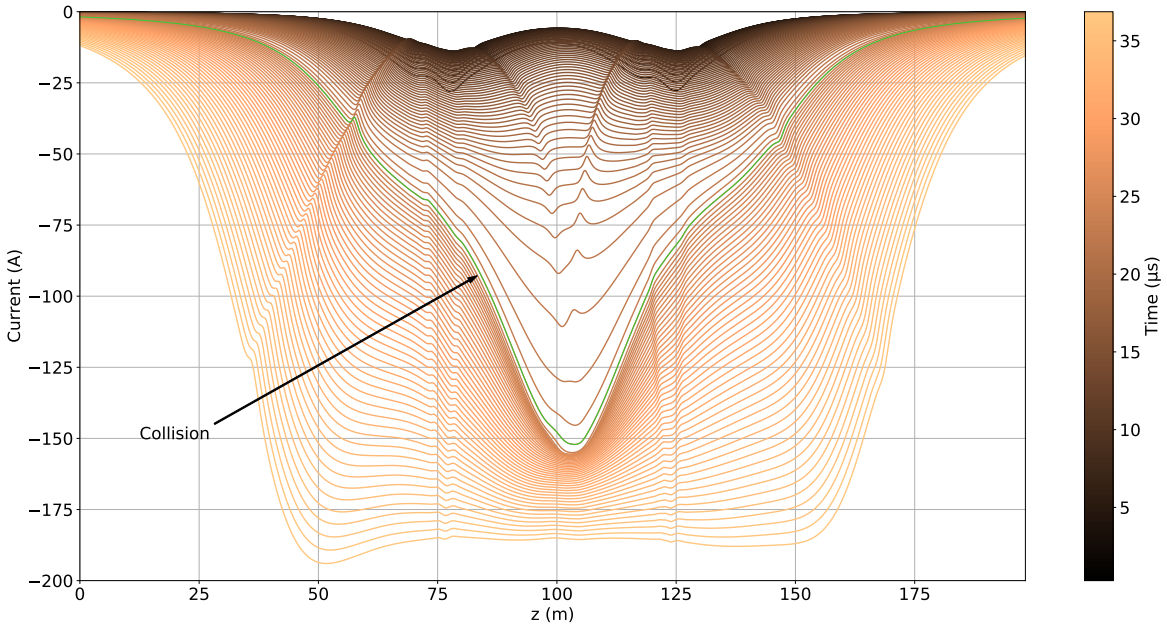

Figure 27: Total electric current along the axis of the domain as a function of position (lines are separated by a step of 0.29 µs) for the collision (green line) between two double-headed streamers illustrated in Figure 25. The time associated with the collision is defined as the time at which the electric field reaches its maximum.

before, during, and after the collision at 70 km altitude (Figure 25). It illustrates the increase of the current during the expansion of the two double-headed streamers before the collision (above the green curve), the strong variation of the current during the collision (green curve), and the increase of the current after the collision (below the green curve).

Figure 28 shows the magnetic field waveform radiated by streamers for collisions occurring at different altitudes as it would be observed by satellite when ignoring the dispersion of the signal through the ionosphere. This assumption allows to neglect qualitative effects such as Farady rotation, dispersion and others effects produced by local inhomogeneity of the ionospheric plasma (e.g., scintillation). We can separate each colored curve in three parts. The first part is before the collision. During that stage,

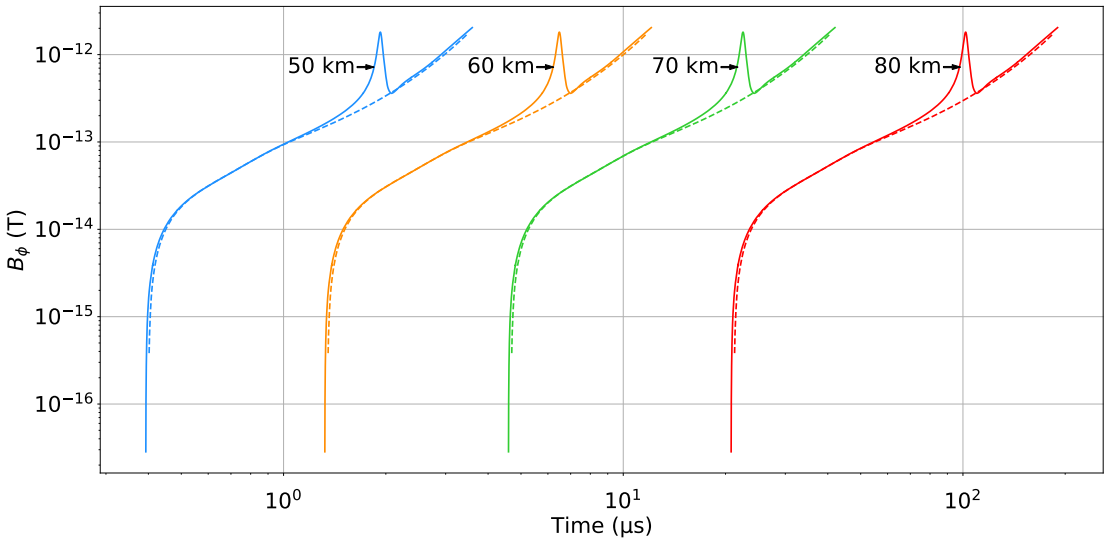

Figure 28: Magnetic field waveform radiated by two double-headed streamers evolving at an altitude of 50 km (blue), 60 km (orange), 70 km (green), and 80 km (red). The relative peak of each curve occurs when the head-on collision between two streamers occurs. Dashed lines are representative of a control simulation of two non-interacting streamers (see text). Results are obtained from a simulation at 70 km.

the increase of the magnetic field is due to an increase of the current in time resulting from the expansion of the two double-headed streamer, as first reported by *Qin et al.* [2012]. The second stage corresponds to the interaction between streamers. During the interaction, the electric field reaches up to 271 $\frac{N}{N_0}$ kV/cm leading to a strong increase in the electron density over a few nanoseconds, and then a strong variation of the current moment over a short time scale leading to a significant increase of the magnetic field illustrated by peaks in Figure 28. The increase of the electron density involves an increase of conductivity, which then leads to a sudden decrease of the electric field. Following the collision, we obtain a single double-headed streamer resulting from the merging of the two double-headed streamers. In the third stage, the total current is still increasing because of the expansion of the single double-headed streamer [*Qin et al.*, 2012], as during the first stage. This expansion is due to the presence of a homogeneous electric

field above the stability field for streamer propagation [e.g., *Liu et al.*, 2009b].

We conducted a simulation using the same setup with a single double-headed streamer in the aim to make a control experiment. Comparison with this no-collision case is shown in the Figure 28. In this figure the magnetic field in the control simulation (no-collision case) is multiplied by two to represent the magnetic field radiated by two non-interacting streamers. This comparison reveals that in the absence of a collision, the radiated magnetic field is around 1 pT at the position of the satellite, while in the case with collision we found 7 pT at 70 km altitude. The results for 50 km, 60 km, and 80 km are scaled using similarity laws. The streamer-observer distance stays at 600 km for all cases.

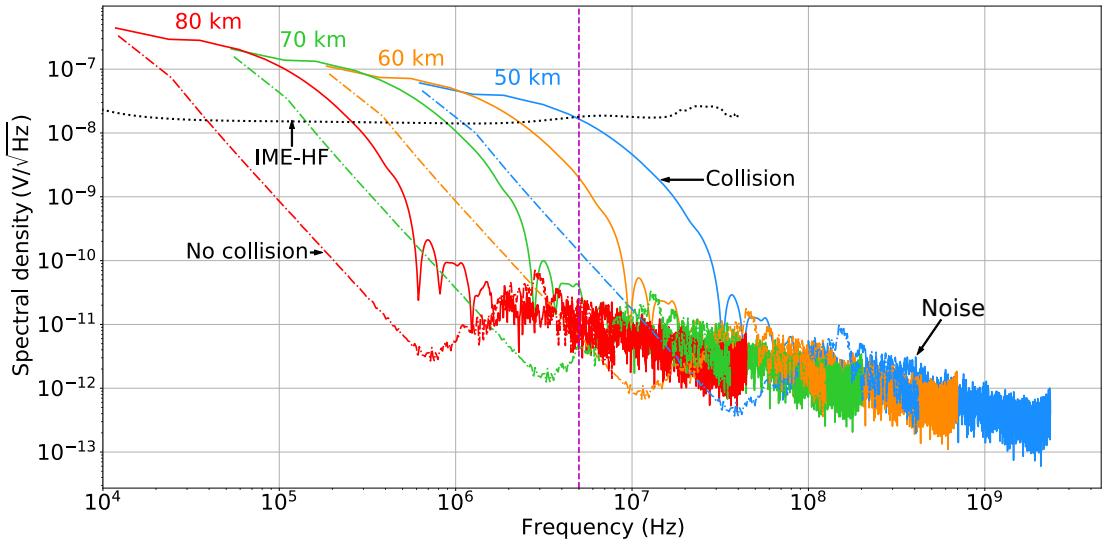

Figure 29: Spectral density of the electric field radiated by two double-headed streamers experiencing a collision (solid lines) and two, non-interacting streamers (dash-dotted lines) immersed in a homogeneous electric field of 40 $\frac{N}{N_0}$kV cm^{-1} at 50 km, 60 km, 70 km, and 80 km altitude. The dotted black line is for the sensitivity of the electric field instrument (IME-HF) on board TARANIS. The effective length of the electric antennas (1 m) has been applied. The sensitivity of the magnetic field instrument (IMM) is not shown because its sensitivity is too low (high sensitivity threshold). The dashed vertical magenta line corresponds to the typical ionospheric cutoff nighttime.

In Figure 29, we show the spectral density of electric fields radiated by two streamer

systems with and without collisions scaled at different altitudes.

For each spectral density shown in Figure 28, we observe three spectral regions for the case with collisions (plain curves). The first region corresponds to the linearly decreasing part of the spectral density and stops before the first significant decrease in the spectral density of the electric field in Figure 28. The frequency range for this region starts from ∼630 kHz up to ∼1.2 MHz for an altitude of 50 km. For an altitude of 60 km, the frequency range spreads from ∼180 kHz up to ∼1.2 MHz. At 70 km altitude, the first region is located between ∼53 kHz and ∼107 kHz, and for 80 km altitude it starts from ∼12 kHz to ∼23 kHz. Note that these low frequencies depend on the duration of the magnetic field signal therefore they do not have a straightforward physical significance because they are an effect of the simulation parameters. The second region starts from the previous point to the first first relative maximum. At 50 km altitude, this region reaches up to ∼30 MHz, for 60 km altitude it is 10 MHz, for 70 km altitude it is ∼3 MHz, and for 80 km altitude it is ∼700 kHz. The last region is filled with numerical noise. For the cases without collisions the three regions are turned into only two regions. The first region is defined by an exponential decrease of the spectral density followed by the second region, which is similar to the third region mentioned above. For 50 km altitude the exponential decrease starts at 648 kHz to 30 MHz, for 60 km altitude it is from 194 kHz to 9 MHz, for 70 kilometer altitude it begins at 55 kHz and it finishes at 2.6 MHz, and for 80 altitude it is between 12 kHz and 570 kHz. For all these altitudes, the spectral density decreases by about a factor of 75000. Note that the frequency associated with the first region is similar to the frequency for the case with collision.

To investigate the capability for TARANIS to detect these electromagnetic signatures, we compare our simulation results to the sensitivity threshold of the instruments IME-HF (dotted black line) in Figure 29. We compare it with the sensitivity of electric field instrument on board TARANIS. We assume an effective length of 1 m for the IME-HF electric antenna for the calculation of spectral density (J.-L. Rauch, IME-HF

Principal Investigator, Personal Communication, 2020). The sensitivity of IME-HF is slightly dependent on the frequency staying almost constant at $\sim 2 \times 10^{-8}\,\mathrm{V}/\sqrt{\mathrm{Hz}}$ from 50 kHz to 30 MHz, which is significantly below the signal level associated with streamer collisions occurring between 50 km and 80 km altitude. The sensitivity of the magnetic field instrument is not reported because its maximum of sensitivity (which is reached at 1 MHz) is 10 times above the maximum of the spectral density for a collision-case at 70 km altitude. The specific spectral signature depends on the altitude of streamers at the time of the collision (as time scales up with altitude, frequency scales down according to similarity laws [e.g., *Pasko*, 2006b]), thus creating a selective filter. Additionally, note that in this frequency range, the propagation through the ionosphere should reflect a significant part of the VLF-LF signal. We observe in Figure 29 that the sensitivity threshold for IME-HF allows to measure a significant part of the signal associated with a single collision. We hence conclude that for a single head-on collision of double-headed streamers, IMM could not detect the signal, while IME-HF might. Figure 29 shows that the neutral density dependence of streamer collision timescales would make altitude discrimination of events possible, and hence could play a complementary role in the exploitation of photometric measurements. However, note that the cases studied here are under the assumption that the effect of the ionosphere is negligible and that the noise context is favorable. If we consider that the nighttime cutoff frequency of the ionosphere is 5 MHz [*Davies*, 1989], HF signals coming from streamer collisions should be measurable by TARANIS when they occur above 50 km altitude. Note however that the ionosphere cutoff frequency depends on the state of the ionosphere, which can be strongly disturbed during thunderstorms, and ULF-LF radio emissions are known to be observable from space during thunderstorm activity [e.g., *Parrot et al.*, 2008]. Moreover, the sensitivity of IME-HF is evaluated from ground based measurements, therefore the true sensitivity in space will only be known once in flight.

However, as previously mentioned, sprites are composed of many streamers moving

up and down, and often interacting. It is expected that, TARANIS radio instruments will observe an incoherent signal resulting from the complex interactions of many sprite streamers. Furthermore, the radio emission produced by lightning discharges could contaminate data despite the fact that they are separated by a few ms. Extracting relevant information might require to use statistical or machine learning techniques. Based on recent reseearch, the observation of the electromagnetic energy released by sprites might help evaluate the number of streamers within sprites [*Liu et al.*, 2019], and the importance of their interactions.

We also evaluate the possibility to observe such events from ground-based telescopes. As an example, the radio telescope NenuFAR performs observations between 10 MHz and 85 MHz *Zarka et al.* [2012, 2015]. The main scientific objectives regarding NenuFAR are the detection and study of exoplanets in radio, detection of the radio signal of the "Cosmic Dawn" (epoch of formation of the first stars and galaxies), and the study of pulsars (hyperdense and strongly magnetized dead stars in rapid rotation). The typical distance between the radiotelescope and the sprite event is assumed to be similar to that of a satellite observation, such as sketched in Figure 26. In the field of radioastronomy, the Jansky unit ($1\,\mathrm{Jy} = 10^{-26}\,\mathrm{W\,m^{-2}\,Hz^{-1}}$), corresponding to the electromagnetic spectral flux density, is commonly used to compare the sensitivity of the instrument with sources. Equation (95) provides a magnetic field that we need to convert into spectral flux density. To obtain the spectral flux density, we compute the norm of the Poynting vector S, which is given by:

$$S = \frac{cB^2}{\mu_0} \tag{102}$$

The spectral distribution of S is obtained using the Fourier transform as shown in Figure 30. The spectral distribution of S is obtained using Fourier transform. Calculations show that the spectral density flux is produced by a sprite streamer collision in NenuFAR range is of $\sim$2 G Jy which is six orders of magnitude larger than the sensitivity of NenuFAR

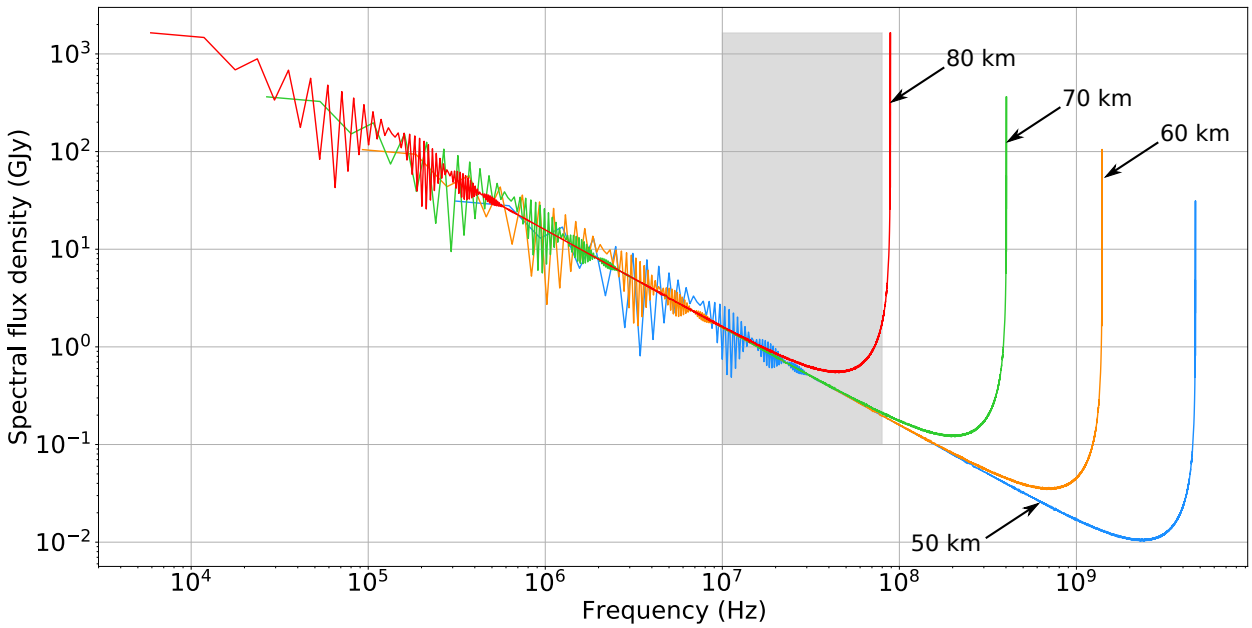

Figure 30: Spectral distribution of the Poyting vector calculated through equation (102). The altitude 50 km is symbolised by the blue line, 60 km by the orange one, 70 km by the green one, and 80 km by the red one. The grey rectangle corresponds to the frequency range used by the radiotelescope NenuFAR.

over a timescale of a dozen of microseconds (L. Bondonneau, Personal Communication, 2020) as shown in Figure 30, demonstrating the high potential of radiotelescopes in the study of TLEs.

III.4 Conclusion

In this chapter, we investigate the production of electromagnetic radio emissions associated with the interaction of plasma filaments in sprite discharges using a streamer fluid model. We show that the collision between two streamers produces a strong variation of the electric current over a short time scale. The short time scale is caused by the increase of the electron density leading to a high conductivity in the plasma, which then briefly collapses the electric field and produces a strong current variation over this short time

scale. We compare the resulting signal with the sensitivity of two radiowave instruments of TARANIS.

For a single collision, we find that the electric field exceeds IME-HF (electric antenna) sensitivity threshold. However, we conclude that IMM (magnetic antenna) sensitivity is too weak to detect such events. The challenge to analyze IME-HF data during thunderstorm where radio emission released by lightning discharges will also be mixing with the radio pattern associated with streamer collisions stays an open question. The results presented in this paper only concern a single head-on collision between two streamers with opposite polarities. This work has a strong implication for the scientific return of the TARANIS mission about the understanding of sprites.

A question remaining open concerns the impact of the ionosphere filtering on the propagation of the signal because in standard condition (i.e., without thunderstorms), the ionosphere tends to block all radio signal below or near its frequency cutoff, except for the Whistler mode of wave propagation. However, during a thunderstorm the ionosphere is strongly disturbed and some low-frequency emissions are known to become observable.

In addition to space observations, we find that ground-based instruments like NenuFAR should detect sprite filament collision events, and therefore open a new way to investigate the microphysics of sprites.

IV Spectrophotometric diagnostic

IV.1 Introduction

Sprites are composed of many plasma filaments named streamers. The observation of sprites can be done either from ground based instruments [e.g., *Gerken et al.*, 2000; *McHarg et al.*, 2010] or from instruments on-board spacecraft like ISUAL on-board FORMOSAT-2 [*Chern et al.*, 2003] or JEM-GLIMS aboard the Japanese module of ISS [*Ushio et al.*, 2011], and more recently ASIM [*Neubert et al.*, 2019] on the European module of ISS. We also mention the future TARANIS mission which is a spacecraft dedicated to the study of TLEs and TGFs [*Lefeuvre et al.*, 2008] and due to launch on November 2020. Except ISUAL, all these missions observe TLEs in nadir-viewing geometry from space. This configuration allows to measure the horizontal extent of sprites and the simultaneity of optical, radio, and particle emissions. Conversely, this configuration leads to the loss of the vertical resolution and thus of the altitude.

The aim to deduce the altitude of elements in the sprite event and the associated electric fields, we seek to interpret optical emissions through modeling. In this approach, there are four band systems that are usually used, three for N_2: the Lyman-Birge-Hopfield (LBH), the first positive ($1\,PN_2$), the second positive ($2\,PN_2$) band systems, and also the first negative band system ($1\,NN_2^+$) of N_2^+ (see Section II.6).

The use of irradiance ratio associated with different band systems to determine the electric field in sprite streamers has been largely reported in the literature [e.g., *Morrill et al.*, 2002; *Kuo et al.*, 2005; *Adachi et al.*, 2006; *Kanmae et al.*, 2010; *Adachi et al.*, 2016; *Ihaddadene and Celestin*, 2017; *Pérez-Invernón et al.*, 2018], as well as some degree of agreement with numerical simulations [e.g., *Liu et al.*, 2006a; *Adachi et al.*, 2008, 2016]. Nevertheless, theoretical and numerical studies have shown the need to use correction factors to correct the electric field associated with sprite streamers introduced by *Celestin and Pasko* [2010], these correction factors come from the spatial shift be-

tween the peak electric field localized in the streamer head and the peak in the excited species densities [*Naidis*, 2009] (see Figure 21 in Section II.9.2) as well as the streamer cylindrical symmetry [*Celestin and Pasko*, 2010]. *Bonaventura et al.* [2011] have shown how these correction factors could also be used in streamers at ground-level, for which the steady-state assumption of excited species is not valid.

Ihaddadene and Celestin [2017] have extended the ratio-band spectrophotometric method using the ratios $\frac{\mathrm{LBH}}{1\mathrm{PN}_2}$, $\frac{\mathrm{LBH}}{1\mathrm{NN}_2^+}$, $\frac{2\mathrm{PN}_2}{1\mathrm{NN}_2^+}$, $\frac{2\mathrm{PN}_2}{1\mathrm{PN}_2}$, and $\frac{2\mathrm{PN}_2}{1\mathrm{NN}_2^+}$, taking the non-steady state nature of some systems in sprites and the exponential expansion of streamers into account. They also tabulated correction factors to deduce accurate electric fields in streamer heads.

In this chapter, we succinctly describe the method developed by *Ihaddadene and Celestin* [2017]. We show how we can use it to obtain an estimation of both the altitude and the electric field. We also briefly investigate the possibility to use tabulated expansion rates to estimate ambient electric field [*Kosar et al.*, 2012]. This approach is verified with a control case in constant air density and varying air density in order to quantify their impact on the method. Then we apply the method to two sprite events observed by ISUAL and reported by *Kuo et al.* [2005].

IV.2 Method

The way to deduce the electric field and the altitude from spectrophotometric measurements is based on the ratio method proposed by *Ihaddadene and Celestin* [2017]. It consists in evaluate the ratio between the photon flux produced by two system bands of N_2 or N_2^+ emitted by sprite streamers. For a given band system , the photon flux can be evaluated through the equation (93) (see Section II.6). Assuming a uniform plasma with field E at altitude h, the ratio between irradiances of two band systems k and k'

can be expressed as:

$$\frac{I_k}{I_{k'}} = \frac{A_k \tau_k(h) \left(\nu_k(h,E) n_e + \sum_m A_m n_m\right)}{A_{k'} \tau_{k'}(h) \left(\nu_{k'}(h,E) n_e + \sum_{m'} A_{m'} n_{m'}\right)} \tag{103}$$

In the rest of this chapter for the sake of clarity, we will remove the dependencies in altitude and electric field. In practice, spectrophotometric measurements from space instruments realized by photometers correspond to the term k (or k') in the equation (103).

This equation implicitly assumes that excited species are in steady state. Nevertheless, *Celestin and Pasko* [2010] have mentioned that the steady state of excited species is not a necessary condition. *Ihaddadene and Celestin* [2017] showed that the main factor required to use such an approach in non-steady state, is to have a stable streamer propagation over a timescale on the order of the lifetime of excited species. It allows to rewrite the equation (91) as:

$$N_k = \tau_k \int_V \nu_k n_e \, \mathrm{d}V + \tau_k \sum_m N_m A_m \tag{104}$$

Where the term $\sum_m N_m A_m$ describes the radiative cascade from higher energy level m. The integral term can be written as in *Ihaddadene and Celestin* [2017]:

$$N^{\star}_{e,\nu_k} = \frac{1}{\nu_k} \int_V \nu_k n_e \, \mathrm{d}V \tag{105}$$

And thus, the equation (91) rewrites as:

$$\frac{\partial N_k}{\partial t} = -\frac{N_k}{\tau_k} + \nu_k N^{\star}_{e,\nu_k} + \sum_m A_m N_m \tag{106}$$

Considering that the expansion of a streamer follows an exponential process [*Liu et al.*,

2009a], the term N_k is expressed as:

$$N_k = N_{k,0} \exp(\nu_e t) \tag{107}$$

where ν_e is the expansion factor, which strongly depends of the ambient electric field [*Kosar et al.*, 2012].

In this case, considering only one upper level m for the radiative cascade, the equation (106) becomes:

$$N_k = \frac{\nu_k \tau_k}{1 + \nu_e \tau_k} \left(N^{\star}_{e,\nu_k} + \frac{1}{\nu_k} \frac{\nu_m A_m \tau_m N^{\star}_{e,\nu_m}}{1 + \nu_e \tau_m} \right) \tag{108}$$

If we assume the absence of radiative cascade between the band systems k and k', their ratio becomes:

$$\frac{I_k}{I_{k'}} = \frac{\nu_k \ A_k \ \tau_k \ N^{\star}_{e,\nu_k} (1 + \nu_e \tau_{k'})}{\nu_{k'} \ A_{k'} \ \tau_{k'} \ N^{\star}_{e,\nu_{k'}} (1 + \nu_e \tau_k)} \tag{109}$$

Assuming that the radiative cascade is reduced to $N_2(C^3\Pi_u) \rightarrow N_2(B^3\Pi_g)$, in the case of $N_2(B^3\Pi_g)$, the previous equation becomes:

$$\frac{I_k}{I_B} = \frac{\nu_k \ A_k \ \tau_k \left(\frac{1 \ + \ \nu_e \ \tau_B}{1 \ + \ \nu_e \ \tau_k} \right)}{\nu_B \ A_B \ \tau_B \left(\frac{N^{\star}_{e,\nu_B}}{N^{\star}_{e,\nu_k}} + \frac{\nu_C \ A_C \ \tau_C}{\nu_B \left(1 \ + \ \nu_e \tau_C \frac{N^{\star}_{e,\nu_C}}{N^{\star}_{e,\nu_k}} \right)} \right)} \tag{110}$$

For the sake of clarity, the subscript B corresponds to $N_2(B^3\Pi_g)$ and the subscript C corresponds to $N_2(C^3\Pi_u)$.

According to *Ihaddadene and Celestin* [2017] there is a need to correct the electric field to take non-homogeneity of the electric field and electron density into account. This correction can be done either with a correction factor as suggested by *Celestin and Pasko* [2010] or using the terms $N^{\star}_{e,\nu_k}$. If we consider the use of correction factors, it implies to set the terms $N^{\star}_{e,\nu_k}$ to 1, and otherwise the terms $N^{\star}_{e,\nu_k}$ have to be set according to tabulations made available by *Ihaddadene and Celestin* [2017]. In the rest of this

chapter, we always consider that field correction is done through the use of $N^{\star}_{e,\nu_k}$.

The expansion factor defined in *Ihaddadene and Celestin* [2017] corresponds to the photon flux growth rate of the streamers as defined in *Kosar et al.* [2012]. To obtain this value, we fit the distance travelled by the streamer in varying air density as function of the time, where the distance travelled by the streamer is defined as the distance between the center of the initial position of the seed (i.e., the neutral cloud of plasma used for the initialization of the streamer) and the position the peak electric field in the streamer head. An illustration is shown in Figure 31. The blue line represents the distance travelled by a positive streamer starting at 80 km altitude and propagating downward to 75 km altitude under a constant ambient reduced electric field of $1.2E_k$ as function of the time. The red curve corresponds to a linear fit (in a logarithmic space) over the propagation of the streamer (i.e., after its initialization stage). The slope deduced from the adjustment gives the expansion factor. However, this factor needs to be multiplied by 3 [*Kosar et al.*, 2012] to obtain the expansion associated with the photon flux of the streamer (i.e., the number of photons per unit time). Indeed, the photon flux depends on the volume, *Kosar et al.* [2012] showed that a factor 3 is required to obtain it from the growth rate of the distance traveled by the streamer.

The inversion of the problem consists in estimating the altitude and the electric field from the ratio of spectrophotometric measurements realized using tabulated ratios. The latter is made by evaluating spectrophotometric ratio values over a range of altitude and electric field through the equation (109) (or equation (110)) if the radiative cascade is used). As the computation of one ratio can be made independently, it is well suited for parallel computing (see Section II.8). Furthermore, we limit the altitude range between 40 km and 90 km altitude which corresponds to the typical altitude range of sprites [*Pasko et al.*, 1998]. Then, using this table, we can find the altitude and electric field corresponding to several spectrophotometric ratios in the parametric space. For two different ratios, we get two sets of possible altitudes and electric fields $\mathcal{S}_1$ and $\mathcal{S}_2$. The

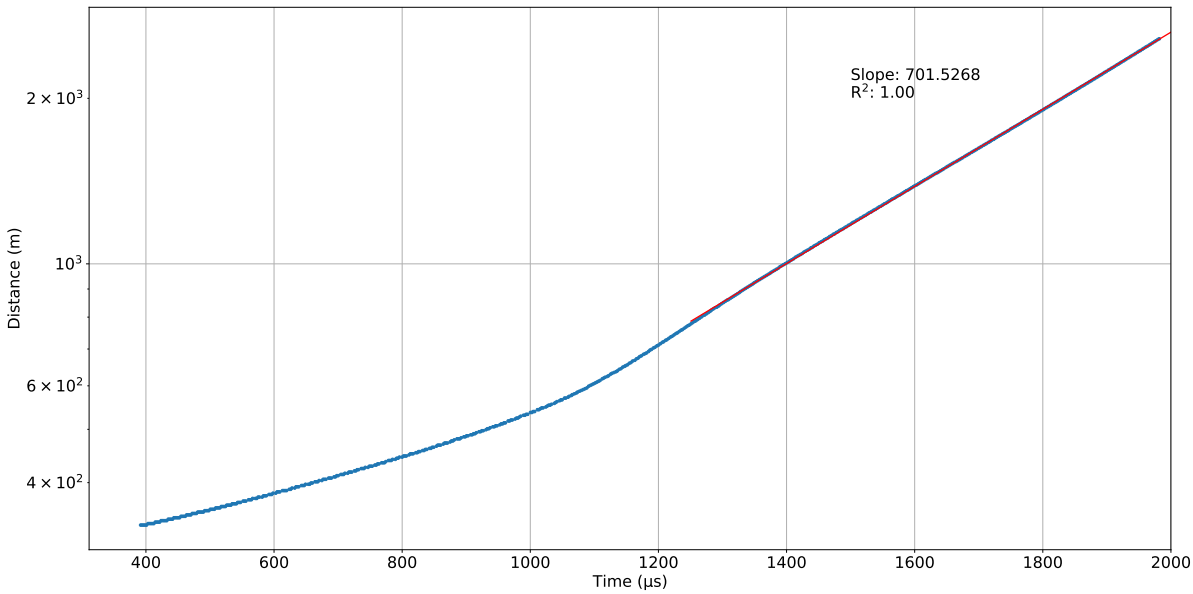

Figure 31: Distance travelled by a positive streamer as function of the time (blue line). The streamer starts at 80 km altitude and propagates downward up to 75 km altitude in varying air density under a constant laplacian reduced electric field of $1.2E_k$. The red line corresponds to a fit in logarithmic space of the part corresponding to the expansion of the streamer between 1200 µs and 2000 µs. Before that time, the streamer is starting its propagation from the seed. The value of this expansion as well as the coefficient of determination (R^2) is reported in the text box.

deduction of the altitude is realized through:

$$h = \mathcal{S}_1 \cap \mathcal{S}_2 \tag{111}$$

In our analysis, we use the ratio $\frac{\text{LBH}}{\text{1PN}_2}$ because the quenching altitude of the LBH (at 77 km altitude [*Ihaddadene and Celestin*, 2017]) allows to have an effect on the ratio as function of the altitude for high altitudes since the collisional quenching decreases the amount of photons released. Figure 32 represents one possible parameter space for this ratio where we observe that for a given altitude, the ratio increases as the reduced electric field grows.

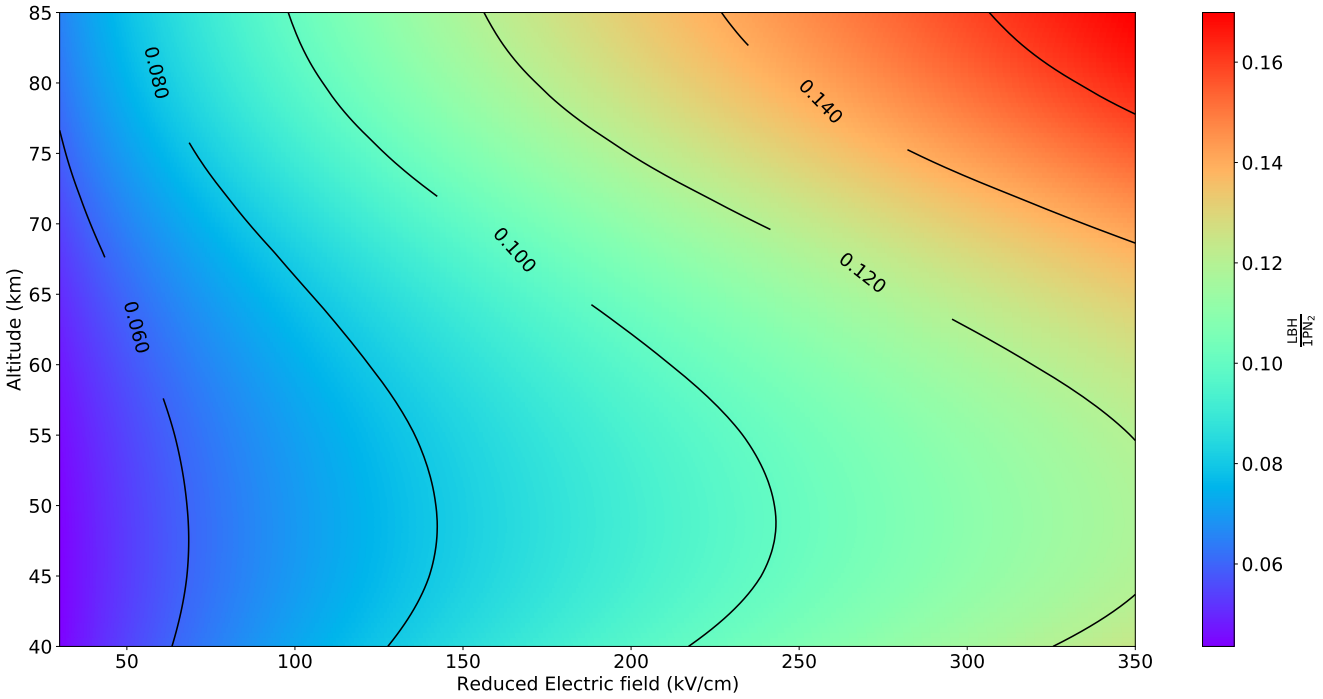

Figure 32: Parametric representation of the spectrophotometric ratio $\frac{\mathrm{LBH}}{1\mathrm{PN}_2}$ as a function of the altitude and the reduced electric field $E\times\frac{N}{N_0}$ computed through the equation (110) with a growth rate of $3.4\,\mathrm{ks}^{-1}$. The black curves represent sets of altitudes and electric fields (e.g., $\mathcal{S}_1$) for a given ratio in the aim to improve the readability.

On the other hand, the ratio $\frac{\mathrm{LBH}}{1\mathrm{NN}_2^+}$ has the advantage to be more sensitive to the electric field. The Figure 33 gives an example of parametric space for this ratio.

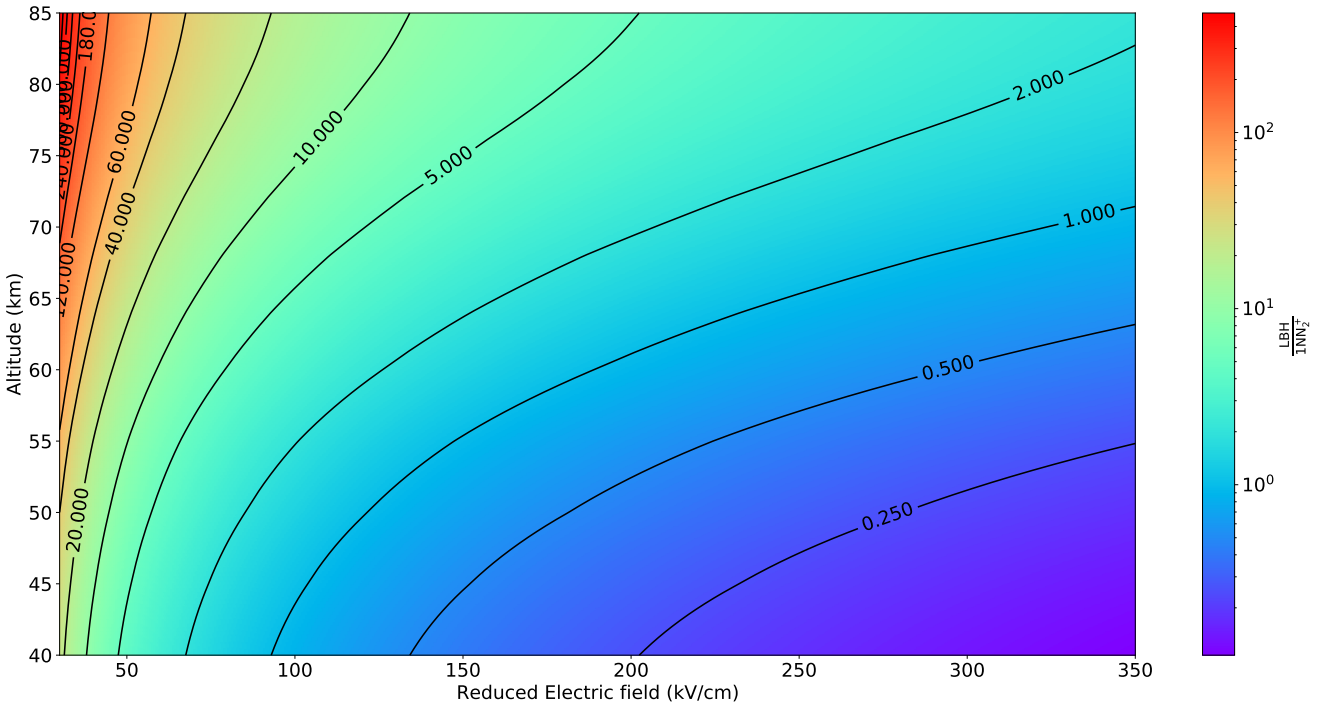

Figure 33: Parametric representation of the spectrophotometric ratio $\frac{\mathrm{LBH}}{1\mathrm{NN}_2^+}$ as a function of the altitude and the reduced electric field $E \times \frac{N}{N_0}$ computed through the equation (109) with a growth rate of $3.4\,\mathrm{ks}^{-1}$. The black curves represent sets of altitudes and electric fields (e.g., $\mathcal{S}_2$) for a given ratio in the aim to improve the readability.

Finally, the method can be summarized in five steps:

1. Determine the growth rate of the streamer through a linear fit in a logarithmic space of its expansion stage.

2. For a given ratio (e.g., $\frac{\mathrm{LBH}}{1\mathrm{PN}_2}$) computes its associated parametric space with the growth rate previously obtained.

3. Report the ratio obtained from measurements onto the parametric space

4. Compute the intersection according to the equation (106) to estimate the altitude.

5. Deduce the electric field in looking for the intersection between a ratio obtained from measurements and the altitude previously found.

IV.3 Results and discussion

IV.3.1 Validation with a control case

In order to validate our approach, we simulate the propagation of a positive streamer at 80 km over 5 km in constant air density in the same framework as *Ihaddadene and Celestin* [2017]. The streamer is initialized with a neutral Gaussian shaped plasma seed with a characteristic radius (see Equation (98)) σ of 190 m and immersed under a constant reduced electric field of $0.8E_k$. The figure 34 shows a cross-sectional view of the electric field at 1.94 ms. The peak electric field reaches a value of 175 V m^{-1} (∼117

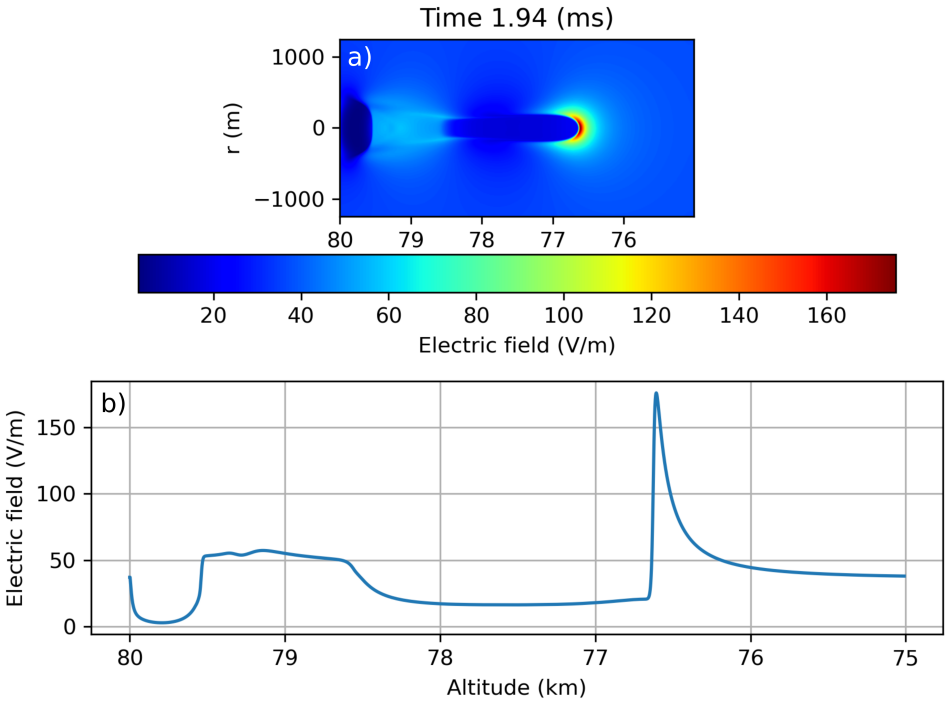

Figure 34: a) Cross section view of the electric field in a positive streamer propagating over 5 km altitude in a constant air density (80 km) at 1.94 ms. b) Electric field of the streamer along the z-axis.

$\frac{N}{N_0}$ kV cm^{-1}). As the air density does not change over the path of the streamer, the electric field in the streamer head stays constant (see Chapter II).

We want to estimate both the altitude and the peak electric field associated with this streamer from photometric data. These data are reproduced in calculating the number of photons per unit time for LBH, $1\,PN_2$, $2\,PN_2$, and $1\,NN_2^+$ over the volume of the simulation domain. The figure 35 shows the number of photons (a) for each band system as well as the ratio $\frac{\text{LBH}}{1\text{PN}_2}$ (b) and $\frac{2\text{PN}_2}{1\text{PN}_2}$ (c) that will be used for the analysis. Note that the ratios are not constant in time, but they stay consistent between them making possible to use them for analysis. We also calculate the ratio $\frac{\text{LBH}}{1\text{NN}_2^+}$ (not shown) with the aim of

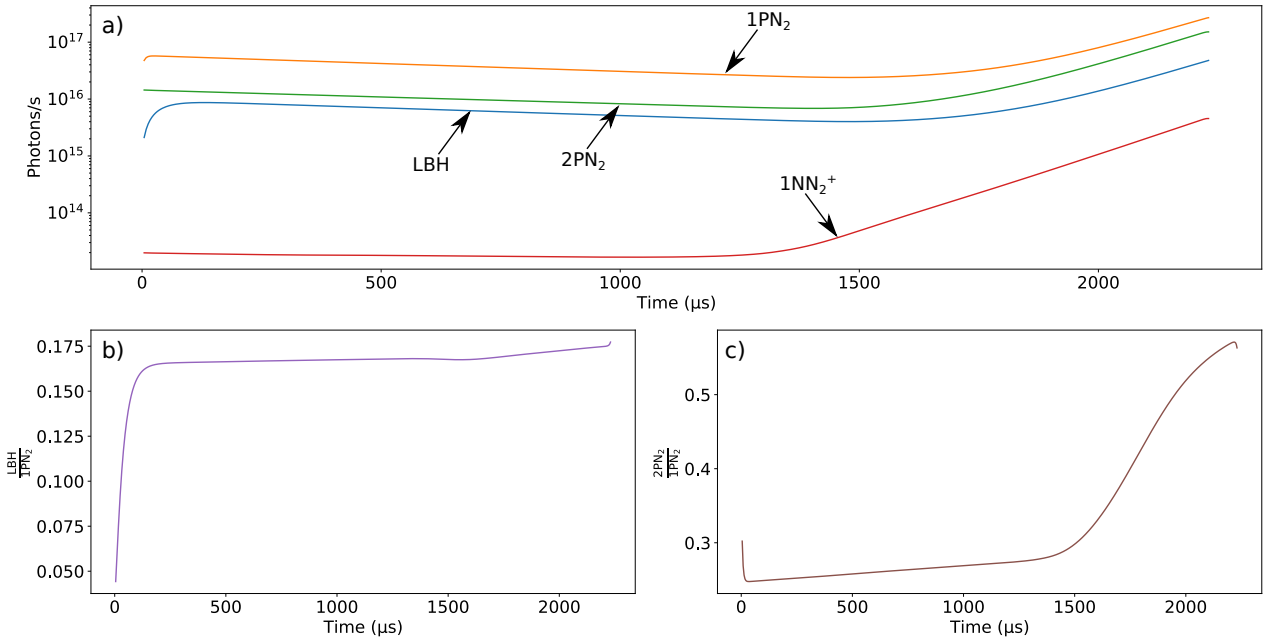

Figure 35: a) Number of photons per second for the LBH (blue), $1\,PN_2$ (orange), $2\,PN_2$ (green), and $1\,NN_2^+$ (red) spectral bands as function of time. b) Ratio $\frac{\text{LBH}}{1\text{PN}_2}$ as function of time deduced from the above panel. c) Same as b) for the ratio $\frac{2\text{PN}_2}{1\text{PN}_2}$. For all panels, the streamer propagation stage is considered to start at 1400 µs.

comparing the efficiency between the ratios $\frac{2\text{PN}_2}{1\text{PN}_2}$ and $\frac{\text{LBH}}{1\text{NN}_2^+}$.

The computation of the parameter space for a given ratio requires to know the expansion factor ν_e (equation (107)). This expansion factor is obtained through a linear fit of the photon flux of one of the four spectral bands shown in Figure 35a during the

propagation stage. We decide to choose the photon flux associated with LBH. This choice is mainly motivated by the fact that in practice (i.e., with real photometric data), LBH emission released by lightning is significantly weaker than the LBH emission produced by a sprite due to its attenuation by the atmosphere. A linear fit of the LBH spectral band gives a growth rate of $2090\,\mathrm{s}^{-1}$ for a coefficient of determination R^2 of 0.99. For an ambient reduced electric field of $0.8E_k$, *Kosar et al.* [2012] reported a growth rate around $2000\,\mathrm{s}^{-1}$ while *Ihaddadene and Celestin* [2017] reported a value almost 4 times larger. It is interesting to note that they found a growth rate of $2300\,\mathrm{s}^{-1}$ for an ambient reduced electric field of 12 $\frac{N}{N_0}$ $\mathrm{kV\,cm^{-1}}$ ($0.4E_k$).

Then, we compute the parameter space for these two ratios for an altitude included between 40 km to 85 km with a step of 0.3 km and a reduced electric field between 30 $\frac{N}{N_0}$ $\mathrm{kV\,cm^{-1}}$ and 267 $\frac{N}{N_0}$ $\mathrm{kV\,cm^{-1}}$ with a step of 0.2 $\frac{N}{N_0}$ $\mathrm{kV\,cm^{-1}}$ as shown in Figure 36 for the ratio $\frac{\mathrm{LBH}}{1\mathrm{PN}_2}$ and Figure 37 for the ratio $\frac{2\mathrm{PN}_2}{1\mathrm{PN}_2}$. For the ratio $\frac{\mathrm{LBH}}{1\mathrm{PN}_2}$ at the time given in Figure 34, the ratio reported in Figure 35b is of 0.172, while the ratio $\frac{2\mathrm{PN}_2}{1\mathrm{PN}_2}$ (Figure 35c) is of 0.494.

Figure 38 illustrates the equation (111) used to estimate the altitude. According to this figure, the altitude is 81 km. Using the parameter space shown in Figure 39 leads to a reduced electric field of 95 $\frac{N}{N_0}$ $\mathrm{kV\,cm^{-1}}$ ($119\,\mathrm{V\,m^{-1}}$) (green cross). Comparing with the real altitude of 80 km, the relative error on the altitude is 1.25 % while for the reduced electric electric it reaches ∼19 %.

We evaluate the efficiency of the same approach using the ratio $\frac{\mathrm{LBH}}{1\mathrm{NN}_2^+}$. Using the case shown in Figure 35a, we found a ratio $\frac{\mathrm{LBH}}{1\mathrm{NN}_2^+}$ of 14.473, which is reported on its related parameter space represented in Figure 39. Using the approach based on intersection illustrated in Figure 38, we found an altitude of 80 km. Note that, the set corresponding to the ratio $\frac{\mathrm{LBH}}{1\mathrm{PN}_2}$ has a certain thickness stemming from the range used to frame the corresponding ratio. According to the parameter space in Figure 39, it corresponds to a reduced electric field of 103 $\frac{N}{N_0}$ $\mathrm{kV\,cm^{-1}}$ ($154\,\mathrm{V\,m^{-1}}$). Comparing with the real altitude,

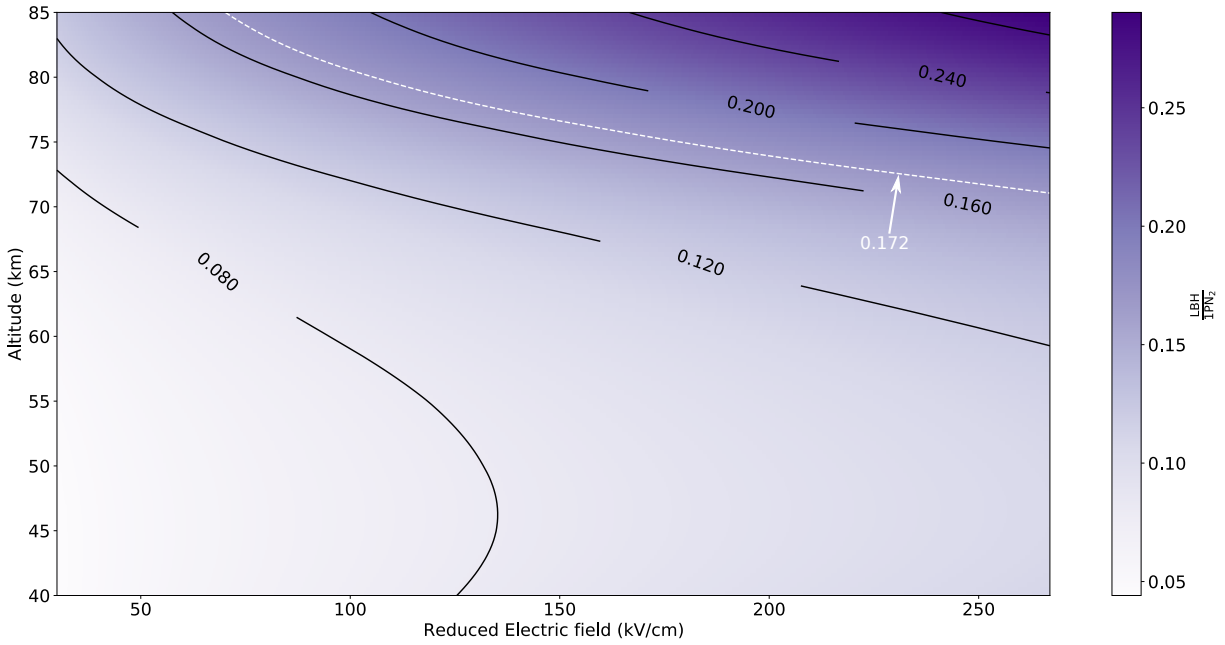

Figure 36: Parametric representation of the ratio $\frac{\mathrm{LBH}}{1\mathrm{PN}_2}$ as a function of the altitude and the reduced electric field. The dashed white curve illustrates a ratio of 0.172 found from Figure 35b. The black curves represent sets of altitudes and electric fields for a given ratios for the sake of clarity.

there is an excellent agreement, while we have a relative error less than 13 % for the reduced electric field.

We note that the use of the ratio $\frac{\mathrm{LBH}}{1\mathrm{NN}_2^+}$ gives both altitude and electric field better estimations. We suggest when it is possible to use the ratio $\frac{\mathrm{LBH}}{1\mathrm{NN}_2^+}$ instead of the ratio $\frac{2\mathrm{PN}_2}{1\mathrm{PN}_2}$. We also note that the knowledge of the altitude and the expansion factor can be used to estimate the ambient electric field in which the streamer propagates. Indeed, *Kosar et al.* [2012] reported that the expansion factor ν_e is strongly dependent on the ambient electric field. *Ihaddadene and Celestin* [2017] have calculated this expansion factor (see Table 4 in their paper). According to this, we should find an ambient electric field around 12 $\frac{N}{N_0}$ kV cm^{-1}, which is not the one used in our simulation ($0.8E_k$ (i.e., 24 $\frac{N}{N_0}$ kV cm^{-1})). A significant difference between both simulation is the characteristic

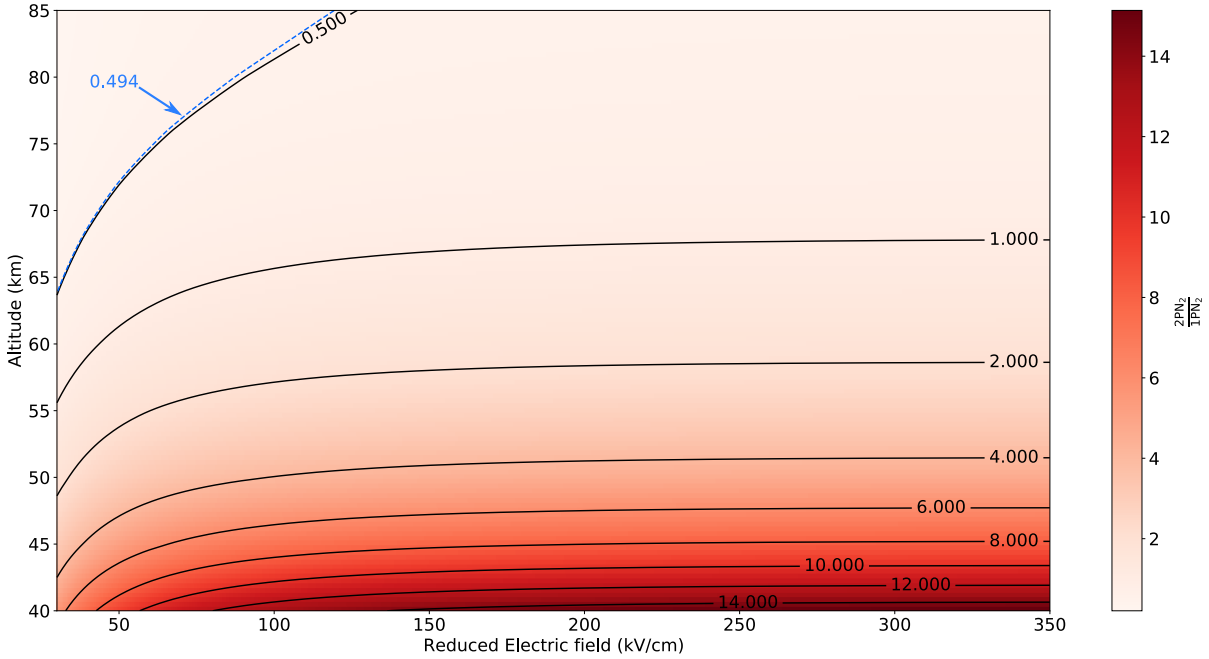

Figure 37: Parametric representation of the ratio $\frac{2PN_2}{1PN_2}$ as a function of the altitude and the reduced electric field. The dashed blue curve illustrates the ratio of 0.494 found from Figure 35c. The black curves represent sets of altitudes and electric fields for a given ratios for the sake of clarity.

size of the seed used to trigger the streamer. This observation let us to think that the characteristic size of the seed may have a strong impact on the expansion factor in addition to the ambient electric field. This observation is dissected in more details in Section V.5.

We prove that the application of the method based on [*Ihaddadene and Celestin*, 2017] is capable to infer the electric field and the altitude for a streamer coming from numerical simulations. The use of this method on real spectrophotometric data is reported in the next section.

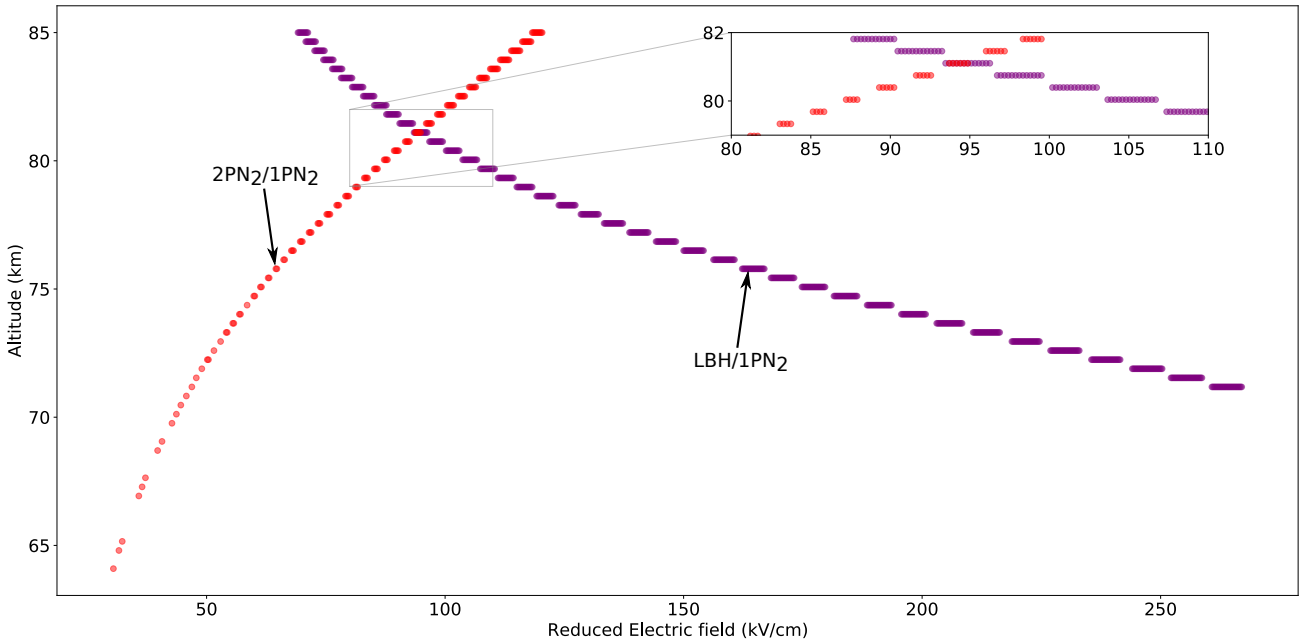

Figure 38: Illustration of the intersection between the set of altitudes and reduced electric fields defined by the ratio $\frac{\text{LBH}}{1\text{PN}_2}$ (red dots) and the ratio $\frac{2\text{PN}_2}{1\text{PN}_2}$ (purple dots). A zoom-in over the intersection area is shown at the top-right of the figure.

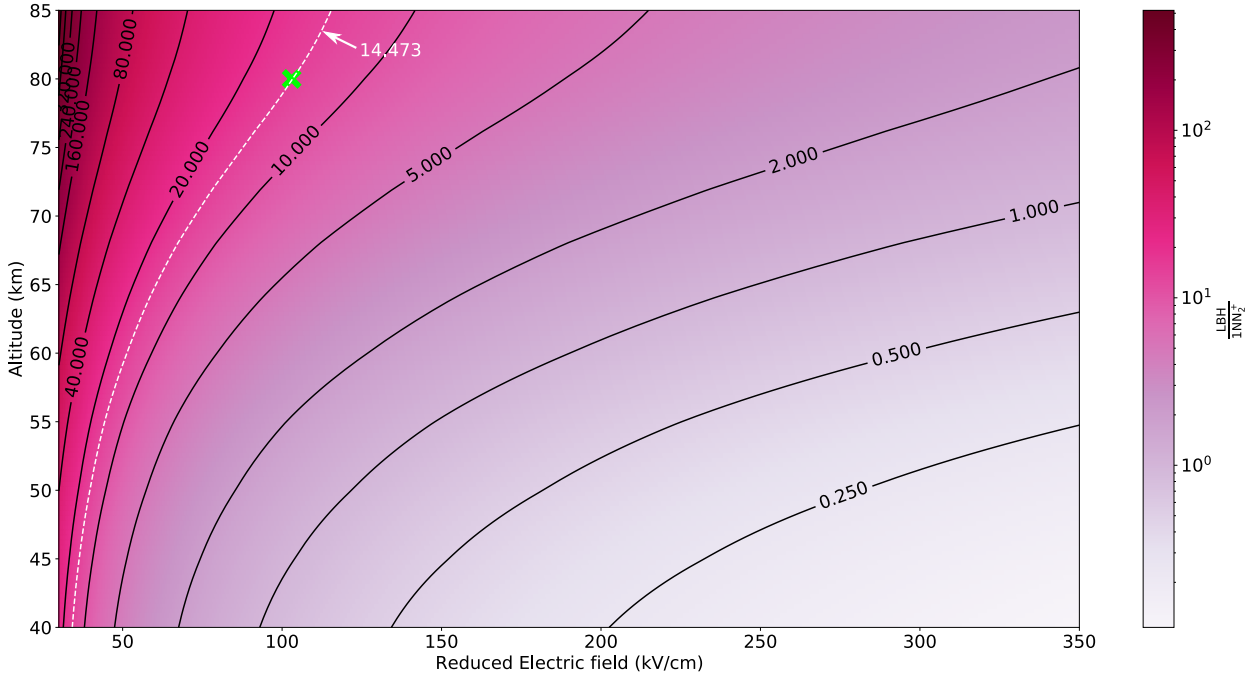

Figure 39: Parametric space for the ratio $\frac{\text{LBH}}{1\text{NN}_2^+}$ as a function of the altitude and the reduced electric field. The dashed white curve illustrates the ratio of 14.473 found from Figure 35a. The black curves show specific values of the ratio for the sake of clarity. The green cross symbolizes the altitude and the electric field obtained through the method presented in this chapter.

IV.3.2 Influence of the varying air density

The analysis conducted in the section IV.3.1 has been realized in constant air density. However, we show in the chapter V, section V.4 the use of a constant non-air density has an influence of the spectroscopic ratio.

In this section, we evaluate the relative uncertainty we obtain when the method describes in section IV.2 is applied to a control case in varying air density.

We simulate the propagation of a positive streamer starting at 80 km altitude propagating downward over 5 km. The streamer is immersed in a reduced ambient electric field of $1E_k$, and triggered from an inhomogeneity neutral Gaussian plasma with a characteristic size σ =190 m situated at z =244 m. The figure 40a shows a cross sectional view of the electric field for the positive streamer describes below and its electric field along the altitude (bottom panel). Instead of a value of 175 V/m in constant density

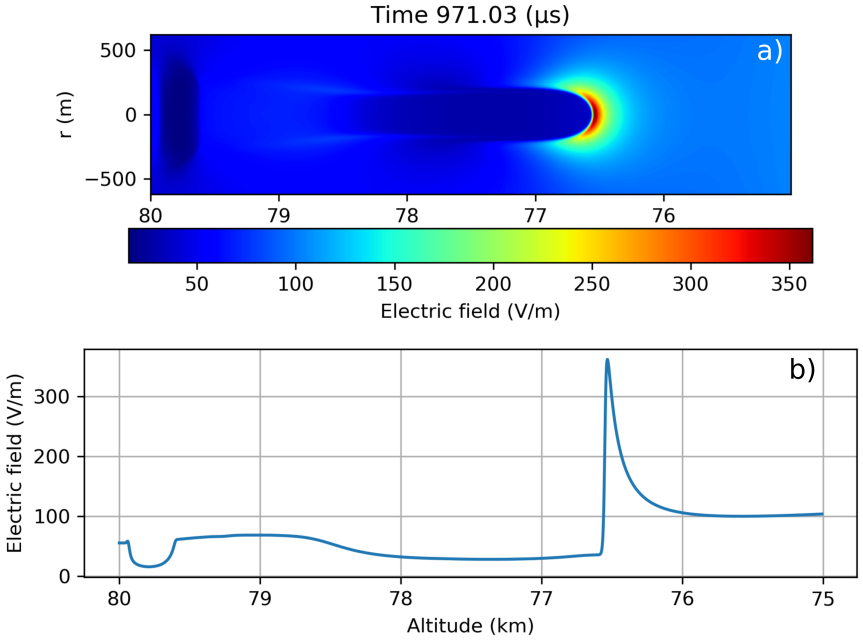

Figure 40: a) Cross section view of the electric field in a positive streamer propagating over 5 km altitude in an varying air density (80 km) at 971.03 µs. b) Electric field of the positive streamer along the altitude.

air, the peak electric field reaches a value of $362\,\mathrm{V\,m^{-1}}$ ($\sim 137\ \frac{N}{N_0}\ \mathrm{kV\,cm^{-1}}$).

As described in the section IV.3.1 the evaluation of the altitude and the electric field from spectrophotometric measurements requires three quantities: The growth rate of the streamer calculated during its expansion stage, the ratios $\frac{\mathrm{LBH}}{1\mathrm{PN_2}}$ and $\frac{\mathrm{LBH}}{1\mathrm{NN_2^+}}$. This information is available in Figure 41.

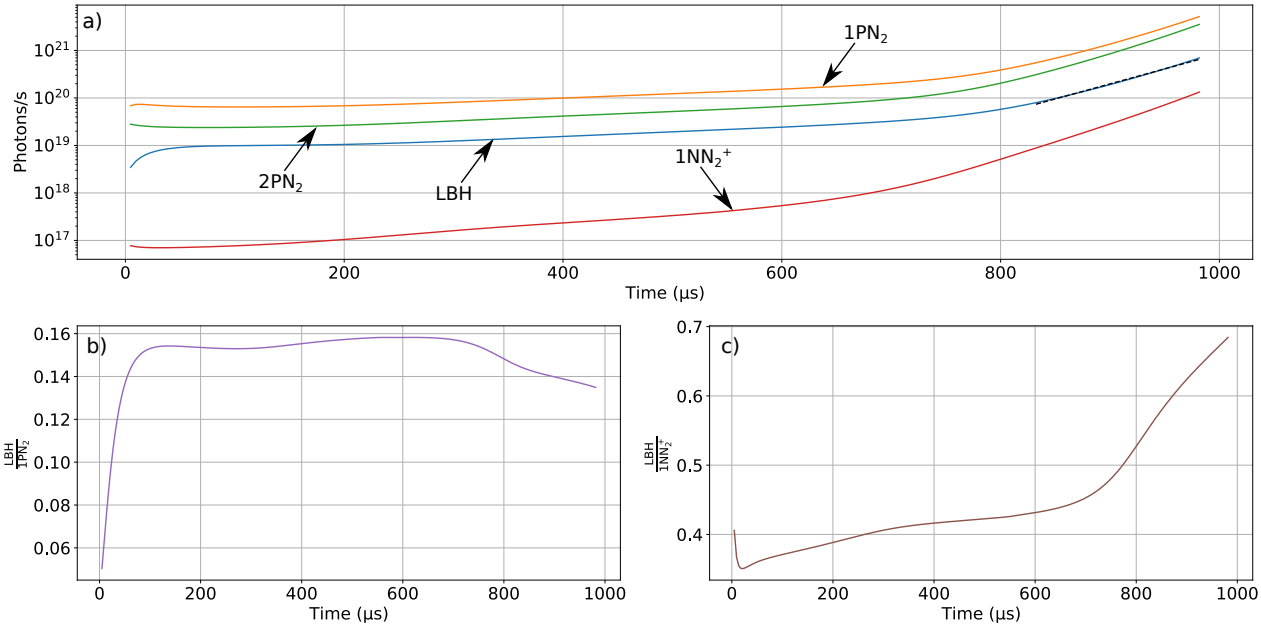

Figure 41: a) Number of photons per second for the LBH (blue), $1\,\mathrm{PN_2}$ (orange), $2\,\mathrm{PN_2}$ (green), and $1\,\mathrm{NN_2}^+$ (red) spectral bands as function of time. b) Ratio $\frac{\mathrm{LBH}}{1\mathrm{PN_2}}$ as function of time deduced from the above panel. c) Same as b) for the ratio $\frac{\mathrm{LBH}}{1\mathrm{NN_2^+}}$. For all panels, the streamer propagation stage is considered to start at 832 µs.

From the linear fit done over the LBH band system in Figure 41a, we found a growth rate of $6353\,\mathrm{s^{-1}}$. At 971.03 µs we found from Figure 41b a ratio $\frac{\mathrm{LBH}}{1\mathrm{PN_2}}$ of 0.135 and for the ratio $\frac{\mathrm{LBH}}{1\mathrm{NN_2^+}}$ of 5.369. The parametric spaces for these two ratios are reported in Figures 42 and 43 , respectively.

The intersection used to estimate the altitude is reported in Figure 44

According to this figure we found an altitude of 74 km that we report in Figure 43 to

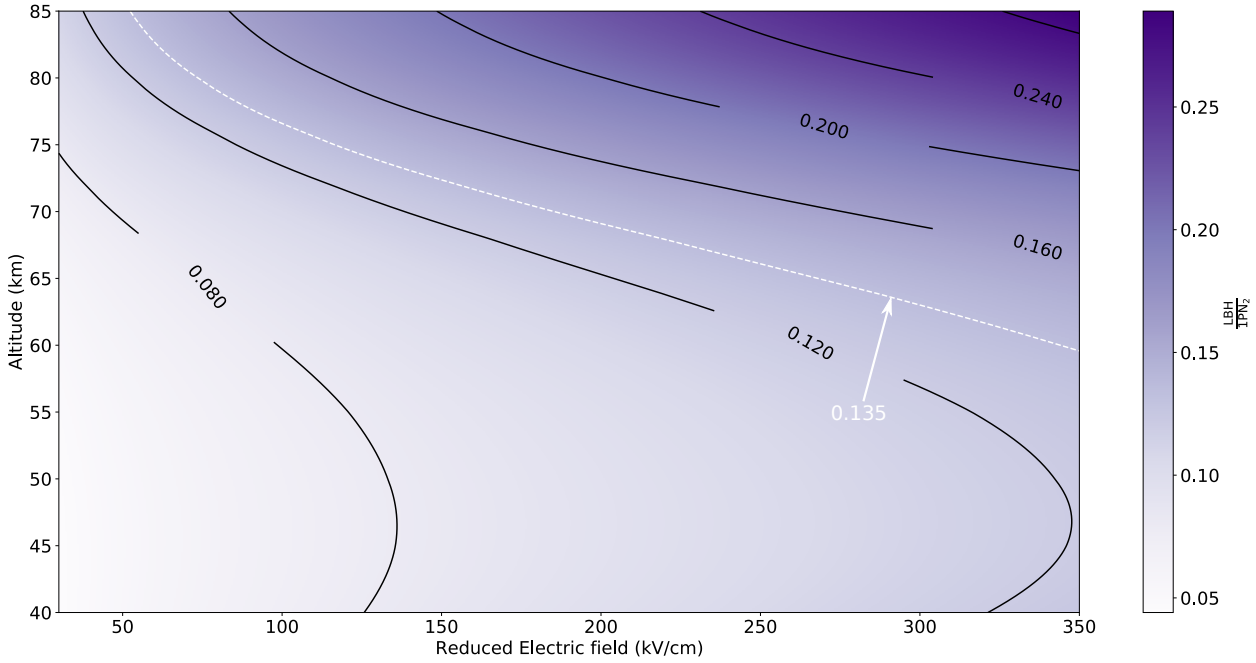

Figure 42: Parametric representation of the ratio $\frac{\mathrm{LBH}}{\mathrm{1PN_2}}$ as a function of the altitude and the reduced electric field. The dashed white curve illustrates a ratio of 0.135 found from Figure 41b. The black curves represent sets of altitudes and electric fields for a given ratios for the sake of clarity.

estimate the peak electric field at 131 $\frac{N}{N_0}$ kV cm^{-1} or 505 V m^{-1}at this altitude. Using Figure 41, we found for our a streamer an altitude of 76.5 km and a peak electric field of 362 V m^{-1} (137 $\frac{N}{N_0}$kvcm), meaning that we have a relative error of $\sim 3\,\%$ for the altitude and a relative error 39.5 % for the peak electric field. A summary of the results found in constant and varying air densities is reported in Table 5.

These results highlights the fact that the framework developed by *Ihaddadene and Celestin* [2017] can not be used for streamers propagating in varying air density. Relatively speaking, the error over the altitude is not very excessive and it is still acceptable but this is not the case for the electric field. It is important to keep in mind that in practice, the medium in which streamers are propagating is a varying air density and the use of the method described in this chapter to infer the altitude and the electric field

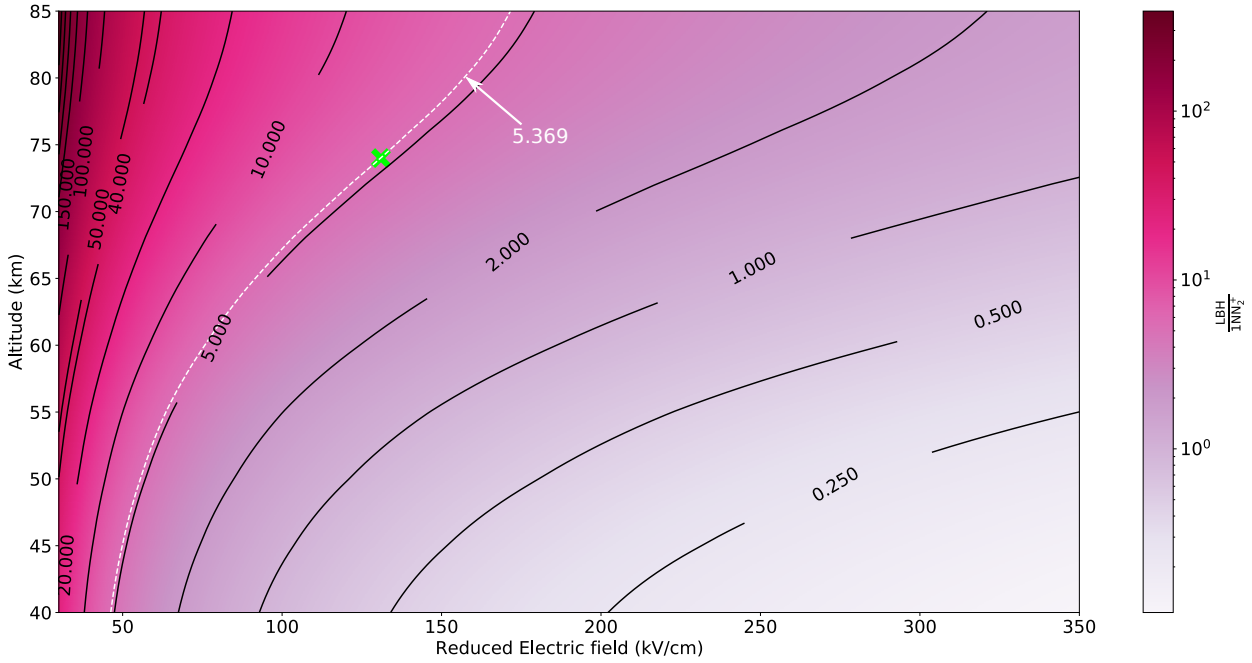

Figure 43: Parametric space for the ratio $\frac{\text{LBH}}{1\text{NN}_2^+}$ as a function of the altitude and the reduced electric field. The dashed white curve illustrates the ratio of 5.369 found from Figure 41a. The black curves show specific values of the ratio for the sake of clarity. The green cross symbolizes the altitude and the electric field obtained through the method presented in this chapter.

is prone to errors, particularly about the electric field as it varies according to $\frac{N}{N_0}$.

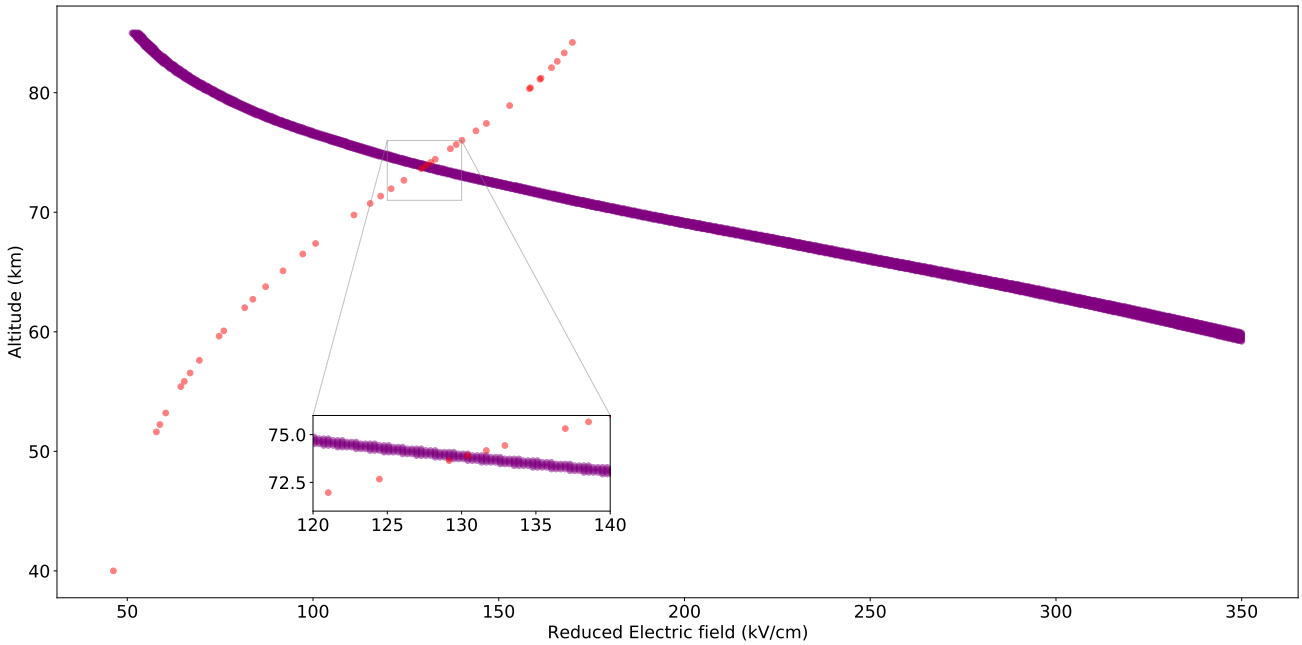

Figure 44: Illustration of the intersection between the set of altitudes and reduced electric fields defined by the ratio $\frac{\text{LBH}}{1\text{PN}_2}$ (red dots) and the ratio $\frac{2\text{PN}_2}{1\text{PN}_2}$ (purple dots). A zoom-in over the intersection area is shown at the top-right of the figure.

Air density	$h_{\texttt{simu}}$ (km)	$E^{\texttt{peak}}_{\texttt{simu}}$ ($\frac{N}{N_0}$ kV cm^{-1})	ν_e (s^{-1})	$h_{\texttt{model}}$ (km)	$E^{\texttt{peak}}_{\texttt{model}}$ ($\frac{N}{N_0}$ kV cm^{-1})
Constant	80	117 (176 V m^{-1})	2090	80	103 (154 V m^{-1})
Varying	76.5	137 (362 V m^{-1})	6353	74	131 (505 V m^{-1})

Table 5: A summary of the altitude $h_{\texttt{model}}$ and the peak electric field $E^{\texttt{peak}}_{\texttt{model}}$ found from the application of the method described in Section IV.2 with the ratio $\frac{\text{LBH}}{1\text{NN}_2^+}$ for a case in constant and varying air densities as well as the altitudes $h_{\texttt{simu}}$ and the peak electric fields $E^{\texttt{peak}}_{\texttt{simu}}$ obtained from the simulations.

IV.3.3 Application to a sprite event recorded by ISUAL

The mission instrument ISUAL on-board the FORMOSAT-2 satellite recorded numerous sprite events. For the application of the method described above, we use the two sprites reported by *Kuo et al.* [2005]. This event has the advantage to have been studied by *Kuo et al.* [2005] and *Liu et al.* [2006a]. The raw brightness timeseries from the six photometers are plotted in Figure 45. These six photometers composed the spectrophotometer instrument on-board ISUAL along with a CCD imager to realize observations in a limb-viewing geometry, and an array of photometers designed to measure the vertical and temporal structures of TLEs. The Table 6 reports the wavelengths used by the ISUAL spectrophotometers and associated details.

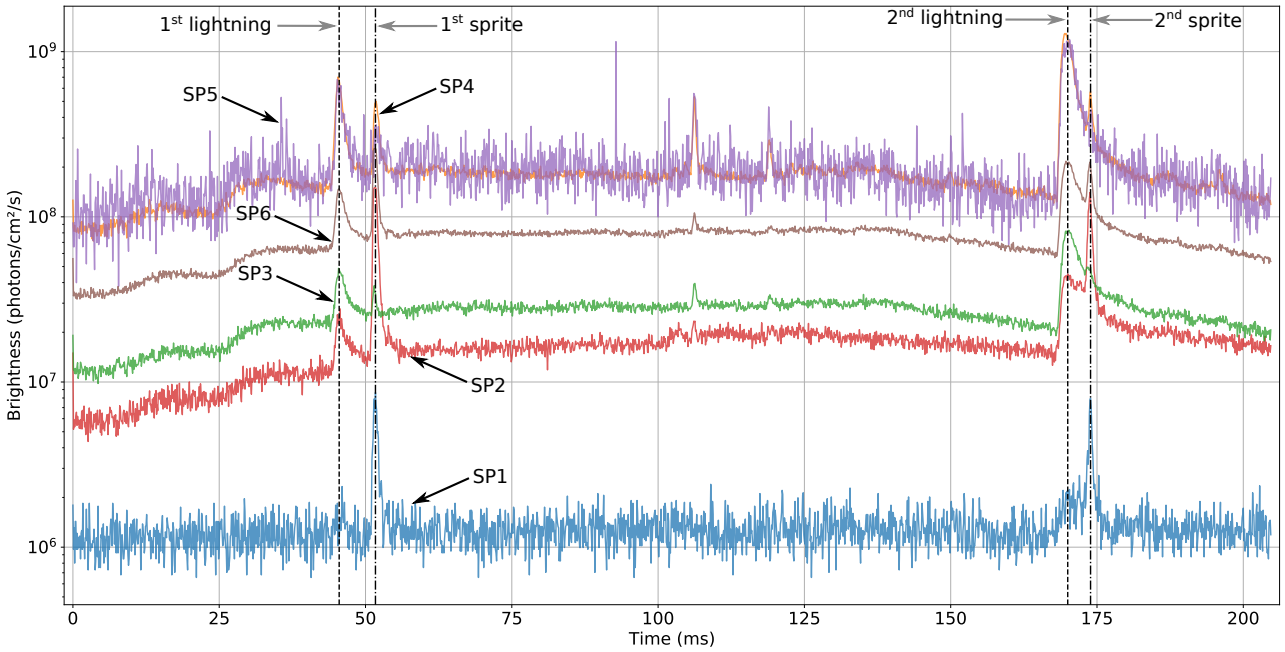

Figure 45: Evolution of the raw brightness measured by the six photometers of the ISUAL instrument for the event recorded at 2004/07/18 on 21:30:15.316 UT. Each photometer is indicated by a black arrow. The two lightnings are symbolized by the dashed vertical lines (45.5 ms and 170 ms) with their associated grey arrows. The two delayed sprites are shown through the use of dash-dotted vertical lines (51.7 ms and 173.9 ms) and their associated grey arrows.

Channel	Wavelength (bandwidth) (nm)	Remarks
SP1	150–290	LBH broadband
SP2	337 (5.6)	$2\,PN_2$ (0,0)
SP3	391.4 (4.2)	$1\,NN_2^+$ (0,0)
SP4	608.9–753.4	$1\,PN_2$ broadband
SP5	777.4	Lightning (O) narrowband
SP6	228.2–410.2	$2\,PN_2 + 1\,NN_2^+$ broadband

Table 6: Wavelength used for each spectrophotometer on-board ISUAL. Adapted from *Kuo et al.* [2005].

In Figure 45, we can identify four clear transient signatures in the brightness. According to pictures recorded at the same time by the mission [*Kuo et al.*, 2005], the first peak in the SP2 channel around 45 ms corresponds to the parent lightning leading to a delayed sprite visible in the photometer data by a second peak at ∼52 ms. The third peak at ∼170 ms is associated with a second cloud-to-ground lightning and the production of a second delayed sprite ∼ 174 ms. Note that the first event is weakly affected by the lightning signal while for the second one, the lightning signal significantly adds up with the sprite signal required signal processing to separate its signature from causative cloud-to-ground lightning component.

For this study, we focus on the ratios $\frac{\text{LBH}}{1\text{PN}_2}$ and $\frac{\text{LBH}}{1\text{NN}_2^+}$ as we have previously shown that they gives more accurate results. Before using data, these must be corrected by a constant factor to take the impact of the bandfilter associated with each ISUAL photometers into account. The value for the band systems LBH, $1\,PN_2$, $2\,PN_2$, and $1\,NN_2^+$ and their mapping with ISUAL photometers are reported in the Table 7. Figure 46a

Band system	LBH	$1\,PN_2$	$2\,PN_2$	$1\,NN_2^+$
SP photometer	SP1	SP4	SP2	SP3
Fraction of the total emission	11 %	11 %	27.8 %	66 %

Table 7: Fraction of the total emission received by SP1, SP2, SP3, and SP4 ISUAL photometers and the related band systems. Adapted from *Liu et al.* [2006a].

shows SP1 and SP4 for the first delayed sprite at ∼51 ms as well as the ratio $\frac{\text{LBH}}{\text{1PN}_2}$ (Figure 46b) while Figure 47a and b are for SP1 and SP3 for the same event. SP1, SP3, and

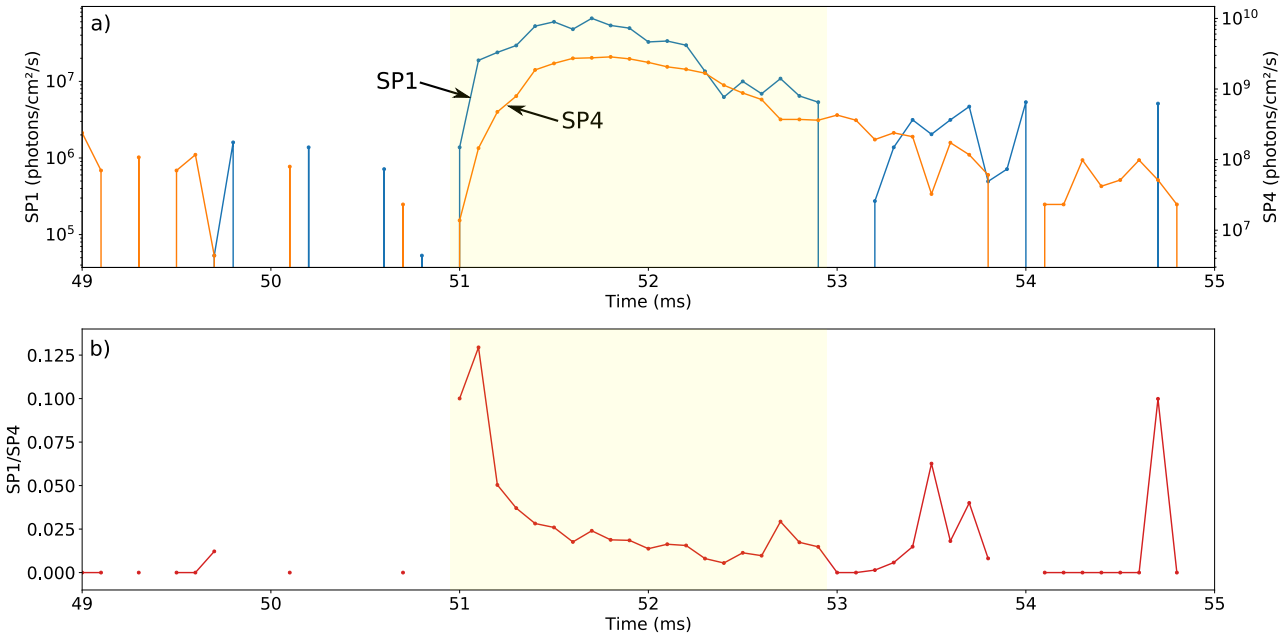

Figure 46: a) Temporal evolution of the brightness of SP1 (dotted blue curve) and SP4 (dotted orange curve) photometers. b) Ratio SP1/SP4 (i.e., $\frac{\text{LBH}}{\text{1PN}_2}$). The figure is a zoom-in view of the first delayed sprite reported in Figure 45. The light yellow rectangle highlights the sprite event.

SP4 channels have been corrected by their corresponding factors reported in Table 7. The SP1 channel signal is subtracted by its average value corresponding to the signal's baseline. The SP3 channel signal is processed like SP1. The SP4 channel signal is first subtracted by the average value of its first 10 ms, then the signal obtained is subtracted by its average value. At the end of each processing, negative values are nullified to avoid undefined behavior due to negative values in logarithmic space.

The growth rate ν_e is determined by applying a linear fit at the early growing phase of the SP1 channel. We found a coefficient factor of 11.4 ks^{-1}. Figure 46b shows that the ratio is of 0.130 at 51.1 ms. Figure 47b shows that the ratio for $\frac{\text{LBH}}{\text{1NN}_2^+}$ at the same time is

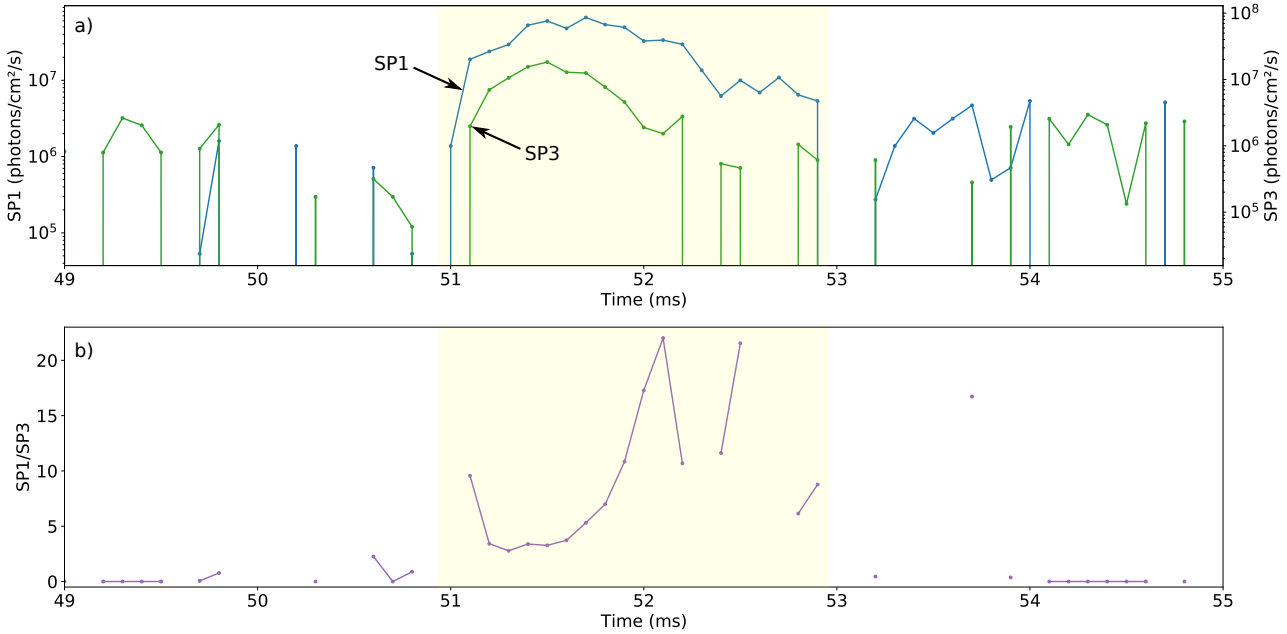

Figure 47: a) Temporal evolution of the brightness of the SP1 (dotted blue curve) and the SP3 (dotted green curve) photometers. b) Ratio SP1/SP3 (i.e., $\frac{\mathrm{LBH}}{1\mathrm{NN}_2^+}$). The Figure is a zoom-in view of the first delayed sprite reported in Figure 45. The light yellow rectangle highlights the sprite event.

of 3.33. With this information, we compute the parameter space for the two ratios and their intersection as defined in the equation (111). The parameter space for the ratio $\frac{\mathrm{LBH}}{1\mathrm{PN}_2}$, $\frac{\mathrm{LBH}}{1\mathrm{NN}_2^+}$, and the intersection are reported in Figure 48, 49 and 50, respectively.

According to the intersection in Figure 50, the altitude of the inception of the sprite is at 72.6 km altitude. Setting this value in Figure 49, the reduced electric field obtained is of $\sim$150 $\frac{N}{N_0}$ kV cm^{-1} corresponding to an electric field of 417 V m^{-1}. In comparison, *Kuo et al.* [2005] found an altitude of 60 km and an electric field of $3.6E_k$ ($\sim$ 108 $\frac{N}{N_0}$ kV cm^{-1}). However their estimate of the electric field does not take into consideration the correction factor due to the spatial shift between the electric field and spectrophotometric species [*Celestin and Pasko*, 2010] and the altitude found was not based on spectrophotometric analysis. If we conduct the same work as described above without the use of

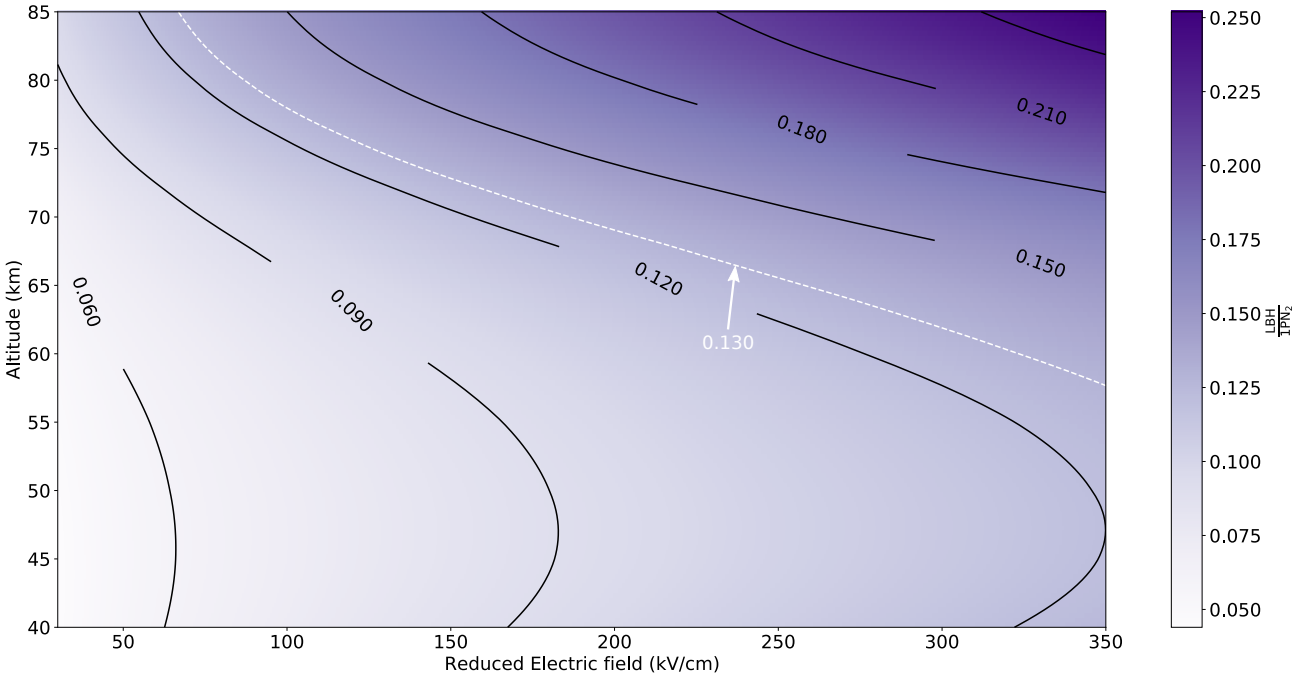

Figure 48: Parametric space illustrating the evolution of the ratio $\frac{\text{LBH}}{1\text{PN}_2}$ as a function of the reduced electric field and the altitude. The black curves show specific values of the ratio for the sake for clarity. The dashed white curve corresponds to the ratio of 0.130 associated with the sprite delayed sprite event.

correction factors, we found an electric field of $\sim$54 $\frac{N}{N_0}$ kV cm^{-1} or $\sim$150 V m^{-1}, which is consistent with what we can expect in a streamer head. For the altitude, the ratio we used corresponds to a specific time in the sprite propagation as recorded by ISUAL photometers. As we did the analysis at the inception of the sprite, the observed event was not a fully developed sprite but rather a bunch of streamers. The altitude found by our method could be consistent with the altitude associated with streamers propagating downward and triggered at higher altitudes [e.g., *Qin et al.*, 2014]. Furthermore, if we use the expansion factor computed through the linear fit and comparing it with those in *Ihaddadene and Celestin* [2017], using *Kosar et al.* [2012] method, we can deduce that the ambient electric field is around 28 $\frac{N}{N_0}$ kV cm^{-1}, which is consistent with previous

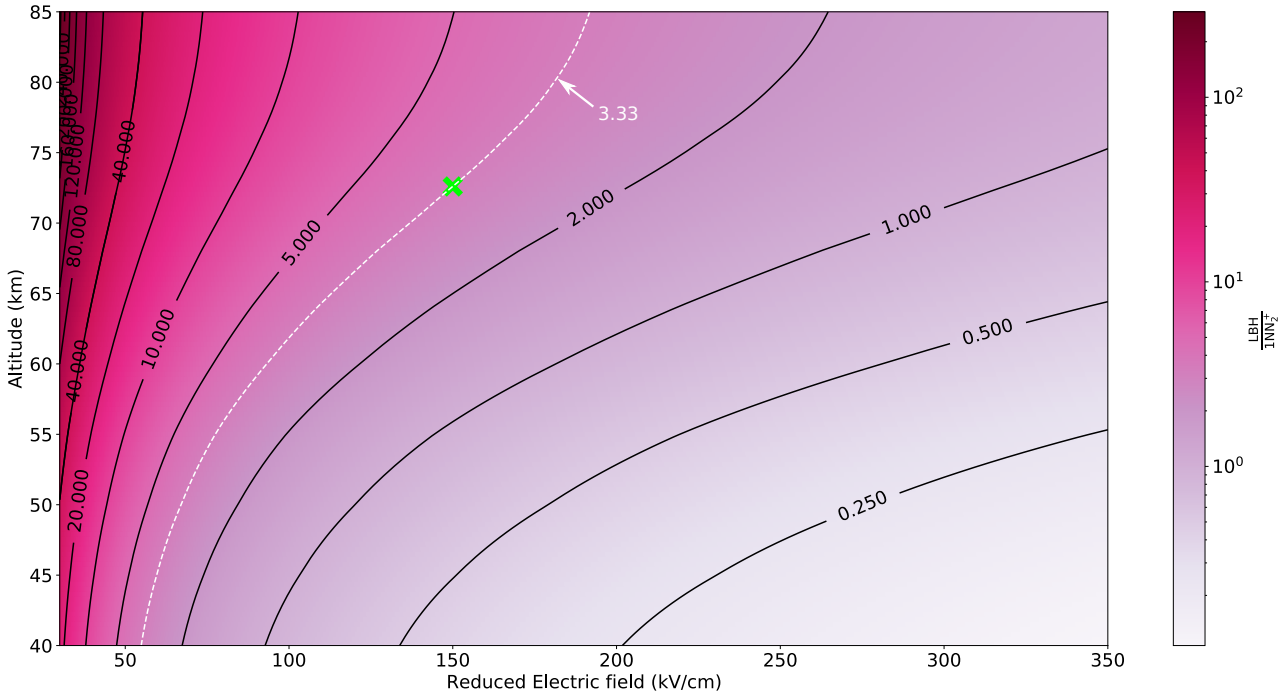

Figure 49: Parametric space illustrating the evolution of the ratio $\frac{\text{LBH}}{1\text{NN}_2^+}$ as a function of the reduced electric field and the altitude. The black curves show specific values of the ratio for the sake for clarity. The dashed white curve corresponds to the ratio of 3.33 associated with the delayed sprite event. The green cross symbolizes the altitude and the electric field associated with the sprite.

simulations of relaxing electrostatic field in the ionosphere [e.g., *Qin et al.*, 2013a].

We conduct the same analysis for the second sprite event localized at ∼174 ms (the magenta line in Figure 45). However, for the second event the SP3 and SP4 channels contain both emission from sprite and lightning. In order to remove this lightning contribution, and in complement to the signal processing mentioned earler, we fit the lightning emission between 169.5 ms and 172.5 ms with an exponential decay centered at 169.5 ms for the two photometers as suggested by *Kuo et al.* [2005]. The fit is realized through Levenberg-Marquardt algorithm on $N_0 \exp\left[-\lambda\left(t - t_0\right)\right]$, where N_0 is a constant, λ is the decay constant and t_0 is the centered time. Then, we use the fitted function to

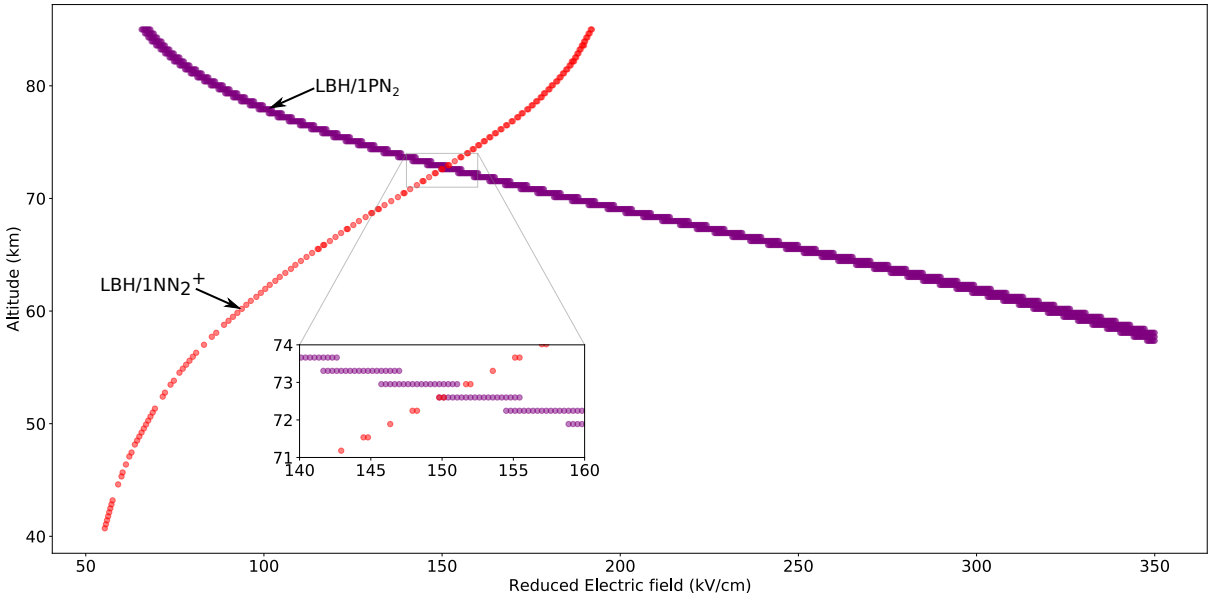

Figure 50: Illustration of the intersection between the set of altitudes and reduced electric fields defined by the ratio $\frac{\text{LBH}}{1\text{PN}_2}$ (purple dots) and the ratio $\frac{\text{LBH}}{1\text{NN}_2^+}$ (red dots). A zoom-in view over the intersection area is shown at the bottom-left of the figure.

remove the lightning contribution from 169.5 ms till the end of the signal. Figure 51 and Figure 52 show the SP4 and SP3 processed signal, respectively.

Using the same approach as described above to determine the expansion factor ν_e, we found it at 1.4 ks^{-1} and a coefficient of determination R^2 is of 0.83, which less than the previous one but still sufficiently meaningful for the analysis. The ratio $\frac{\text{LBH}}{1\text{PN}_2}$ at 173.4 ms is 0.08, and the ratio $\frac{\text{LBH}}{1\text{NN}_2^+}$ is 7.17. The computation of parameter space for these two ratios is realized as mentioned above, and the intersection between the two ratios is shown in Figure 53. We found an altitude of ∼64 km corresponding to the barycenter (obtained through arithmetic mean) between the first red point at ∼75 $\frac{N}{N_0}$ kV cm^{-1} and ∼78 $\frac{N}{N_0}$ kV cm^{-1}. The electric field deduced in Figure 54 is of 79 $\frac{N}{N_0}$ kV cm^{-1}.

For the second delayed sprite, we found an altitude lower than the first sprite. The electric field is also weaker despite the fact that we are at the beginning of the event.

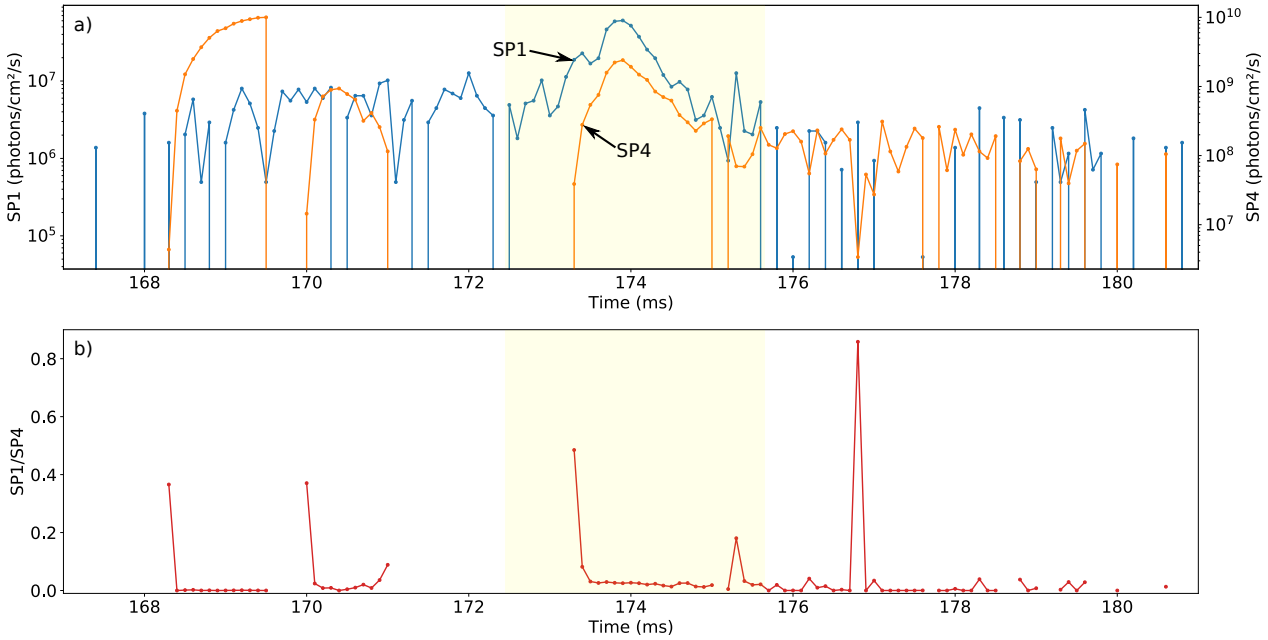

Figure 51: a) Temporal evolution of brightness of SP1 (dotted blue curve) and SP4 (dotted orange curve) photometers. b) Ratio SP1/SP4 (i.e., $\frac{\mathrm{LBH}}{\mathrm{1PN_2}}$). The figure is a zoom-in view over the second delayed sprite reported in Figure 45. The light yellow rectangle highlights the sprite event for the sake of readability.

However, the expansion factor reveals that the ambient electric field is weak and may be below 12 $\frac{N}{N_0}\mathrm{kV\,cm^{-1}}$. Note that, the event studied here is more complex than the previous one. According to the pictures taken by the ISUAL CCD camera [*Kuo et al.*, 2005], the second delayed sprite seems to contain at least two sprites making the present analysis less relevant since incoherent sources of light are observed by the photometers.

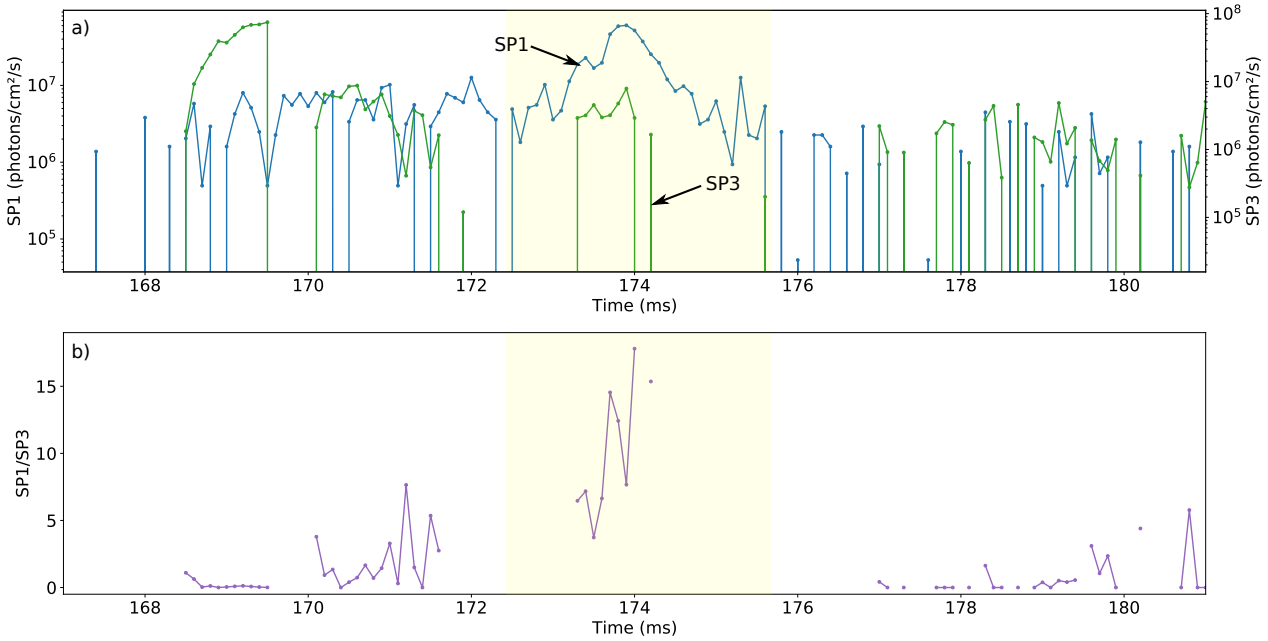

Figure 52: a) Temporal evolution of the brightness of SP1 (dotted blue curve) and SP3 (dotted green curve) photometers. b) Ratio SP1/SP3 (i.e., $\frac{\mathrm{LBH}}{1\mathrm{NN}_2^+}$). The figure is a zoom-in view over the first delayed sprite reported in Figure 45. The light yellow rectangle highlights the sprite event for the sake of readability.

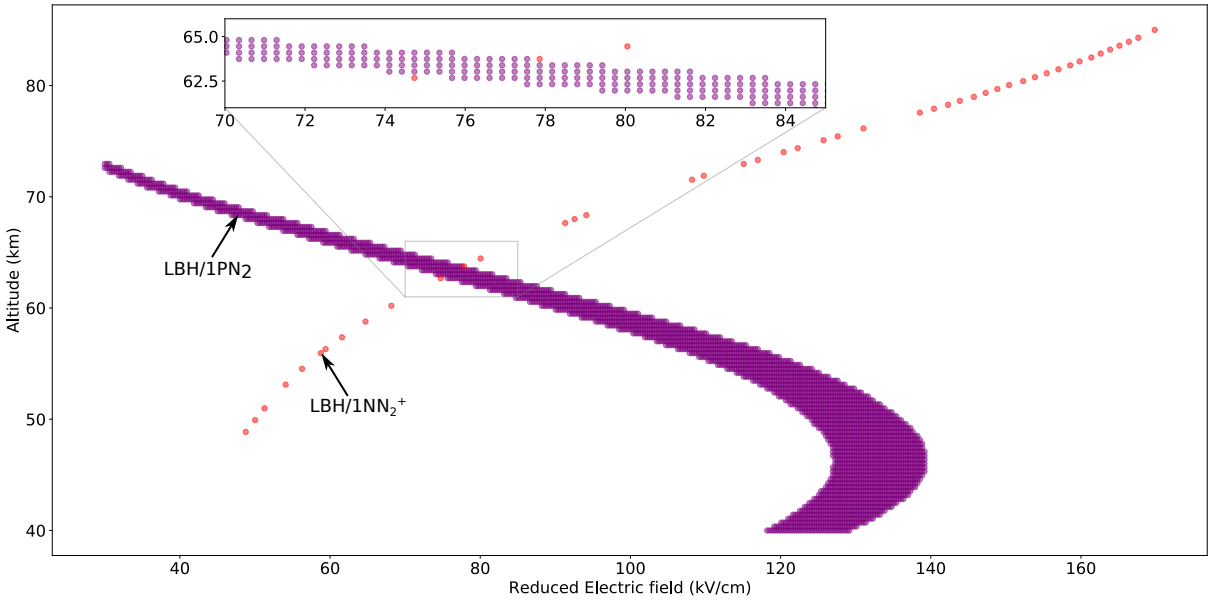

Figure 53: Illustration of the intersection between the set of altitudes and reduced electric fields defined by the ratio $\frac{\text{LBH}}{1\text{PN}_2}$ (purple dots) and the ratio $\frac{\text{LBH}}{1\text{NN}_2^+}$ (red dots). A zoom-in view over the intersection area is shown at the top of the figure.

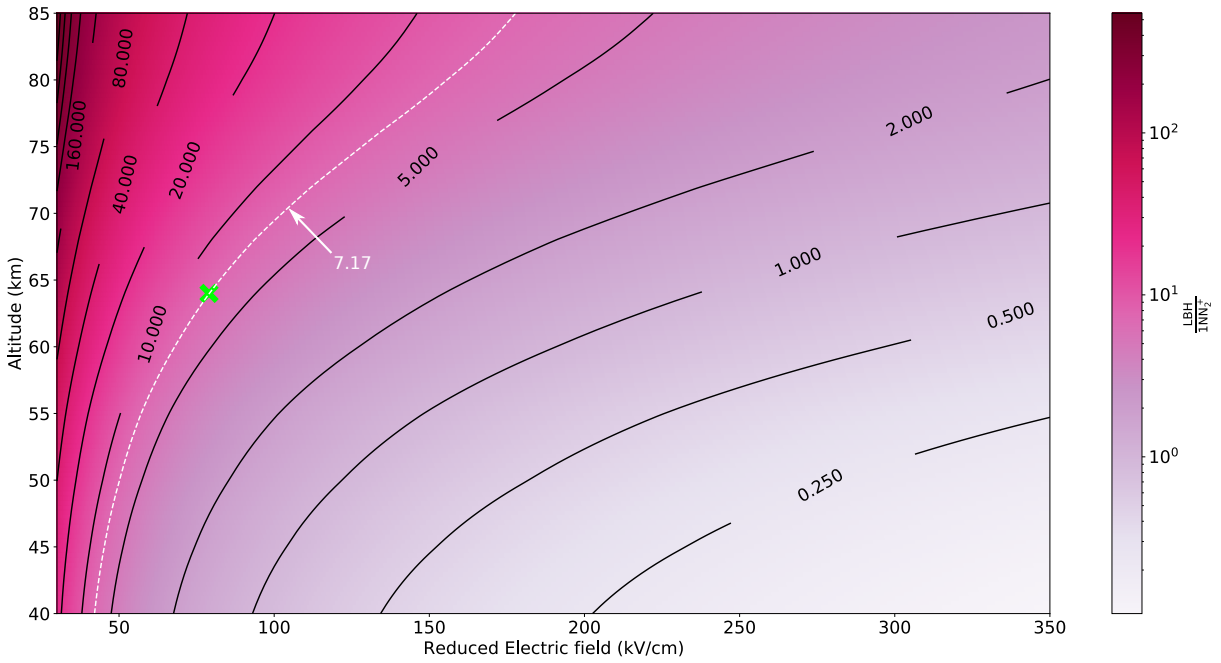

Figure 54: Parametric representation of the ratio $\frac{\mathrm{LBH}}{1\mathrm{NN}_2^+}$ as function of the reduced electric field and the altitude. The black curves show specific values of the ratio for the sake for clarity. The dashed white curve corresponds to a ratio of 7.17 associated with the delayed sprite event. The green cross symbolizes the altitude and the electric field obtained through the method presented in this chapter.

IV.4 Conclusion

In this chapter, we demonstrate the feasibility to use the ratio method proposed by [*Ihaddadene and Celestin*, 2017] with the ratios $\frac{\mathrm{LBH}}{1\mathrm{PN}_2}$, $\frac{2\mathrm{PN}_2}{1\mathrm{PN}_2}$, and $\frac{\mathrm{LBH}}{1\mathrm{NN}_2^+}$ to infer the altitude and the electric field associated with a sprite streamer in their early stages. Note that the method reported here used a first order approximation, which can be significantly improved using a minimization method to avoid the use of discrete value ratio. We report that the use of ratios $\frac{\mathrm{LBH}}{1\mathrm{PN}_2}$ and $\frac{\mathrm{LBH}}{1\mathrm{NN}_2^+}$ give more accurate results on the validation case.

For the first time, we apply this spectrophotometric method on to real data of sprite events reported by *Kuo et al.* [2005] using the instrument ISUAL on board the FORMOSAT-2 satellite. For the first delayed sprite event, we found an altitude for the early stage of the sprite higher than that reported by *Kuo et al.* [2005] through images of the whole events. The second event is trickier for the analysis as ISUAL camera revealed that it is composed by at least two sprites.

This work points out the possibility to estimate the altitude and the electric field for each sample recorded by a spectrophotometer instrument. However, the method is based on streamers that are much simpler than a carrot sprite, hence reaching the limit of the method reported here for complex fully developed complex structures. Nevertheless, the question could be discussed with ASIM measurements because its spectrophotometers (MMIA) have a sampling frequency of 100 kHz (in comparison, ISUAL has a sampling frequency of 10 kHz while JEM-GLIMS and TARANIS have a sampling frequency of 20 kHz). The calculation of the expansion factor could then show more details.

In this chapter, using real data from photometers on board spacecraft, we also show that the growth rate of streamers can be used to estimate the ambient electric field in which the streamer is propagating as proposed by *Kosar et al.* [2012]. This method offers a new way to investigate the environment in which the streamer is initiated, grows, and decay from photometric measurements. However, we also note that this approach need

to be investigated further results seem to suggest that the characteristic radial size of the seed triggering the sprite streamers could play a significant role. We also showed the influence of varying air density on the determination of the altitude and the peak electric field affects mainly the peak electric over which a larger uncertainty occurs. However, the altitude does not change. The application of the method developed in this chapter in varying air density is the next challenge.

Another interesting point is the importance to have the possibility to observe the $1\,NN_2{}^+$ band system. ISUAL and GLIMS both had a photometer dedicated to such observations while ASIM and TARANIS do not. However, if the use of the ratio $\frac{\mathrm{LBH}}{1\mathrm{NN}_2^+}$ gives more accurate results, the ratio $\frac{2\mathrm{PN}_2}{1\mathrm{PN}_2}$ still gives acceptable results.

In addition, we also highlight the fact that $\frac{\mathrm{LBH}}{1\mathrm{PN}_2}$ can be used with photometric data coming from space instruments despite the claimed impossibility reported by [*Pérez-Invernón et al.*, 2020] due to a cascading process (excited $\mathrm{N}_2(\mathrm{w}^1\Delta_\mathrm{u}, \nu) \rightarrow \mathrm{N}_2(\mathrm{a}^1\Pi_\mathrm{g}, \nu = 0)$) breaking the assumption of a constant vibrational distribution function of the $\mathrm{N}_2(\mathrm{a}^1\Pi_\mathrm{g}, \nu = 0)$ levels required to calculate the contribution of LBH into the photometer band and to estimate the altitude of the streamer head [*Pérez-Invernón et al.*, 2018].

V Physics of long streamers in variable air density

V.1 Introduction

Numerical simulations of sprite streamers are usually realized over small distances on the order of a few hundreds of meters [e.g., *Pasko et al.*, 1997; *Liu and Pasko*, 2004; *Bourdon et al.*, 2007; *Qin et al.*, 2013b; *Ihaddadene and Celestin*, 2015; *Shi et al.*, 2017; *Janalizadeh and Pasko*, 2019]. This is explained by the expensive computational costs of long streamers simulations. These costs can be decreased using adaptive mesh refinement (AMR) techniques [e.g., *Montijn et al.*, 2006] or adapting the code to modern computers with shared and distributed memory. The simulation of long streamers is one of the next steps to understand the physics of sprite streamers. *Luque and Ebert* [2010] and *Qin and Pasko* [2015] have simulated streamers over 5 km in varying air density and reported a departure from the similarity laws regarding the electron density and electric field. Note that *Shi et al.* [2017] simulated long streamers of 4.5 cm at ground pressure that is, using similarity laws, around 663 m at 70 km altitude.

In this chapter, we report our results regarding the evolution of the electron density, and the electric field for a streamer with a 15-km length starting at 80 km and propagating downward.

We then study the impact of the varying air density on the spectroscopic ratio as a function of different ambient reduced electric fields for 5-km long streamers, starting at 80 km and propagating downward and we study the impact of the size of the inhomogeneity on the growth rate of the streamer in constant air density.

The results presented in this chapter open a pathway to improve spectroscopic diagnostics for expanding sprite streamers propagating over several scale heights. Their analysis leads to constraints on the choice of pairs of spectroscopic ratios and the corresponding expected altitude resolution, as well as intrinsic uncertainties associated with those methods.

V.2 Method

We simulate a positive streamer starting at 80 km altitude and moving downward to 65 km altitude following *Qin and Pasko* [2015], the mesh resolution is of 2.08 m for the r and z directions and the numerical grid is made of 800×7212 points thus corresponding to a physical domain of 1.6 km $\times$ 15 km. The streamer is initialized from a neutral Gaussian seed (see equation (98)) with a characteristic size of $\sigma = 139$ m. The ambient electric field is set to a value of 1 E_k, with $E_k = 30 \frac{N}{N_0}$ kV cm^{-1} the local breakdown electric field. The ionospheric electron background profile defined in equation (96) (see Section II.9.2) is applied, and the calculation of the photoionization process is not included.

We need to have an analytic expression of the air density with altitudes. In this aim, we use the US Standard Atmosphere [*Oliver*, 1987]. We fit it with the exponential function $a \exp(bx)$ as illustrated in Figure 55. The coefficient of determination R^2 is 0.9964. The coefficient $a = 2.95 \times 10^{19}$ cm^{-3} and the coefficient $b = \frac{1}{H} = 0.1428$ km^{-1} (where H is the atmosphere scale height equal to 7 km) leading to express the air density N as a function of the altitude h as:

$$N(h) = 2.95\,10^{19} \exp(-0.1428h) \tag{112}$$

The equation (112) can be used to estimate the relationship between physical quantities and air density to evaluate the difference with the similarity laws (see Chapter I).

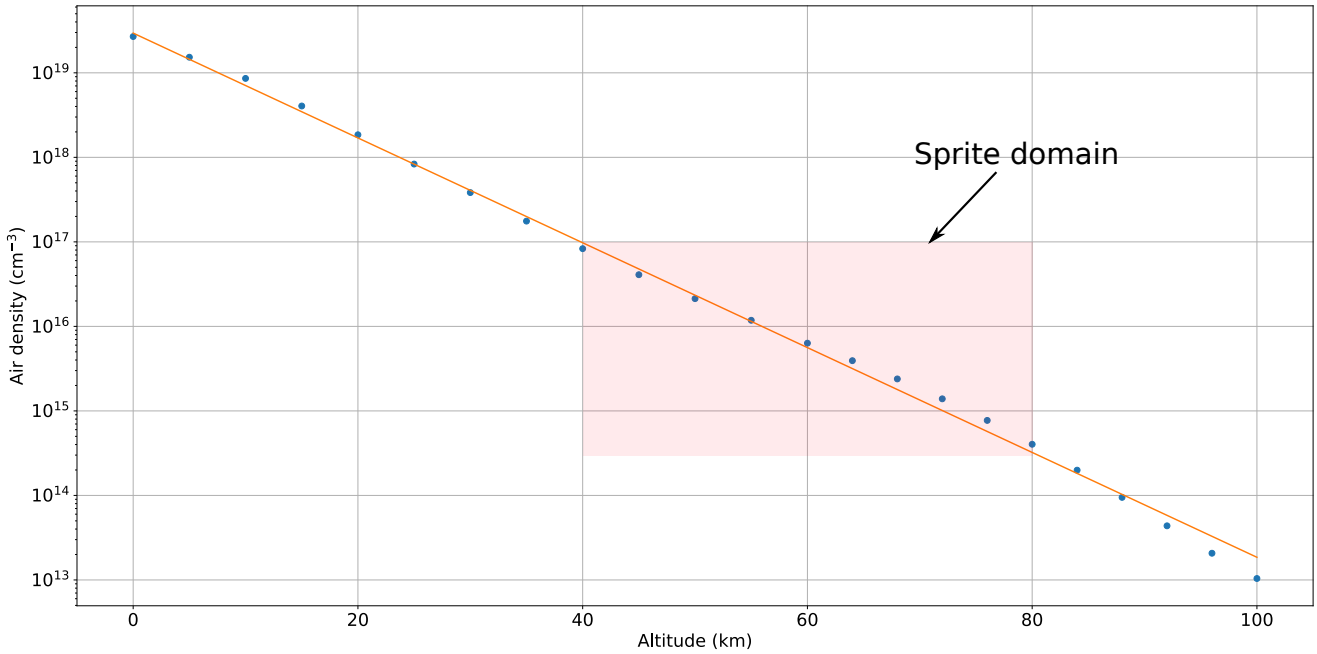

Figure 55: Illustration of the fit (orange line) of the air density from the US Standard Atmosphere (blue points). The pink rectangle shows the sprite domain spreading over ∼3 decades of air density.

V.3 Results and discussions

V.3.1 Effects on the electron density

Figure 56 shows a cross-sectional view of the electron density for a positive streamer at four different times over a propagation of about 15 km.

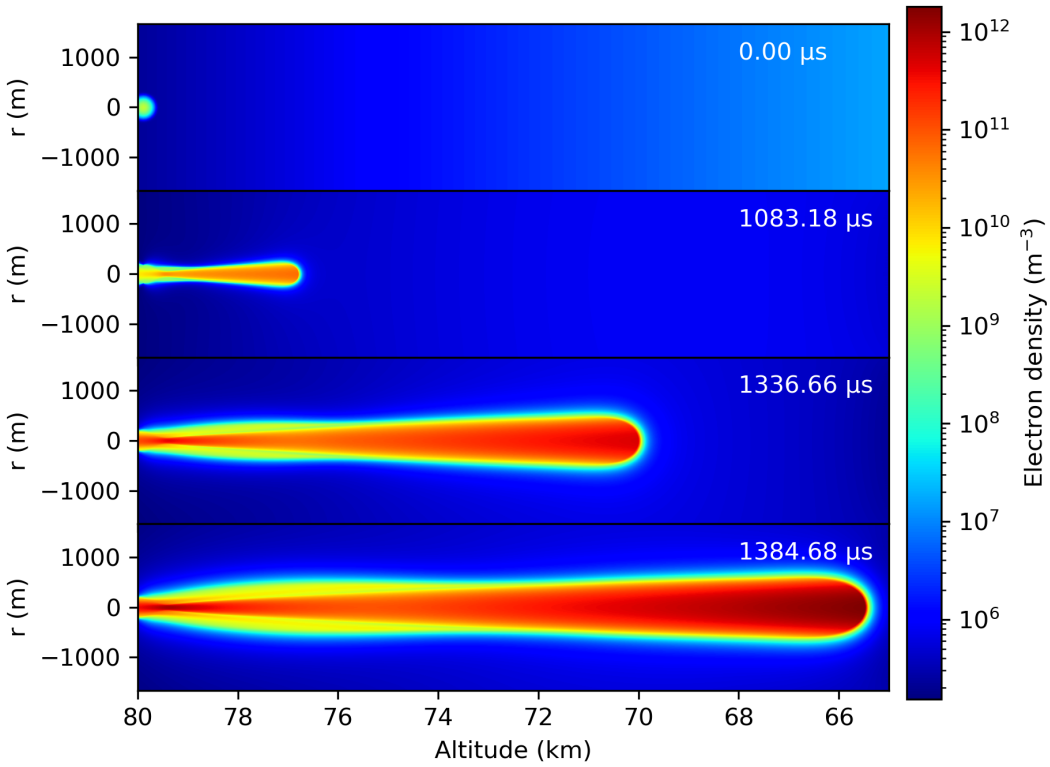

Figure 56: Four 2-D cross-sectional views of the electron density at four different times indicated in the top-right corner for a positive streamer propagating from 80 km to 65 km under a constant reduced electric field of 1 E_k.

Figure 57 shows the maximum of the electron density as a function of the altitude for the positive streamer shown in Figure 56 once its propagation started from 1000 µs. The maximum of the electron density as a function of the altitude is well fitted with an exponential law with a characteristic length of ∼3.39 km.

We estimate the exponent k in $\left(\frac{N}{N_0}\right)^k$ from the previous fit to evaluate the departure

from the similarity laws to be $k = \frac{7\,\mathrm{km}}{3.39\,\mathrm{km}} \simeq 2.06$.

This value is consistent with the similarity law of the electron density predicted to scale as $\left(\frac{N}{N_0}\right)^2$. Although *Qin and Pasko* [2015] found the same value for a linear varying electric field, for constant reduced electric field of $0.8E_k$ they reported an exponent $k = 2.4$. This difference can be explained by the difference between the ambient electric fields used. For instance, *Qin and Pasko* [2015] reported different exponents of $\frac{N}{N_0}$ for the maximum of the electron density for a streamer propagating downward in different electric fields.

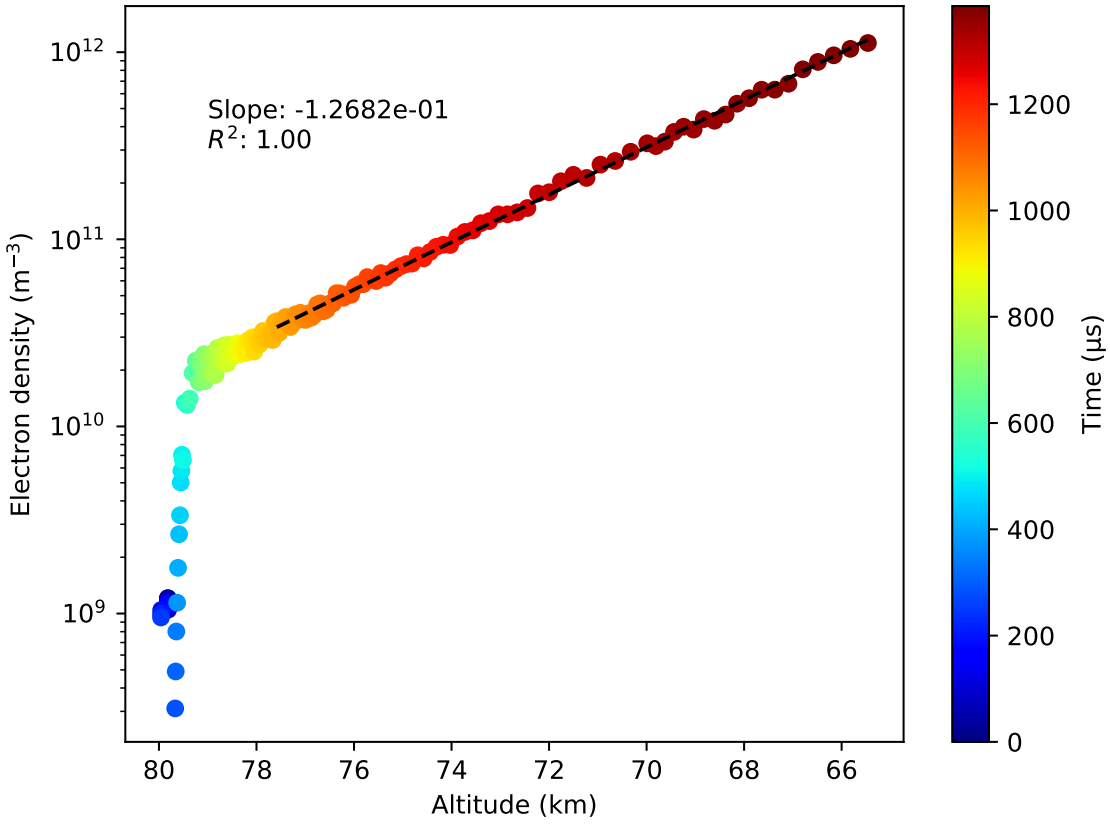

Figure 57: Maximum of the electron density along the vertical axis for the positive streamer illustrated in Figure 56. The maximum of the electron density used for the fit is taken once the streamer propagates ($t > 1000\,\mu s$), and its temporal evolution is reported in the associated colorbar. The dashed black line corresponds to a linear fit of the discrete set of points. The coefficient of determination R^2 as well as the slope are given at the top-left corner.

V.3.2 Effects on the electric field

Figure 58 shows the electric field of the positive streamer at different times over the 15-km propagation. The increase of the electric field is the result of the increase of the

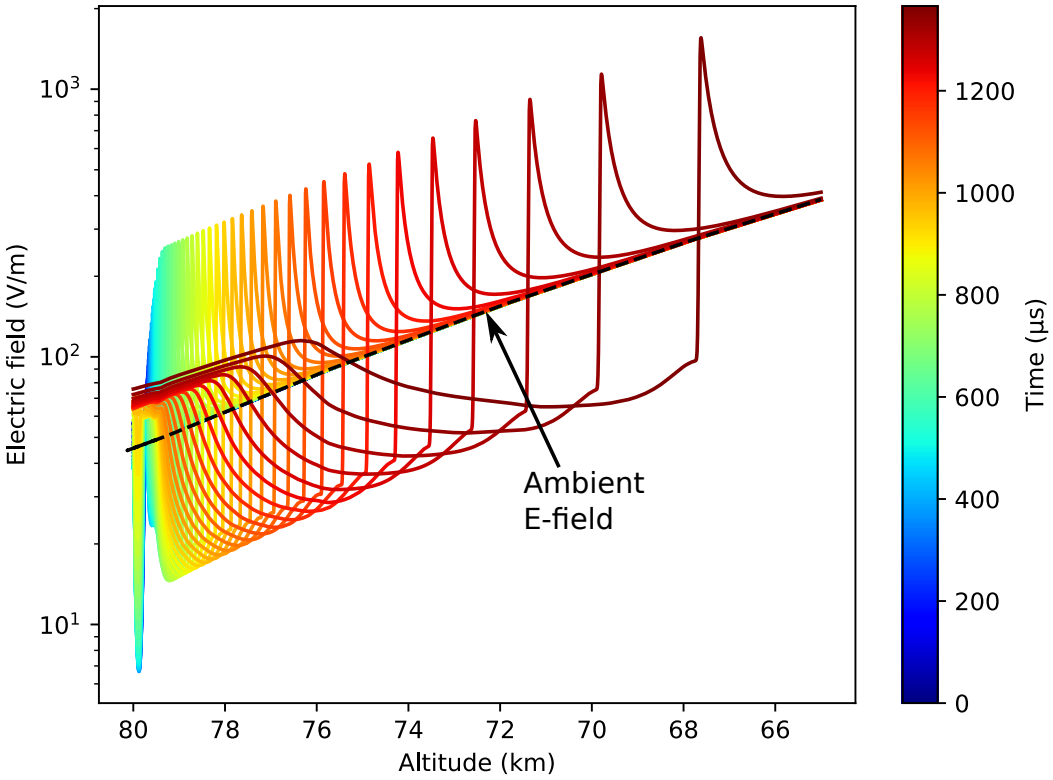

Figure 58: Evolution of the electric field along the altitude for the positive streamer illustrated in Figure 56. The colorbar indicates the time associated with the positive streamer propagation. The dashed black curve shows the ambient electric field in which the streamer propagates.

air density as long as the streamer propagates downward. It contrasts with a streamer propagating in an atmosphere with constant density along the altitude. In such a case, the peak electric field is constant (see Figure 17). As the streamer propagates downward, the peak electric field for a given altitude is never reached leading to a continuous increase of the electric field.

Figure 59 illustrates the evolution of the peak electric field as a function of the altitude. We fit it with an exponential function in the growth phase to evaluate the power-law relation in $\frac{N}{N_0}$ as we did in the previous section. We found an exponent of

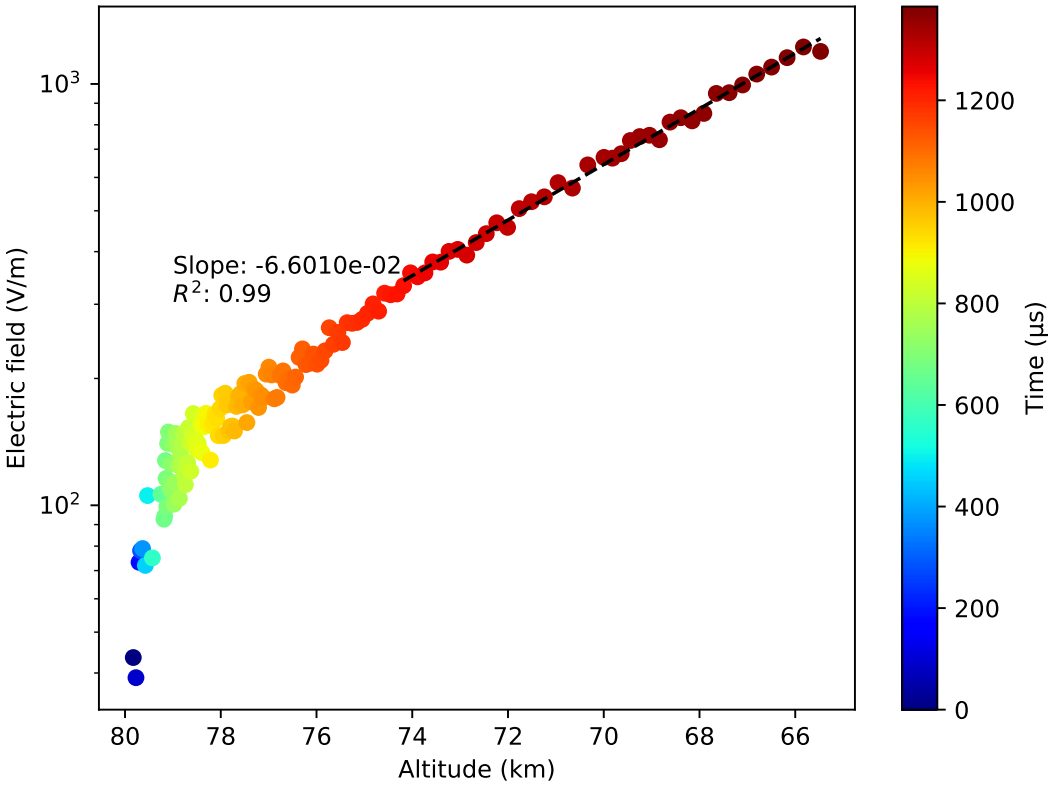

Figure 59: Peak electric field as a function of the altitude for the positive streamer illustrated in Figure 56. The time associated with the peak electric field is reported in the colorbar. The dashed black line corresponds to a linear fit of the discrete set of points. The coefficient of determination R^2 as well as the slope are given in vicinity of the dashed black line.

$k\sim$ 1.1, which is close to 1. As with the maximum of the electron density, we find that under an external reduced field of 1 E_k, the result is consistent with the similarity law of the electric field as it scales as $\left(\frac{N}{N_0}\right)$.

V.4 Effects on the spectroscopic ratios

As reported in the two previous sections, we note that the electron density and the peak electric field are not constant when a streamer propagates in varying air density (see Figure 57 and Figure 59). The density of excited species $N_2(a^1\Pi_g)$, $N_2(B^3\Pi_g)$, $N_2(C^3\Pi_u)$, and $N_2^+(B^2\Sigma_u^+)$ is expected to vary as $\left(\frac{N}{N_0}\right)^2$ because it is mainly affected by the electron density and the excitation frequency (see equation (91) and Section II.6), which is affected by the streamer electric field.

To study the impact of varying air density of spectroscopic emissions, we conduct three identical simulations consisting of the positive streamer propagation in a similar setup as the one described in the section V.2, except that we use three different reduced ambient electric fields $0.8E_k$, $1E_k$, and $1.2E_k$ extending over 5 km. The figure 60 shows the ratio $\frac{\mathrm{LBH}}{1\mathrm{PN}_2}$ as a function of $\frac{2\mathrm{PN}_2}{1\mathrm{PN}_2}$.

Considering the ratio $\frac{\mathrm{LBH}}{1\mathrm{PN}_2}$ given for a reduced ambient electric field of $0.8E_k$, we identify two parts. The first one is the plateau for the ratio $\frac{\mathrm{LBH}}{1\mathrm{PN}_2}$ from 78.5 km to 77 km altitude, then followed by its decrease. For stronger reduced ambient electric fields (i.e., $1E_k$ and $1.2E_k$), we only found one part corresponding to a decrease of the $\frac{\mathrm{LBH}}{1\mathrm{PN}_2}$ as the altitude decreases. Note that for the two reduced ambient electric fields of $0.8E_k$ and $1E_k$, we do not consider the increasing of the ratio in the first kilometers (i.e., up to $\sim$78.5 km) of the streamer because it has not been completely formed yet.

For the sake of comparison with the propagation of streamers in similar conditions of ambient electric fields or plasma seed size but in constant air density corresponding to an altitude of 80 km, the evolution of the ratio $\frac{2\mathrm{PN}_2}{1\mathrm{PN}_2}$ as a function of $\frac{\mathrm{LBH}}{1\mathrm{PN}_2}$ is shown in Figure 61.

For a reduced ambient electric field $0.8E_k$ we observe that the ratios $\frac{\mathrm{LBH}}{1\mathrm{PN}_2}$ and $\frac{2\mathrm{PN}_2}{1\mathrm{PN}_2}$ grow as the altitude decreases. We also found a similar shape of the curve as described above with a growing part between 79 km and 78.5 km altitude followed by a plateau around 78.5 km altitude and then an increase part from 78 km altitude. For a reduced

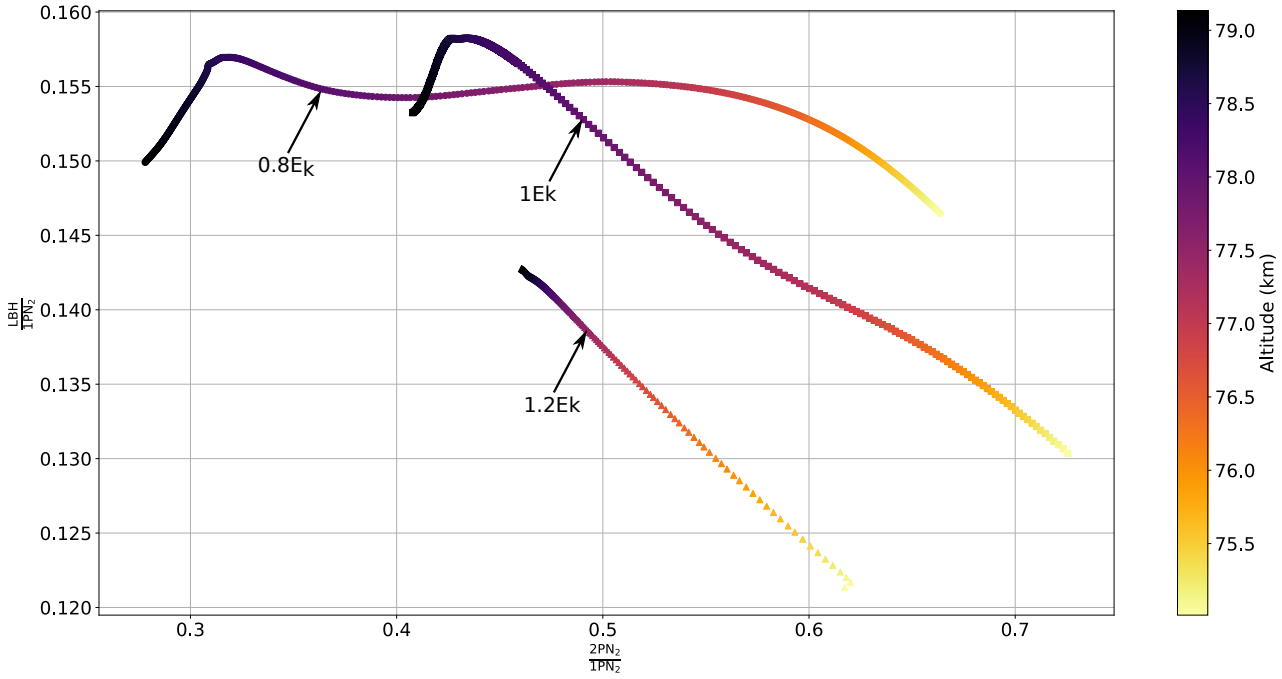

Figure 60: Evolution of the ratio $\frac{2\mathrm{PN}_2}{1\mathrm{PN}_2}$ as a function of $\frac{\mathrm{LBH}}{1\mathrm{PN}_2}$ in varying air density for a reduced ambient electric field of $0.8E_k$(disk), $1E_k$ (square), and $1.2E_k$ (triangle). The altitude of the streamer defined as the position of the peak electric field is reported in the colorbar. Note that, the early initialization stage of the three streamers are removed.

ambient electric field of $1E_k$, the behavior of both ratios $\frac{\mathrm{LBH}}{1\mathrm{PN}_2}$ and $\frac{2\mathrm{PN}_2}{1\mathrm{PN}_2}$ is similar to the case in varying air density immersed in a reduced ambient electric field of $1.2E_k$. Finally, for the reduced ambient electric field of $1.2E_k$, the variation for both ratios is very weak, and it stays almost constant with an average ratio of 0.165 for $\frac{\mathrm{LBH}}{1\mathrm{PN}_2}$, and 0.43 for $\frac{2\mathrm{PN}_2}{1\mathrm{PN}_2}$. However, the variation range for these ratios in constant air density is significantly different. Indeed, in varying air density the ratio $\frac{\mathrm{LBH}}{1\mathrm{PN}_2}$ varies between 0.12 and 0.16 (Figure 60) while in constant air density its variation is between 0.162 and 0.174 (Figure 61), which is practically constant. On the other hand, in varying air density the ratio $\frac{2\mathrm{PN}_2}{1\mathrm{PN}_2}$ is between 0.3 and 0.7 (Figure 60) and it starts at 0.25 and finishes at 0.55 in constant air density (Figure 61).

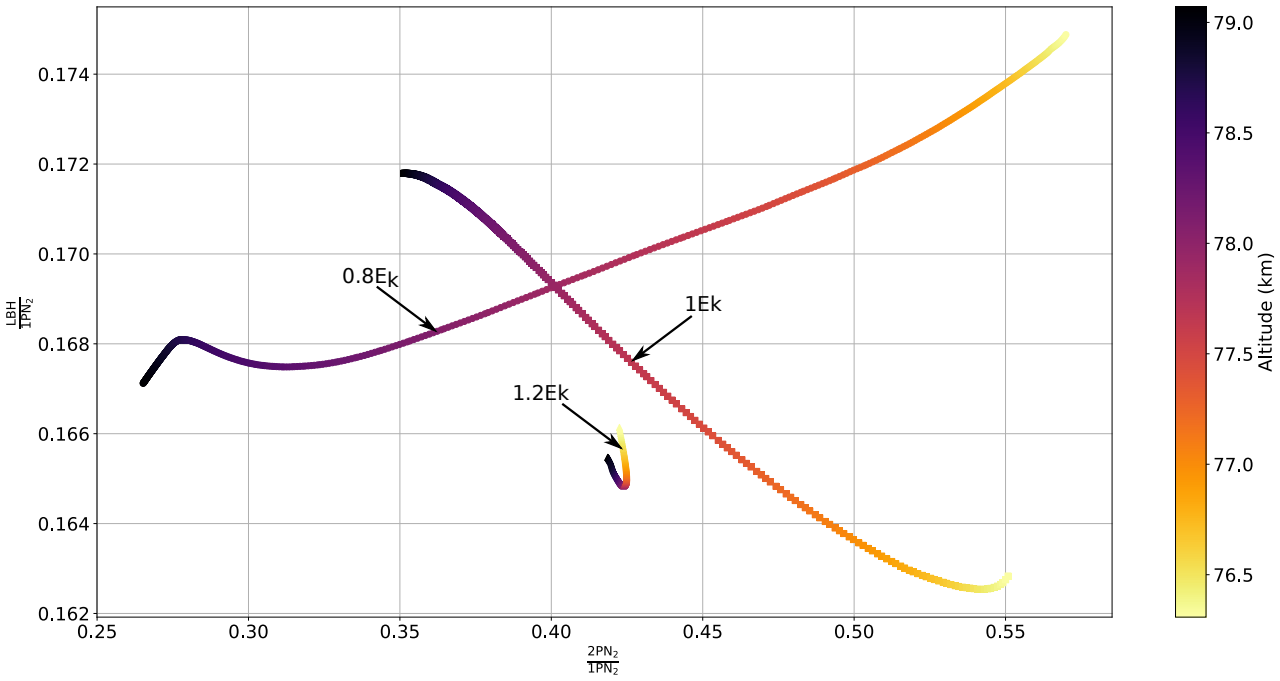

Figure 61: Evolution of the ratio $\frac{2\mathrm{PN}_2}{1\mathrm{PN}_2}$ as a function of $\frac{\mathrm{LBH}}{1\mathrm{PN}_2}$ in constant air density for a reduced ambient electric field of $0.8E_k$(disk), $1E_k$ (square), and $1.2E_k$ (triangle). The altitude of the streamer is defined as the position of the peak electric field is reported in the colorbar. Note that the early initialization stage of the three streamers are removed.

In order to evaluate the influence of the varying air density on ratio, we compare the relative amplitude variation defined as:

$$\Delta V_r = 100 \left| \frac{\max(r) - \min(r)}{\min(r)} \right| \tag{113}$$

where r is the ratio (e.g., $\frac{\mathrm{LBH}}{1\mathrm{PN}_2}$) for case in constant air density and varying air density.

We conduct this analysis for the ratio $\frac{\mathrm{LBH}}{1\mathrm{PN}_2}$ and results are summarized in the Table 8. As shown in this table, the relative amplitude variation for the case regarding the constant air density is between $\sim$0.6 % and $\sim$5 %, while for the varying air density it is between $\sim$7 % and $\sim$21 % showing that the reduced ambient electric field in varying air density has a stronger impact than the constant air density where spectroscopic ratios

E_k	0.8	1	1.2
$\Delta V_{\texttt{varying density}}$ (%)	∼7	∼21	∼18
$\Delta V_{\texttt{constant density}}$ (%)	∼5	∼5	∼0.6

Table 8: Relative amplitude variation for the ratio $\frac{\text{LBH}}{1\text{PN}_2}$ calculated for the three reduced ambient electric field $0.8E_k$, $1E_k$, and $1.2E_k$ from Figure 60 and Figure 61.

are nearly constant. We expect the results to be converged in the case of the constant air density. One can consider it to be the case as $\Delta V_r \leq 5\,\%$. But in varying air density, the distance over which ΔV_r is calculated is arbitrary and the ratios will continue to vary.

From this section, we conclude that for a practical application of the method proposed by [*Ihaddadene and Celestin*, 2017] discussed in Chapter IV to recover the altitude of sprite streamer heads, in the worst case, ratios used from an altitude to the next should vary by more than ∼20 % to reach an altitude resolution of 15 km.

V.5 Influence of the seed radius

Another parameter that could affect spectrophotometric diagnostics is the size of the inhomogeneity from which the streamer ignites. In particular, it is usually estimated that the growth rate only depends on the ambient electric field. However, in this section, we show that the growth rate also depends on the size of the initial inhomogeneity. It is an important point to consider in the use of irradiance-ratios-based spectroscopic techniques, as those depend on the streamer growth rate [*Ihaddadene and Celestin*, 2017].

In simulations, the triggering of streamers from a Gaussian inhomogeneity can be realized either with a spherical electrode [*Liu and Pasko*, 2006] or without [e.g., *Qin and Pasko*, 2015]. Note that for example *Kosar et al.* [2012] initiates positive and negative streamers in a weak electric field from an elongated plasma inhomogeneity without spherical electrode.

Kosar et al. [2012] have studied the impact of the ambient electric field on the growth rate of streamers. They show an increase of the growth rate as the electric field becomes stronger and suggest that the ambient electric field could be estimated from this growth rate.

In this section, we investigate the impact of the characteristic size of the globally neutral Gaussian inhomogeneity over the growth rate under a constant electric field. In addition, the air density is set constant. We propagate three positive streamers under an ambient electric field of $1E_k$ over 5 km at an altitude of 80 km. The characteristic sizes σ (see equation (98)) of the initial inhomogeneity used are 190 m, 285 m (i.e., 1.5 times bigger), and 570 m (i.e., 2 times bigger).

Figure 62 shows the distance travelled by the three positive streamers initialized with a different characteristic size of the Gaussian inhomogeneity.

The use of an exponential allows us to estimate the growth rate of the streamer throughout its expansion stage [*Kosar et al.*, 2012]. However it is important to point out

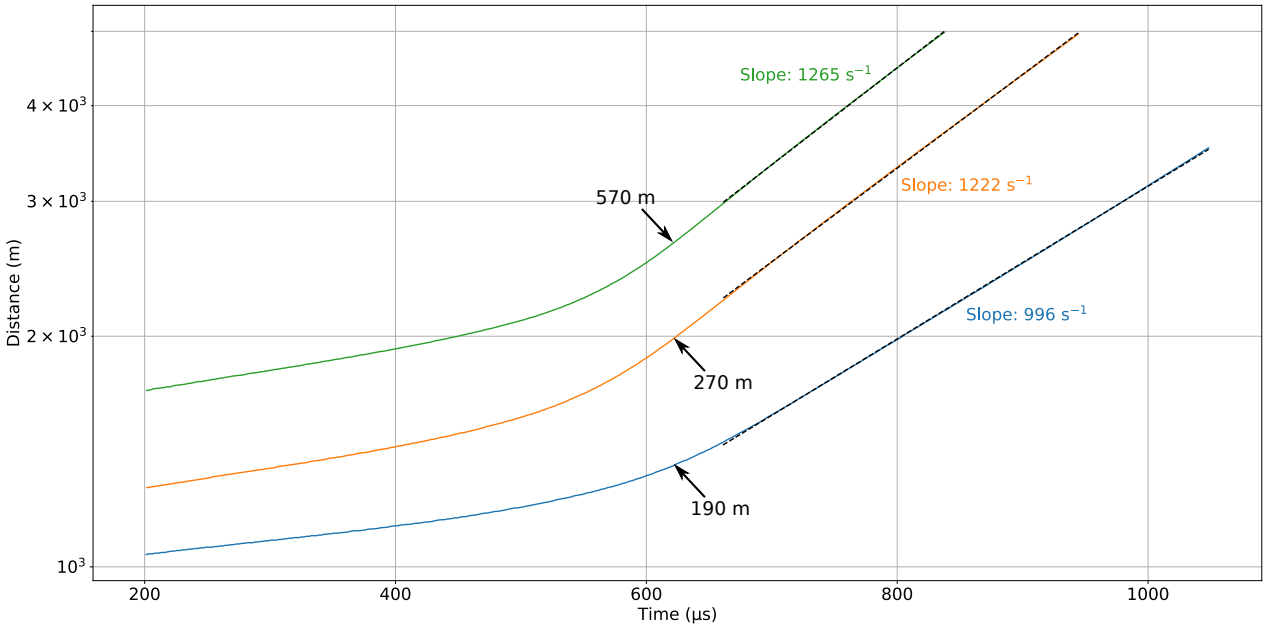

Figure 62: Distance travelled by three positive streamers at 80 km altitude over 5 km as a function of time in constant air density. The ambient electric field is $1E_k$. The characteristic size used for the Gaussian inhomogeneity is reported by the three black arrows. The three dashed black lines correspond to the linear fit for each streamer during their expansion stage. The estimated growth rates (for speed) corresponding to the slope are reported in the vicinity of each curve.

that the definition of the growth rate ν_e has two definitions. Indeed, it can be defined with respect to speed or brightness. The relationship between the two is a factor of 3 *Kosar et al.* [2012]. A comparison of the growth rate (for brightness) in this study with those reported by *Ihaddadene and Celestin* [2017] points out the fact that the values founded are consistent. Indeed, for a streamer at an altitude of 80 km under an ambient electric field of 28 $\frac{N}{N_0}$ kV cm^{-1} with a Gaussian inhomogeneity size of 10^{-4} $\frac{N}{N_0}$ m (i.e., 6.67 m at 80 km altitude), they found an irradiance growth rate of 7.75×10^3 s^{-1} (Table 4 in their paper) while (see Section IV.2) we found an irradiance growth rate of 6884 s^{-1} for the smallest Gaussian inhomogeneity size of 10^{-4} $\frac{N_0}{N}$ m ($\sigma = 190$ m, blue curve in Figure 62). For the biggest one ($\sigma = 570$ m, green curve in Figure 62) we found a growth

Radius size (m)	Growth rate (s^{-1})
190	2295
285	2814
570	2914

Table 9: Growth rate as a function of the initial Gaussian inhomogeneity size for the three positive streamers immersed in an ambient electric field of $1E_k$.

rate of $8743\,s^{-1}$.

However, we were not able to simulate a streamer with a Gaussian inhomogeneity size of 6.67 m (after scaling at 80 km altitude) as the one used by *Ihaddadene and Celestin* [2017] presumably because we do not use a spherical electrode. The use of a such electrode allows to create strong electric fields (several times the breakdown threshold field), and therefore can propagate streamers associated with small inhomogeneities (see [*Qin and Pasko*, 2014]). From the smallest seed used to the largest, we observe a relative variation of the growth rate of 26 %.

Table 9 shows the evolution of the growth rate as a function of the characteristic size σ coming from the three positive streamers reported in Figure 62.

We see in this figure that the growth rate has dependence on the inhomogeneity size. Therefore, the growth rate depends on both the ambient electric field [*Kosar et al.*, 2012] and the inhomogeneity size. However, further investigations are required to properly define the trend that is suggested by Table 9. Indeed, these three points are not sufficient to conclude if the growth rate increases as long as the characteristic size of the inhomogeneity increases or if it can reach a limit. Nevertheless, we reported that we failed to trigger a positive streamer with a Gaussian inhomogeneity size of 95 m. Concerning the peak electric field of $200\,V\,m^{-1}$ in the streamer head, we did not notice any significant variation as function of the characteristic size leading to think that the latter is mostly driven by the ambient electric field.

V.6 Conclusion

In this chapter we reported our results concerning the propagation of long streamer (i.e., from 5 km to 15 km) in varying air density obtained using the efficient streamer model developed in the course of the PhD research.

We reported an increase of the electric field and electron density as long as the positive streamer propagates downward. The electric field and electron density variation seem to follow similarity laws for each ambient electric field of $1E_k$.

We also studied the impact of these two parameters with the production of excited species used for spectrophotometric diagnostics. A comparison with a streamer in varying air density and constant air density reveals that the air density gradient has a significant impact on the ratio $\frac{\mathrm{LBH}}{1\mathrm{PN}_2}$, which is used to determine the altitude and the electric field of the peak electric field of a streamer.

In the course of our investigation, we have found out that the growth rate of expanding positive streamers depends on the characteristic sizes of the Gaussian inhomogeneity used to trigger them. We note that the Gaussian inhomogeneity plays two roles. First, there is a minimum size required to trigger a positive streamer. Second, for a given ambient electric field, the growth rate is increasing as the inhomogeneity size grows in a manner that is not negligible. These two observations made from numerical simulations highlight the fact that the inhomogeneity size used for triggering streamers has an influence on the expansion of the streamer as the ambient electric field does. However, the impact on the peak electric field in the streamer head seems negligible. The expansion growth rate itself has a direct effect on the dependence of spectroscopic ratios on the electric field. The results obtained in this chapter help constrain and improve the use of spectrophotometric methods used to measure the electric field and altitude of sprite streamer heads.

VI Conclusion

During this thesis, we developed a 3-D axisymetric streamer code capable of simulating their propagation through solving Poisson's equation, the drift-diffusion equation, and the three-group SP_3 for photoionization process. In addition, we compute spectroscopic emissions associated with four spectroscopic species $N_2(a^1\Pi_g)$, $N_2(B^3\Pi_g)$, $N_2(C^3\Pi_u)$, and $N_2^+(B^2\Sigma_u^+)$. We also include Uman's antenna model to compute the magnetic field radiated by streamers. Furthermore, the code is optimized for modern CPU architectures and it is able to take advantage of shared memory parallel computing. Poisson's equation and the three-group SP_3 are both severe bottlenecks for the computation, and they have been ported on GPUs in order to exploit their intrinsic massive parallel capability.

This model has been used to simulate the radio emission associated with the head-on collision of streamers. We calculated the spectral density for different altitudes and have shown that the electric antenna on-board TARANIS should be able to detect sprite streamer collisions. Although our approach neglects the role of the ionospheric filtering, the behavior of the ionosphere above a thunderstorm is quite complex, allowing the possibility for signals with a frequency below the ionospheric plasma frequency to pass through the ionosphere and reach near-Earth space.

We also developed a spectrophotometric diagnostic to infer the altitude and the electric field of sprite streamers from optical data. The method is based on the ratio method developed by *Ihaddadene and Celestin* [2017]. It consists in creating a parameter space for altitude and electric field for a given growth rate deduced from photometric measurements. Using this parameter space, it is possible to report the ratios obtained through spectrophotometric measurements and obtain a set of altitudes and electric fields. The use of two different ratios allows to estimate the altitude as the intersection between two sets of points. Then, the electric field is inferred through the estimated altitude. We also investigate limitations of the spectrophotometric method through

the study of streamer propagation over several scale heights and the dependence of the exponential expansion characteristic rate on the size of the initial inhomogeneity.

Indeed, the performance of our code gave us the opportunity to simulate long streamers (i.e., 5 km of length) and up to 15 km in less than 3 weeks of computation offering the possibility to explore the behavior of the electron density, electric field, and spectrophotometric ratios. We found that the electron density and the electric field are always increasing as the streamer propagates downward in a constant reduced electric field, and that the spectroscopic ratio $\frac{\mathrm{LBH}}{1\mathrm{PN}_2}$ is significantly affected by the varying air density. Simulations of streamers of 5-km length with different inhomogeneity sizes reveal that under an identical reduced electric field, the growth rate of the streamer is significantly affected. We also notice that it does not influence the peak electric field.

Suggestion for future work:

Streamer code In this thesis, Poisson's equation and the three-group SP_3 were solved on large numerical grids. It is interesting to study the use of direct solvers instead of iterative solvers. Moreover, the use of a direct solver on GPUs is well documented in the literature.

Radio emission The work about the electromagnetic emission produced by head-on collisions between two streamers having opposite polarities could be extended in taking the ionosphere filtering into account. One should also study the effect of the varying air density on the collision of streamers. Indeed, streamers propagating downward will meet a stronger density while streamers propagating upward will meet a lower one. As we observed that has an effect on the electric field, which will not be constant and thus could produce a collision between two streamers having a significant asymmetry with respect to their own electric field. Finally, the conducted study does not investigate how the radio signal will be affected by the superposition of a large quantity of incoherent streamer collisions.

Spectroscopic diagnostic The work about spectroscopic diagnostic can be extended in adding the effect of the inhomogeneity size of the seed in the study, and thus could offer a possibility to estimate its size from spectrophotometric measurements. Another step forward we will be to add the varying air density into the model as this one affects also spectroscopic ratios.

Long streamers Because it is mainly an exploratory work, it will be nice to keep up. One should focus on the influence of a changing halo electric field on the propagation of long streamers in varying air density in order to be closer of what happens in the ionosphere. One should also investigate the possibility to simulate long streamers to observe streamer branching, and thus may explain the role plays by the photoionization length on streamer branching.

References

Adachi, T., H. Fukunishi, Y. Takahashi, Y. Hiraki, R.-R. Hsu, H.-T. Su, A. B. Chen, S. B. Mende, H. U. Frey, and L. C. Lee (2006), Electric field transition between the diffuse and streamer regions of sprites estimated from ISUAL/array photometer measurements, *Geophysical Research Letters*, *33*, L17,803.

Adachi, T., Y. Hiraki, K. Yamamoto, Y. Takahashi, H. Fukunishi, R.-R. Hsu, H.-T. Su, A. B. Chen, S. B. Mende, H. U. Frey, and L. C. Lee (2008), Electric fields and electron energies in sprites and temporal evolutions of lightning charge moment, *Journal of Physics D: Applied Physics*, *41*(23), 234,010.

Adachi, T., M. Sato, T. Ushio, A. Yamazaki, M. Suzuki, M. Kikuchi, Y. Takahashi, U. S. Inan, I. Linscott, Y. Hobara, H. U. Frey, S. B. Mende, A. B. Chen, R.-R. Hsu, and K. Kusunoki (2016), Identifying the occurrence of lightning and transient luminous events by nadir spectrophotometric observation, *Journal of Atmospheric and Solar-Terrestrial Physics*, *145*, 85 – 97.

Armstrong, R., J. Shorter, M. Taylor, D. Suszcynsky, W. Lyons, and L. Jeong (1998), Photometric measurements in the sprites '95 & '96 campaigns of nitrogen second positive (399.8 nm) and first negative (427.8 nm) emissions, *Journal of Atmospheric and Solar-Terrestrial Physics*, *60*, 787 – 799.

Babich, L., and E. Bochkov (2017), Numerical simulation of electric field enhancement at the contact of positive and negative streamers in relation to the problem of runaway electron generation in lightning and in long laboratory sparks, *Journal of Physics D: Applied Physics*, *50*(45), 455,202.

Blanc, E., and T. Farges (2012), La face cachée des orages, *Pour la Science*, *416*(48).

Blanc, E., T. Farges, R. Roche, D. Brebion, T. Hua, A. Labarthe, and V. Melnikov

(2004), Nadir observations of sprites from the International Space Station, *Journal of Geophysical Research: Space Physics*, *109*(A02306).

Bonaventura, Z., A. Bourdon, S. Celestin, and V. P. Pasko (2011), Electric field determination in streamer discharges in air at atmospheric pressure, *Plasma Sources Science and Technology*, *20*(3), 035,012.

Boris, J. P., and D. L. Book (1973), Flux-corrected transport. i. shasta, a fluid transport algorithm that works, *Journal of Computational Physics*, *11*(1), 38 – 69.

Bourdon, A., V. P. Pasko, N. Y. Liu, S. Célestin, P. Ségur, and E. Marode (2007), Efficient models for photoionization produced by non-thermal gas discharges in air based on radiative transfer and the Helmholtz equations, *Plasma Sources Science and Technology*, *16*, 656–678.

Bucsela, E., J. Morrill, M. Heavner, C. Siefring, S. Berg, D. Hampton, D. Moudry, E. Wescott, and D. Sentman (2003), N_2 ($B^3\Pi_g$) and N_2^+($A^2\Pi_u$) vibrational distributions observed in sprites, *Journal of Atmospheric and Solar-Terrestrial Physics*, *65*, 583 – 590.

Celestin, S., and V. P. Pasko (2010), Effects of spatial non-uniformity of streamer discharges on spectroscopic diagnostics of peak electric fields in transient luminous events, *Geophysical Research Letters*, *37*, L07804.

Chanrion, O., and T. Neubert (2008), A pic-mcc code for simulation of streamer propagation in air, *Journal of Computational Physics*, *227*(15), 7222 – 7245.

Chern, J., R. Hsu, H. Su, S. Mende, H. Fukunishi, Y. Takahashi, and L. Lee (2003), Global survey of upper atmospheric transient luminous events on the rocsat-2 satellite, *Journal of Atmospheric and Solar-Terrestrial Physics*, *65*(5), 647 – 659.

Chern, J.-S., A.-M. Wu, and S.-F. Lin (2014), Globalization extension of transient luminous events from formosat-2 observation, *Acta Astronautica*, *98*, 64 – 70.

Combes, F. (2015), The square kilometer array: cosmology, pulsars and other physics with the SKA, *Journal of Instrumentation*, *10*(09), C09,001–C09,001.

Cummer, S., U. Inan, T. Bell, and C. Barrington-Leigh (1998), ELF radiation produced by electrical currents in sprites, *Geophysical Research Letters*, *25*, 1281–1284.

Cummer, S., N. Jaugey, J. Li, W. Lyons, T. Nelson, and E. Gerken (2006a), Submillisecond imaging of sprite development and structure, *Geophysical Research Letters*, *33*.

Cummer, S. A., H. U. Frey, S. B. Mende, R. Hsu, H. Su, A. B. Chen, H. Fukunishi, and Y. Takahashi (2006b), Simultaneous radio and satellite optical measurements of high-altitude sprite current and lightning continuing current, *Journal of Geophysical Research: Space Physics (1978–2012)*, *111*(A10315).

Davies, K. (1989), *Ionospheric radio*, P. Peregrinus, London.

DLMF (2019), *NIST Digital Library of Mathematical Functions*, http://dlmf.nist.gov/, Release 1.0.24 of 2019-09-15, f. W. J. Olver, A. B. Olde Daalhuis, D. W. Lozier, B. I. Schneider, R. F. Boisvert, C. W. Clark, B. R. Miller, B. V. Saunders, H. S. Cohl, and M. A. McClain, eds.

Dwyer, J. R., D. M. Smith, and S. A. Cummer (2012), High-Energy Atmospheric Physics: Terrestrial Gamma-Ray Flashes and Related Phenomena, *Space Science Reviews*, *173*, 133–196.

Ebert, U., C. Montijn, T. Briels, W. Hundsdorfer, B. Meulenbroek, A. Rocco, and E. Veldhuizen (2006), The multiscale nature of streamers, *Plasma Sources Science and Technology*, *15*, S118.

Evans, D. (1984), Parallel s.o.r. iterative methods, *Parallel Computing*, *1*(1), 3 – 18.

Farges, T., and E. Blanc (2010), Characteristics of infrasound from lightning and sprites near thunderstorm areas, *Journal of Geophysical Research: Space Physics*, *115*, A00E31.

Farges, T., and E. Blanc (2011), Lightning and tle electric fields and their impact on the ionosphere, *Comptes Rendus Physique*, *12*(2), 171 – 179.

Farges, T., and E. Blanc (2016), Characteristics of lightning, sprites and human-induced emissions observed by nadir-viewing cameras on board the international space station, *Journal of Geophysical Research: Atmospheres*, *121*, 3405–3420.

Farges, T., P. Hébert, F. Le Mer-Dachard, K. Ravel, and S. Gaillac (2018), Microcameras and photometers (MCP) on board the TARANIS satellite, in *XVI International Conference on Atmospheric Electricity*.

Fishman, G. J., P. N. Bhat, R. Mallozzi, J. M. Horack, T. Koshut, C. Kouveliotou, G. N. Pendleton, C. A. Meegan, R. B. Wilson, and W. S. Paciesas (1994), Discovery of Intense Gamma-Ray Flashes of Atmospheric Origin, *Science*, *264*(5163), 1313–1316.

Franz, R., R. J Nemzek, and J. R Winckler (1990), Television image of a large upward electrical discharge above a thunderstorm system, *Science*, *249*, 48–51.

Frey, H., S. Mende, S. Harris, H. Heetderks, Y. Takahashi, H. Su, B. Chen, H. Fukunishi, Y.-S. Chang, and L. Lee (2016), The imager for sprites and upper atmospheric lightning (ISUAL): Isual, *Journal of Geophysical Research: Space Physics*, pp. 8134–8145.

Füllekrug, M., D. R. Moudry, G. Dawes, and D. D. Sentman (2001), Mesospheric sprite current triangulation, *Journal of Geophysical Research: Atmospheres*, *106*(D17), 20,189–20,194.

Füllekrug, M., R. Roussel-Dupré, E. M. D. Symbalisty, O. Chanrion, A. Odzimek, O. van der Velde, and T. Neubert (2010), Relativistic runaway breakdown in low-frequency radio, *Journal of Geophysical Research: Space Physics*, *115*(A00E09).

Gerken, E. A., U. S. Inan, and C. P. Barrington-Leigh (2000), Telescopic imaging of sprites, *Geophysical Research Letters*, *27*, 2637–2640.

Golub, G. H., and C. F. Van Loan (1996), *Matrix Computations (4rd Ed.)*, Johns Hopkins University Press, Baltimore, Maryland, USA.

Gordillo-Vázquez, F. J., A. Luque, and M. Simek (2011), Spectrum of sprite halos, *Journal of Geophysical Research: Space Physics*, *116*, A09319.

Gordillo-Vázquez, F. J., A. Luque, and M. Simek (2012), Near infrared and ultraviolet spectra of TLEs, *Journal of Geophysical Research: Space Physics*, *117*, A05329.

Gordillo-Vazquez, F. J. (2010), Vibrational kinetics of air plasmas induced by sprites, *Journal of Geophysical Research: Space Physics*, *115*, A00E25.

Green, B. D., M. E. Fraser, W. T. Rawlins, L. Jeong, W. A. M. Blumberg, S. B. Mende, G. R. Swenson, D. L. Hampton, E. M. Wescott, and D. D. Sentman (1996), Molecular excitation in sprites, *Geophysical Research Letters*, *23*, 2161–2164.

Guo, J.-M., and C.-H. J. Wu (1993), Comparisons of multidimensional non-equilibrium and equilibrium fluid and monte carlo models for streamers, *Journal of Physics D: Applied Physics*, *26*(3), 487–492.

Hampton, D. L., M. J. Heavner, E. M. Wescott, and D. D. Sentman (1996), Optical spectral characteristics of sprites, *Geophysical Research Letters*, *23*, 89–92.

Han, F., and S. A. Cummer (2010), Midlatitude nighttime d region ionosphere variability on hourly to monthly time scales, *Journal of Geophysical Research: Space Physics*, *115*(A09329).

Heavner, M. J., J. S. Morrill, C. Siefring, D. D. Sentman, D. R. Moudry, E. M. Wescott, and E. J. Bucsela (2010), Near-ultraviolet and blue spectral observations of sprites in the 320-460 nm region: N_2 (2PG) emissions, *Journal Geophysical Research*, *115*, A00E44.

Ihaddadene, M. A. (2016), Numerical modeling of streamer discharges in preparation of the TARANIS space mission, Theses, Université d'Orléans.

Ihaddadene, M. A., and S. Celestin (2015), Increase of the electric field in head-on collisions between negative and positive streamers, *Geophysical Research Letters*, *42*, 5644–5651.

Ihaddadene, M. A., and S. Celestin (2017), Determination of sprite streamers altitude based on N $_2$ spectroscopic analysis, *Journal of Geophysical Research: Space Physics*, *122*, 1000–1014.

Intel Corporation (2016a), *Intel® 64 and IA-32 Architectures Developer's Manual*, vol. 1.

Intel Corporation (2016b), *Intel® 64 and IA-32 Architectures Developer's Manual*, vol. 2A.

Janalizadeh, R., and V. P. Pasko (2019), A general framework for photoionization calculations applied to nonthermal gas discharges in air, *Plasma Sources Science and Technology*, *28*(10), 105,006.

Janalizadeh, R., and V. P. Pasko (2020), A framework for efficient calculation of photoionization and photodetachment rates with application to the lower ionosphere, *Journal of Geophysical Research: Space Physics*, *125*(7), e2020JA027,979.

Jehl, A., T. Farges, and E. Blanc (2013), Color pictures of sprites from non-dedicated observation on board the international space station, *Journal of Geophysical Research: Space Physics*, *118*(1), 454–461.

Kanmae, T., H. C. Stenbaek-Nielsen, and M. G. McHarg (2007), Altitude resolved sprite spectra with 3 ms temporal resolution, *Geophysical Research Letters*, *34*, L07810.

Kanmae, T., H. C. Stenbaek-Nielsen, M. G. McHarg, and R. K. Haaland (2010), Observation of sprite streamer head's spectra at 10,000 fps, *Journal of Geophysical Research: Space Physics*, *115*, A00E48.

Kosar, B. C., N. Liu, and H. K. Rassoul (2012), Luminosity and propagation characteristics of sprite streamers initiated from small ionospheric disturbances at subbreakdown conditions, *Journal of Geophysical Research: Space Physics*, *117*, A08328.

Kulikovsky, A. (1995), A more accurate scharfetter-gummel algorithm of electron transport for semiconductor and gas discharge simulation, *Journal of Computational Physics*, *119*(1), 149 – 155.

Kuo, C.-L., R. R. Hsu, A. B. Chen, H. T. Su, L. C. Lee, S. B. Mende, H. U. Frey, H. Fukunishi, and Y. Takahashi (2005), Electric fields and electron energies inferred from the isual recorded sprites, *Geophysical Research Letters*, *32*(19).

Kuo, C. L., A. B. Chen, J. K. Chou, L. Y. Tsai, R. R. Hsu, H. T. Su, H. U. Frey, S. B. Mende, Y. Takahashi, and L. C. Lee (2008), Radiative emission and energy deposition in transient luminous events, *Journal of Physics D: Applied Physics*, *41*(23), 234,014.

Köhn, C., O. Chanrion, and T. Neubert (2017), Electron acceleration during streamer collisions in air, *Geophysical Research Letters*, *44*(5), 2604–2613.

Lefeuvre, F., E. Blanc, J.-L. Pinçon, R. Roussel-Dupré, D. Lawrence, J.-A. Sauvaud, J.-L. Rauch, H. de Feraudy, and D. Lagoutte (2008), *TARANIS—A Satellite Project Dedicated to the Physics of TLEs and TGFs*, pp. 301–315, Springer New York.

Liu, N., and V. P. Pasko (2004), Effects of photoionization on propagation and branch-

ing of positive and negative streamers in sprites, *Journal Geophysical Research*, *109*, A04301.

Liu, N., and V. P. Pasko (2005), Molecular nitrogen LBH band system far-UV emissions of sprite streamers, *Geophysical Research Letters*, *32*, L05104.

Liu, N., and V. P. Pasko (2006), Effects of photoionization on similarity properties of streamers at various pressures in air, *Journal of Physics D: Applied Physics*, *39*(2), 327–334.

Liu, N., V. P. Pasko, D. H. Burkhardt, H. U. Frey, S. B. Mende, H.-T. Su, A. B. Chen, R.-R. Hsu, L.-C. Lee, H. Fukunishi, and Y. Takahashi (2006a), Comparison of results from sprite streamer modeling with spectrophotometric measurements by isual instrument on formosat-2 satellite, *Geophysical Research Letters*, *33*(1).

Liu, N., V. P. Pasko, D. H. Burkhardt, H. U. Frey, S. B. Mende, H.-T. Su, A. B. Chen, R.-R. Hsu, L.-C. Lee, H. Fukunishi, and Y. Takahashi (2006b), Comparison of results from sprite streamer modeling with spectrophotometric measurements by ISUAL instrument on FORMOSAT-2 satellite, *Geophysical Research Letters*, *33*, L01101.

Liu, N., S. Célestin, A. Bourdon, V. P. Pasko, P. Ségur, and E. Marode (2007), Application of photoionization models based on radiative transfer and the helmholtz equations to studies of streamers in weak electric fields, *Applied Physics Letters*, *91*(21), 211,501.

Liu, N., V. P. Pasko, H. U. Frey, S. B. Mende, H.-T. Su, A. B. Chen, R.-R. Hsu, and L.-C. Lee (2009a), Assessment of sprite initiating electric fields and quenching altitude of $A^1\Pi_g$ state of N_2 using sprite streamer modeling and ISUAL spectrophotometric measurements, *Journal of Geophysical Research: Space Physics*, *114*, A00E02.

Liu, N., J. R. Dwyer, J. N. Tilles, M. A. Stanley, P. R. Krehbiel, W. Rison, R. G. Brown, and J. G. Wilson (2019), Understanding the radio spectrum of thunderstorm

narrow bipolar events, *Journal of Geophysical Research: Atmospheres*, *124*(17-18), 10,134–10,153.

Liu, N. Y., V. P. Pasko, K. Adams, H. C. Stenbaek-Nielsen, and M. G. McHarg (2009b), Comparison of acceleration, expansion, and brightness of sprite streamers obtained from modeling and high-speed video observations, *Journal of Geophysical Research: Space Physics*, *114*(A00E03).

Luque, A. (2017), Radio frequency electromagnetic radiation from streamer collisions, *Journal of Geophysical Research: Atmospheres*, *122*(19), 10,497–10,509.

Luque, A., and U. Ebert (2010), Sprites in varying air density: Charge conservation, glowing negative trails and changing velocity, *Geophysical Research Letters*, *37*, L060,806.

McHarg, M. G., H. C. Stenbaek-Nielsen, T. Kanmae, and R. K. Haaland (2010), Streamer tip splitting in sprites, *Journal of Geophysical Research: Space Physics*, *115*, A00E53.

Mende, S. B., R. L. Rairden, G. R. Swenson, and W. A. Lyons (1995), Sprite spectra; N_2 1 PG band identification, *Geophysical Research Letters*, *22*, 2633–2636.

Mignone, A. (2014), High-order conservative reconstruction schemes for finite volume methods in cylindrical and spherical coordinates, *Journal of Computational Physics*, *270*, 784 – 814.

Milikh, G., J. A. Valdivia, and K. Papadopoulos (1998), Spectrum of red sprites, *Journal of Atmospheric and Solar-Terrestrial Physics*, *60*, 907–915.

Montijn, C., W. Hundsdorfer, and U. Ebert (2006), An adaptive grid refinement strategy for the simulation of negative streamers, *Journal of Computational Physics*, *219*(2), 801 – 835.

Morrill, J., E. Bucsela, C. Siefring, M. Heavner, S. Berg, D. Moudry, S. Slinker, R. Fernsler, E. Wescott, D. Sentman, and D. Osborne (2002), Electron energy and electric field estimates in sprites derived from ionized and neutral n2 emissions, *Geophysical Research Letters*, *29*(10).

Morrill, J. S., E. J. Bucsela, V. P. Pasko, S. L. Berg, M. J. Heavner, D. R. Moudry, W. M. Benesch, E. M. Wescott, and D. D. Sentman (1998), Time resolved N_2 triplet state vibrational populations and emissions associated with red sprites, *Journal of Atmospheric and Solar-Terrestrial Physics*, *60*, 811–829.

Morrow, R., and J. J. Lowke (1997), Streamer propagation in air, *Journal of Physics D: Applied Physics*, *30*, 614.

Moss, G. D., V. P. Pasko, N. Liu, and G. Veronis (2006), Monte Carlo model for analysis of thermal runaway electrons in streamer tips in transient luminous events and streamer zones of lightning leaders, *Journal Geophysical Research*, *111*, A02307.

Naidis, G. V. (2009), Positive and negative streamers in air: Velocity-diameter relation, *Phys. Rev. E*, *79*, 057,401, doi:10.1103/PhysRevE.79.057401.

Neubert, T., N. Østgaard, V. Reglero, E. Blanc, O. Chanrion, C. A. Oxborrow, A. Orr, M. Tacconi, O. Hartnack, and D. D. V. Bhanderi (2019), The ASIM mission on the International Space Station, *Space Science Reviews*, *215*, 26.

Oliver, J. E. (1987), *STANDARD ATMOSPHEREStandard atmosphere*, pp. 801–803, Springer US, Boston, MA.

Parra–Rojas, F. C., A. Luque, and F. J. Gordillo–Vázquez (2013), Chemical and electrical impact of lightning on the earth mesosphere: The case of sprite halos, *Journal of Geophysical Research: Space Physics*, *118*(8), 5190–5214.

Parrot, M., U. S. Inan, and N. G. Lehtinen (2008), V-shaped vlf streaks recorded on demeter above powerful thunderstorms, *Journal of Geophysical Research: Space Physics*, *113*, A10,310.

Pasko, V. P. (2006a), *Theoretical modeling of sprites and jets, in Sprites, Elves and Intense Lightning Discharges*, Ser. 2, 253-311 pp., NATO Sci. Ser., Springer, Heidleberg, Germany, edited by Füllekrug, M., E. A. Mareev, and M. J. Rycroft.

Pasko, V. P. (2006b), *Theoretical modeling of sprites and jets, in Sprites, Elves and Intense Lightning Discharges*, Ser. 2, 253-311 pp., NATO Sci. Ser., Springer, Heidleberg, Germany.

Pasko, V. P. (2007), Red sprite discharges in the atmosphere at high altitude: the molecular physics and the similarity with laboratory discharges, *Plasma Sources Science and Technology*, *16*(1), S13–S29.

Pasko, V. P., and H. C. Stenbaek-Nielsen (2002), Diffuse and streamer regions of sprites, *Geophysical Research Letters*, *29*(10).

Pasko, V. P., U. S. Inan, T. F. Bell, and Y. N. Taranenko (1997), Sprites produced by quasi-electrostatic heating and ionization in the lower ionosphere, *Journal of Geophysical Research: Space Physics*, *102*, 4529–4561.

Pasko, V. P., U. S. Inan, and T. F. Bell (1998), Spatial structure of sprites, *Geophysical Research Letters*, *25*, 2123–2126.

Pasko, V. P., J. Qin, and S. Celestin (2013), Toward Better Understanding of Sprite Streamers: Initiation, Morphology, and Polarity Asymmetry, *Surveys in Geophysics*, *34*, 797–830.

Press, W. H., S. A. Teukolsky, W. T. Vetterling, and B. P. Flannery (2007), *Numerical*

Recipes 3rd Edition: The Art of Scientific Computing, 3 ed., Cambridge University Press, New York, NY, USA.

Pérez-Invernón, F. J., A. Luque, F. J. Gordillo-Vázquez, M. Sato, T. Ushio, T. Adachi, and A. B. Chen (2018), Spectroscopic diagnostic of halos and elves detected from space-based photometers, *Journal of Geophysical Research: Atmospheres*, *123*(22), 12,917–12,941.

Pérez-Invernón, F. J., A. Malagón-Romero, F. J. Gordillo-Vázquez, and A. Luque (2020), The contribution of sprite streamers to the chemical composition of the mesosphere-lower thermosphere, *Geophysical Research Letters*, *47*(14), e2020GL088,578.

Qin, J., and V. P. Pasko (2014), On the propagation of streamers in electrical discharges, *Journal of Physics D: Applied Physics*, *47*(43), 435,202.

Qin, J., and V. P. Pasko (2015), Dynamics of sprite streamers in varying air density, *Geophysical Research Letters*, *42*(6), 2031–2036.

Qin, J., S. Celestin, and V. P. Pasko (2011), On the inception of streamers from sprite halo events produced by lightning discharges with positive and negative polarity, *Journal of Geophysical Research: Space Physics*, *116*(A06305).

Qin, J., S. Celestin, and V. P. Pasko (2012), Low frequency electromagnetic radiation from sprite streamers, *Geophysical Research Letters*, *39*(22), L22,803.

Qin, J., S. Celestin, V. P. Pasko, S. A. Cummer, M. G. McHarg, and H. C. Stenbaek-Nielsen (2013a), Mechanism of column and carrot sprites derived from optical and radio observations, *Geophysical Research Letters*, *40*(17), 4777–4782.

Qin, J., S. Celestin, and V. P. Pasko (2013b), Dependence of positive and negative sprite morphology on lightning characteristics and upper atmospheric ambient conditions, *Journal of Geophysical Research: Space Physics*, *118*, 2623–2638.

Qin, J., V. P. Pasko, M. G. McHarg, and H. C. Stenbaek-Nielsen (2014), Plasma irregularities in the D-region ionosphere in association with sprite streamer initiation, *Nature Communications*, *5*, 3740.

Sato, M., T. Ushio, T. Morimoto, M. Kikuchi, H. Kikuchi, T. Adachi, M. Suzuki, A. Yamazaki, Y. Takahashi, U. Inan, I. Linscott, R. Ishida, Y. Sakamoto, K. Yoshida, Y. Hobara, T. Sano, T. Abe, M. Nakamura, H. Oda, and Z.-I. Kawasaki (2015), Overview and early results of the Global Lightning and Sprite Measurements mission, *Journal of Geophysical Research: Atmospheres*, *120*, 3822–3851.

Ségur, P., A. Bourdon, E. Marode, D. Bessieres, and J. H. Paillol (2006), The use of an improved eddington approximation to facilitate the calculation of photoionization in streamer discharges, *Plasma Sources Science and Technology*, *15*(4), 648–660.

Sentman, D. D., E. M. Wescott, D. L. Osborne, D. L. Hampton, and M. J. Heavner (1995), Preliminary results from the sprites94 aircraft campaign: 1. red sprites, *Geophysical Research Letters*, *22*, 1205–1208.

Sentman, D. D., H. C. Stenbaek-Nielsen, M. G. McHarg, and J. S. Morrill (2008), Plasma chemistry of sprite streamers, *Journal of Geophysical Research: Atmospheres*, *113*(D111112).

Shi, F., N. Liu, and J. R. Dwyer (2017), Three-dimensional modeling of two interacting streamers, *Journal of Geophysical Research: Atmospheres*, *122*(19), 10,169–10,176.

Shi, F., N. Liu, J. R. Dwyer, and K. M. A. Ihaddadene (2019), Vhf and uhf electromagnetic radiation produced by streamers in lightning, *Geophysical Research Letters*, *46*(1), 443–451.

Siefring, C. L., J. S. Morrill, D. D. Sentman, and M. J. Heavner (2010), Simultaneous near-infrared and visible observations of sprites and acoustic-gravity waves during the exl98 campaign, *Journal of Geophysical Research: Space Physics*, *115*(A10).

Siefring, C. L., J. S. Morrill, D. D. Sentman, and M. J. Heavner (2010), Simultaneous near-infrared and visible observations of sprites and acoustic-gravity waves during the EXL98 campaign, *Journal Geophysical Research*, *115*, A00E57.

Suszcynsky, D., R. Roussel-Dupre, W. Lyons, and R. A. Armstrong (1998), Blue-light imagery and photometry of sprites, *Journal of Atmospheric and Solar-Terrestrial Physics*, *60*, 801–809.

Uman, M., K. Mclain, and E. Krider (1975), The electromagnetic radiation from a finite antenna, *American Journal of Physics*, *43*, 33–38.

Ushio, T., M. Sato, T. Morimoto, M. Suzuki, H. Kikuchi, A. Yamazaki, Y. Takahashi, Y. Hobara, U. Inan, I. Linscott, Y. Sakamoto, R. Ishida, M. Kikuchi, K. Yoshida, and Z.-I. Kawasaki (2011), The Global Lightning and Sprite Measurement (GLIMS) Mission on International Space Station, *IEEJ Transactions on Fundamentals and Materials*, *131*(12), 971–976.

van der Velde, O. A., W. A. Lyons, T. E. Nelson, S. A. Cummer, J. Li, and J. Bunnell (2007), Analysis of the first gigantic jet recorded over continental north america, *Journal of Geophysical Research: Atmospheres*, *112*(D20).

Vetter, S. (2019), https://apod.nasa.gov/apod/ap191008.html, consultation on 2nd Sep. 2020, 14h37.

Vitello, P. A., B. M. Penetrante, and J. N. Bardsley (1994), Simulation of negative-streamer dynamics in nitrogen, *Physical Review E*, *49*, 5574–5598.

Wait, J. R., and K. P. Spies (1964), Characteristics of the earth-ionosphere waveguide for vlf radio waves, p. Tech note 300, National Bureau of Standards: Boulder, Colorado.

Wescott, E. M., D. Sentman, D. Osborne, D. Hampton, and M. Heavner (1995), Prelim-

inary results from the sprites94 aircraft campaign: 2. blue jets, *Geophysical Research Letters*, *22*(10), 1209–1212.

Xu, C., N. Huret, M. Garnung, and S. Celestin (2020), A new detailed plasma-chemistry model for the potential impact of blue jet streamers on atmospheric chemistry, *Journal of Geophysical Research: Atmospheres*, *125*(6), e2019JD031,789.

Zalesak, S. T. (1979), Fully multidimensional flux-corrected transport algorithms for fluids, *Journal of Computational Physics*, *31*(3), 335 – 362.

Zalesak, S. T. (2012), *The Design of Flux-Corrected Transport (FCT) Algorithms for Structured Grids*, pp. 23–65, Springer Netherlands, Dordrecht.

Zarka, P., J. N. Girard, M. Tagger, L. Denis, and the LSS team (2012), LSS/NENUFAR: The LOFAR super station project in Nançay, in *SF2A-2012: Semaine de l'Astrophysique Francaise*, pp. 687–694.

Zarka, P., M. Tagger, L. Denis, J. N. Girard, A. Konovalenko, M. Atemkeng, M. Arnaud, S. Azarian, M. Barsuglia, A. Bonafede, F. Boone, A. Bosma, R. Boyer, M. Branchesi, C. Briand, B. Cecconi, S. Célestin, D. Charrier, E. Chassande-Mottin, A. Coffre, I. Cognard, F. Combes, S. Corbel, C. Courte, A. Dabbech, S. Daiboo, R. Dallier, C. Dumez-Viou, M. N. E. Korso, E. Falgarone, I. Falkovich, A. Ferrari, C. Ferrari, K. Ferrière, C. Fevotte, A. Fialkov, M. Fullekrug, E. Gérard, J.-M. Grießmeier, B. Guiderdoni, L. Guillemot, J. Hessels, L. Koopmans, V. Kondratiev, L. Lamy, T. Lanz, P. Larzabal, M. Lehnert, F. Levrier, A. Loh, G. Macario, J.-J. Maintoux, L. Martin, D. Mary, S. Masson, M.-A. Miville-Deschenes, D. Oberoi, M. Panchenko, M. Pandey-Pommier, A. Petiteau, J.-L. Pinçon, B. Revenu, F. Rible, C. Richard, H. O. Rucker, P. Salomé, B. Semelin, M. Serylak, O. Smirnov, B. Stappers, C. Taffoureau, C. Tasse, G. Theureau, P. Tokarsky, S. Torchinsky, O. Ulyanov, W. van Driel, I. Vasylieva, J. Vaubaillon, F. Vazza, S. Vergani, M. Was, R. Weber, and V. Zakharenko

(2015), Nenufar: Instrument description and science case, in *International Conference on Antenna Theory and Technique*, pp. 13–18.

Zheleznyak, M. B., A. K. Mnatsakanyan, and S. V. Sizykh (1982), Photoionization of nitrogen and oxygen mixtures by radiation from a gaz discharge, *High Temperature*, *20*, 357–362.

Matthieu GARNUNG

Modélisation numérique haute-performance de streamers de sprites : Développement de diagnostics optiques et électromagnétiques pour caractériser les événements lumineux transitoires en vue de la mission TARANIS.

Résumé : Les événements lumineux transitoires (TLE) sont des d'événements brefs et lumineux se produisant au-dessus des orages. Dans le cadre de cette thèse, nous nous intéressons particulièrement aux sprites. Ils sont composés de filaments de plasma appelés streamers qui se propagent par l'ionisation locale du milieu. Les sprites se produisent suite à l'établissement d'une connexion électrique entre le nuage d'orage et le sol générant un déséquilibre soudain des charges électriques entre le nuage et l'ionosphère. Le champ électrostatique ainsi induit augmente l'énergie des électrons présents dans les couches supérieures de l'atmosphère terrestre déclenchant l'apparition de streamers, lesquels génèrent des processus d'ionisation et d'émission radiative souvent perçus comme rougeâtres entre 40 et 90 km d'altitude.Plusieurs missions spatiales ont adopté des stratégies d'observation au nadir. Cependant, cette géométrie entraîne une perte de la résolution verticale.Afin de surmonter cet inconvénient, nous proposons dans cette thèse, une méthode pour déterminer l'altitude et le champ électrique associés aux sprites à partir de leurs émissions optiques.Pour cela, nous avons développé un code plasma fluide modélisant les décharges de streamers. Le code résoud l'équation de Poisson pour obtenir le champ électrostatique, l'équation de dérive-diffusion pour le mouvement des espèces chargées, la méthode SP3 à trois groupes pour les processus de photoionisation ainsi que l'ionisation et l'attachement des électrons. Afin de prédire les émissions optiques que les sprites produisent, nous modélisons la production d'états électroniques excités du diazote et de son ion positif.Nous utilisons également le modèle d'antenne d'Uman pour estimer les émissions radio des streamers de sprites.Avec ce modèle, nous étudions l'applicabilité d'une méthode permettant de déterminer l'altitude et le champ électrique d'un streamer à partir d'observations spectrophotométriques.Une comparaison entre des simulations et des données satellitaires montrent que cette méthode peut être utilisée pour analyser les observations réalisées au nadir depuis l'espace. Les limitations de cette approche ont été étudiées au travers de la simulation de la propagation de streamers sur plusieurs hauteurs d'échelles et de l'influence du taux caractéristique d'expansion exponentielle en fonction de la taille de l'inhomogénéité initiale.De plus, nous avons étudié les signatures radio dans la bande HF-VHF lors de la collision frontale entre deux streamers de polarités opposées. En négligant le filtrage ionosphérique, nous avons montré que l'instrument TARANIS IME-HF aurait pu observer de telles émissions. De plus, nous montrons que le radiotélescope NenuFAR est également capable de faire de telles observations depuis le sol.

Mots clés : Sprite, simulation numérique, Emission optique

High-performance numerical modeling of sprite streamers: Development of optical and electromagnetic diagnostics to characterize transient luminous events for the TARANIS mission.

Summary : Transient luminous events (TLEs) are brief and bright events occurring above thunderstorms. In the framework of this thesis, we are particularly interested in sprites. They are composed of plasma filaments called streamers that propagate through local ionization. Sprites occur following the establishment of an electrical connection between a thundercloud and the ground generating a sudden imbalance of electric charges between the cloud and the ionosphere. The induced electric field energizes the electrons present in the upper layers of the Earth's atmosphere and initiate streamers, generating ionization and radiative emission processes often perceived as reddish between 40 and 90 km in altitude.Several space missions have adopted nadir-viewing observation strategies. However, this geometry leads to a loss of the vertical resolution.In order to overcome this drawback, we propose to use a spectrophotometric technique to determine the altitude and the electric field associated with the sprites from their optical emissions.To this end, we have developed a plasma fluid code modeling streamer discharges. The code consists in solving Poisson's equation to obtain the electrostatic field, the drift-diffusion equation for the motion of charged species, the three-group SP3 method for photoionization processes as well as ionization and electron attachment. To predict the light emissions that sprites produce, we keep track of the production of excited electronic states of nitrogen molecules and ions.We also use Uman's antenna model to estimate radio emissions from sprite streamers.With this model, we investigate the applicability of a method to determine the altitude and electric field of a streamer from spectrophotometric observations.A comparison between simulations and satellite observations show that this method can be used to exploit space-based observations in nadir-viewing geometry.Limitations of the spectrophotometric method are investigated through the study of streamer propagation over several scale heights and the dependence of the exponential expansion characteristic rate on the size of the initial inhomogeneity.Additionally, we investigated radio signatures in the HF-VHF band during the head-on collision between two streamers of opposite polarities. Neglecting ionospheric filtering we have shown that the TARANIS IME-HF instrument would have been able to observe such emissions. Moreover, we show that the NenuFAR radiotelescope is also capable of making such observations from the ground.

Keywords : Sprite, numerical simulation, Optical emission

Laboratoire de Physique et Chimie de l'Environnement et de l'Espace (LPC2E)
3A avenue de la recherche scientifique
45071 Orléans CEDEX 2